Lyα Emitters as a Probe of Galaxy Formation and Ionisation History

Loren Richard Bruns Jr

Submitted in Total Fulfillment

of the Requirements of the Degree of

Doctor of Philosophy

School of Physics

The University of Melbourne

April 2016

Abstract

Current observations suggest that the reionisation of hydrogen in the intergalactic medium had begun by $z \sim 10$ and was completed around $z \sim 6$. Directly observing this epoch is not possible with existing instrumentation, making it difficult to infer how the increased ionising background during this period affected galaxy formation. This thesis aims to put constraints on the galaxy formation history of the Universe with existing instruments, by modelling and observing the number densities of observed Lyα emitters in the ionised environments around $z \sim 2-3$ quasars to mimic conditions found during the epoch of reionisation.

The main work presented is a model for the ionisation state of the intergalactic medium around star forming galaxies in the vicinity of a luminous quasar, tuned by empirical relationships from conditions at $z \sim 2-3$. This model suggests that the intense ionising radiation from a quasar offsets the increased density of the intergalactic medium found around it, implying that the direct detection of star forming galaxies by their Lyα emission in the vicinity of $z \sim 2-3$ quasars is less obstructed by the intergalactic medium than galaxies in the field.

The accuracy of this model is compared to existing Lyα galaxy surveys and found to be in good agreement. Discrepancies exist between the expected number of Lyα emitting galaxies this model predicts and the surveyed region around the super-luminous quasar PKS 0424-131, in which no Lyα emission was detected. The

modelling done suggests that in order to be consistent with this null detection at the 68 % (90 %) level, galaxies below $2.5 \times 10^{12}\,M_{\odot}$ ($4.2 \times 10^{12}\,M_{\odot}$) must be omitted. These results suggest that considerable radiative suppression of galaxy formation by PKS 0424-131 is taking place.

This hypothesis is tested using observations made on the Baade telescope at the Las Campanas Observatory with the Maryland Magellan Tunable Filter. The unique suitability of tunable filters for the detection of high-redshift galactic Lyα emission is described in detail, along with their idiosyncratic calibration and data reduction processes. The adverse seeing conditions make it impossible to put limits on the impact of ionising radiation of galaxy formation using these observations, and an analysis of the factors that prevented detection is provided. Finally, suggestions are made for ways to improve the chance of success for future observations of this effect using tunable filters, as well as ways to remove spurious ghost reflections in the data analysis that are unique to tunable filter observations.

Declaration

This is to certify that:

(i) This thesis, entitled 'Lyα Emitters as a Probe of Galaxy Formation and Ionisation History', comprises only my original work towards the PhD, except where indicated otherwise;

(ii) Due acknowledgement has been made in the text to all other material used;

(iii) This thesis has fewer than 100 000 words, exclusive of tables, bibliographies and appendices.

.....

Loren Richard Bruns Jr

Preface

This preface contains a summary for each chapter in this thesis and a listing of the chapters which are included in publications, detailing the contributions from co-authors and supervisors.

- Chapter 1 is an original overview of the background, key concepts, and motivation for this thesis, with previous works cited.

- Chapter 2 presents original work done to model the Lyα transmission of star forming galaxies through the intergalactic medium at high-redshift.

- Chapter 3 describes original work using the models presented in chapter 2 to determine the expected number density of Lyα galaxies in survey volumes.

- Chapter 4 is an original overview of tunable filter technology, specifically describing their unique suitability in the detection of high-redshift galaxies by their Lyα emission. It further outlines an original experiment conducted to look for evidence of the radiative suppression of galaxies in the vicinity of high-redshift quasars and the modelling done to determine the expected number of detectable Lyα galaxies in the observations conducted.

- Chapter 5 is an original overview of the data reduction process for tunable filter observations, and presents a novel pipeline for selecting candidate Lyα

galaxies from the final science images. It goes on to show that the observations described in chapter 4 resulted in a null detection of Lyα galaxies, consistent with the low sensitivities achieved.

- Chapter 6 is an original summary of the work presented in this thesis, along with concluding remarks.

Chapters 2 and 3 constitute work that has been previously published as a single paper (Bruns et al., 2012). The author of this thesis was the first author on this paper, and was the main contributor to the work presented therein. The co-authors on this paper were J. S. B. Wyithe, J. Bland-Hawthorn and M. Dijkstra. Each contributed to its inspiration, the concepts and ideas it presents, and its preparation for publication. All the software created in the course of this work was written and used solely by the author.

Acknowledgements

It is unfortunate that the acknowledgements section is traditionally written at the end of the thesis writing process. A more fair and accurate distribution of praise would result by taking a detailed journal throughout the long years of toil and using that as the basis of acknowledgements, rather than the misremembered anecdotes of a stress-addled brain at the conclusion. That said, what follows are the best misremembered anecdotes I could come up with at the last minute. Hopefully they will do justice to all those that helped and supported me during the completion of this thesis.

First I'd like to thank my parents for all their support in every aspect of my life. Having recently become a parent I appreciate their unwavering commitment to my well-being all the more, and I am so happy that coming out the other end of my childhood we're such good friends. In particular, their continued blessing of my great migration to Australia and insistence that I follow through with this thesis has been invaluable.

This entire adventure would have gone differently had not Professor Mary James asked if I was interested in learning about gravitational lensing for my undergraduate thesis project. Through the retrospectoscope it is easy to point to that conversation as the springboard for my interest in astrophysics and subsequent decision to begin my PhD in Australia. Her kindness and personality made her an ideal mentor, and

it was a pleasure and an honour to work with her at Stanford for a year after completing my physics bachelors degree to continue our work on gravitational lensing.

My mother was always insistent that I travel the world. As a graduation present she found an Australian touring company that seemed to offer the best travel experience for those between the ages of eighteen and thirty-five, and organised a forty-five day camping tour around Europe. This gift, and the year-long delay my work at Stanford required not only opened my eyes to the world, but drew my gaze directly to Australia through the person of my wife and best friend Caitlin. My decision to pursue my postgraduate studies in Melbourne were a directly consequence of our then long-distance relationship.

Caitlin deserves the lion's share of all the publicity and renown that comes from this intellectual endeavour. She has been behind me all the way, often shoving firmly, and this last year she has managed to take care of both our seven-month-old Natalie and my work-life imbalance with aplomb. She's been the keystone keeping everything together, and has successfully reminded me on two separate occasions during this seven year odyssey to normalise the power-spectrum.

Professor Rachel Webster is directly responsible for the beginning and subsequent completion of this thesis. In particular, during a fortuitous cleaning of her email's junk box she ran across an email entitled 'International Astrophysics PhD Inquiry'. Her encouraging reply to that initial inquiry and the following email correspondence had me in Australia on a student-visa within six months. She was also instrumental in lighting the fire under me that saw this manuscript go from some notes and a published paper to a doctoral thesis, also in six months. These two six month periods form the bookends to an eventful time in my life, and I'm not sufficiently poetic to express my gratitude for Rachel's help in making it happen.

I'd like to thank my supervisor Professor Stuart Wyithe for agreeing to work

with me sight unseen upon my arrival in Australia. He helped me to quickly get up to speed on the current state of cosmology and guided me through the publication of my paper 'Clustering of Lyα emitters around luminous quasars at $z = 2 - 3$: an alternative probe of reionisation on galaxy formation'. He also introduced me to the two collaborators on this paper, Professor Joss Bland-Hawthorn, and Associate Professor Mark Dijkstra. Their work on the theory and observation of Lyα emission form the bedrock upon which this thesis is built upon.

My cohort of post-graduate students in the University of Melbourne School of Physics all deserve a large, boundaries respecting physical and mental hug after all this. Chris[1], Brad, Steve, Dre, Mark, Letizia, and Cat were not only my first academic colleagues and charter members of my thesis support group, they became my first batch of friends here in Australia. Thank you all so much for such a wonderful welcome.

To Cat, Steve, T'Mir, and Andreas, thank you for reading my thesis all those times so that I didn't have to. It's so much the better for your constant vigilance, I can't thank you enough for putting in the time and effort to see this thing dead and buried, in a good way.

Finally, I'd like to thank the University of Melbourne and the ARC Centre of Excellence for All-sky Astrophysics for supporting me financially as I transitioned into my new life on a new continent. The generosity that these institutions and the Australian government have shown this migrant from across the sea is truly humbling, and I am enthusiastic to pay that generosity forward in the coming decades to those in my adoptive country.

[1]I've had more coffee with Chris than anyone else in my life, and I think we're both much better off for it.

Contents

List of Figures

List of Tables

Chapter 1

Introduction

The structure of the Universe has been shaped by periods of intense star formation. The first stars are thought to have appeared between 65 and 180 million years after the first matter in the Universe was formed, followed 410 to 750 million years later by a more pervasive population of stars that make up the galaxies and large-scale structure seen today. This second population of stars is presumed to have produced the majority of the ultraviolet photons that reionised the then-prevalent neutral hydrogen in the Universe. At the present time it is not at all clear what impact this dramatic rise in the background intensity of ionising photons had on galaxy formation and evolution. Directly observing galaxy formation during reionisation is not possible with current telescopes, and creating this capability is one of the major science drivers for the upcoming James Webb Space Telescope. This thesis presents a novel approach to probe the effect of reionisation on galaxy formation and evolution indirectly, using surrogate environments that are within the resolving power of existing ground-based telescopes.

This thesis describes the modelling and observation of galaxy clusters from 2 to 3 billion years ago. These clusters usually contain a large central galaxy hosting an active nucleus emitting an intense stream of ultraviolet radiation, mimicking the conditions found much earlier in the formation history of the Universe. The models developed use semi-analytical methods to determine the average number of galaxies that should inhabit these regions, and the fraction of these galaxies that

should be detectable using current instrumentation. The models do not account for any suppression in star formation from the strong ultraviolet emission from the central galaxy, so any discrepancy between the modelled and observed regions will give insight on the strength of this effect.

This chapter introduces the relevant background required to understand the details of the cosmological models and narrowband observations conducted in the course of this experiment and to place the violent period of cosmic history known as the epoch of reionisation in context.

1.1 A brief history of the Universe

The canonical view of the Universe is one of constant evolution. Current theory begins with the Universe in a hot and condensed state, with all the energy observed at the present day distributed isotropically and homogeneously into an infinitesimally smaller physical volume. The average energy density of the Universe was so high that the fundamental forces and phases of matter experienced today were incapable of existing. These are the conditions as they were at a single snapshot in history, now referred to as the Big Bang. Even at this point in its history, the one defined out of necessity to be the beginning, the Universe was already evolving.

The extreme energy density of the Universe at this time was causing space-time itself to expand, creating more physical distance between all points in the Universe. In just the first second after the Big Bang the Universe had already experienced a series of dramatic transformations: a period of exponential expansion known as cosmic inflation had lowered the average energy density enough to form matter–antimatter pairs of the familiar sub-atomic building blocks – protons, neutrons, and electrons – as well as the less familiar dark matter that dominates the present-day matter budget; a period where continued expansion saw the overall temperature fall

to the point where pairs of these particles were no longer created spontaneously, leading to a mass annihilation of matter and antimatter that saw just 1 part in 10^{10} of the matter remain and all the free antimatter destroyed; and all of this turmoil ending in a period where the remaining matter cooled to the point where the energy density of the Universe was then dominated by photons. These photons were to remain tightly coupled to the resulting plasmatic soup of protons, neutrons, and electrons for the next 372 000 years, until the inexorable expansion of the Universe would cause the next major transition.

During this relative period of calm the Universe continued to expand, until the lowering energy density finally made it energetically favourable for electrons in the all-pervasive plasma to combine with protons to form neutral hydrogen. This sudden drop in the number of free electrons caused the mean time between interactions for the photons trapped in the plasma to increase to greater than the crossing time of the Universe, decoupling the photons from the newly formed hydrogen atoms. These photons lit up the Universe for the first time, and are detected today as the cosmic microwave background (CMB). In the 13.8 billion years since their journey began, the CMB photons have travelled through an ever expanding space-time metric, causing their wavelength to stretch – and therefore redden – in a process known as cosmological redshift.

1.2 Cosmological redshift and distance

There is a limited amount of information that can be extracted from a photon about its origins. Individually, the most useful information extracted is its wavelength at the time of detection. From an ensemble of photons, it is further possible to determine the emission and absorption spectrum of an object and its luminosity at each wavelength. However, to determine the cosmological distance a photon has

travelled requires not only an understanding of the exact conditions of its emission but also a model for the expansion history of the Universe. This knowledge of the provenance of a photon is packed within a single quantity called its redshift.

The redshift of a photon is defined as the increase in the ratio of the observed wavelength of a photon compared to when it was originally emitted. This is equivalent to comparing the relative scale of the physical distance between two points at present day to that at a certain lookback time. Mathematically, the redshift z of a photon is defined as

$$1 + z = \frac{\lambda_{\text{observed}}}{\lambda_{\text{emitted}}} = \frac{a(t_0)}{a(t)}, \tag{1.1}$$

where $a(t)$ is the time-dependent scale factor of the Universe and is defined by the assumed cosmology.

This relationship gives us the ability to determine the age of a cosmologically distant object from the observed wavelength of its emitted photons, provided the process that caused their emission is fully understood. In the case of the CMB photons, they are theorised to be emitted in a nearly perfect black-body spectrum, peaking at around 3000 K. The measured profile of the CMB at the present day peaks at 2.726 K, translating to a redshift of 1090. This corresponds to the previously mentioned 372 000 years after the Big Bang.

1.3 The epoch of reionisation

After the CMB radiation had fully decoupled from the atomic matter, the Universe entered into period known within astronomy as the Dark Ages. At this point there were no stars or galaxies, just a sea of neutral hydrogen and dark matter spread evenly throughout space. Quantum fluctuations in this isotropic universe caused certain regions of space to become denser than average, and through gravitational attraction these regions attracted neighbouring matter. After 100 to 180 million

years, at a redshift $z = 20 - 30$, the Universe had begun the process of large structure formation, continually segregating into bound objects containing the first stars and into growing voids of empty space.

The form these initial stars took, their duration and life cycle, and the impact their likely violent deaths had on their surroundings is still a topic of debate.[1] Even though these stars were emitting the first significant population of post-CMB photons the bulk of these photons were absorbed and scattered out of line-of-sight by pervasive neutral hydrogen, preventing a detailed study using current observational methods. This veil would not be lifted until the second generation of stars and active galactic nuclei (AGN) saturated the Universe with enough radiation to ionise the neutral hydrogen back into a plasma, a period called the epoch of reionisation (EoR).

Current models of reionisation are constrained by observations to have begun by $z \sim 8.8$ at the latest, as measured by anisotropies in the polarisation of CMB photons at large angular scale (Planck Collaboration et al., 2015). This polarisation was caused by newly liberated electrons interacting with the free streaming CMB photons, through a process known as Thomson scattering. The relevant calculation assumes an instantaneous reionisation of the hydrogen not bound in galaxies, and thus for a realistic extended period of universal reionisation it represents the latest time the reionisation process could have begun.

The popular picture of this process assumes that the first major sources of ionising radiation were isolated from one another, each carving out small, localised, bubbles of ionised hydrogen known as H II regions. Over time, as the cosmic star formation rate increased and ionisation from AGN grew in strength, the H II regions grew in size and eventually began overlapping with neighbouring regions. As

[1] See Bromm et al. (2009) for a concise overview of the formation of the first stars.

the regions overlapped, their collective surface area decreased in relation to the number of ionising photons being created within them, increasing the ionisation rate of the remaining neutral hydrogen in the IGM. Once all the H II regions merged the Universe was once again pervaded by a plasma of electrons and protons.

It was during this period that the large-scale structure of the Universe began to form in earnest, when complex interactions between matter and radiation shaped the Universe observable today. Understanding these interactions in detail is therefore required for any successful model of galaxy formation and evolution. Unfortunately for present day astronomers, the bulk of these early interactions are hidden from view within the individual H II regions formed at the beginning of reionisation. Future observations with the James Webb Space Telescope are expected to probe these regions directly and shed light on the first galaxies (Bromm & Yoshida, 2011). In the interim, novel techniques using current instrumentation are required to shed light on the outstanding questions of galaxy formation taking place before and during the EoR.

1.4 Lyα radiation

The cosmic reionisation of hydrogen is assumed to have completed by $z \sim 6$, an estimate based on the absorption of Lyman-α photons by the matter in the Universe not bound within galaxies – the IGM. To appreciate the details of this important detection requires an understanding of the history and significance of the Lyman-α transition in hydrogen.[2]

The emission of a Lyman-α (Lyα) photon is caused by the relaxation of a hydrogen electron from the $n = 2$ orbital to the ground state, corresponding to a wavelength of 1215.67 Å, and is so-named because it is the first transition in the Ly-

[2]See Nilsson (2007) for a more in-depth discussion on the history of Lyα and its general use as a cosmological tool.

man spectral series. The first discussions of Lyα in astronomy came in the 1920s (Menzel, 1926; Zanstra, 1927), in the context of the diffuse emission of Lyman series photons from stellar nebulae within the galaxy. The original hypothesis, later proven to be correct, was that ionising radiation from hot *O* and *B* stars embedded in a stellar nebula ionise the neutral hydrogen gas from within. During the recombination of the ionised nebular hydrogen the electrons cascade down the orbitals in a series of excitations and relaxations, preferentially settling in the $n = 2$ orbital. A final relaxation emits a Lyα photon, which escapes the nebula and streams freely. It has been shown mathematically and observationally that fully two of every three ionising photons absorbed by the nebula leave as Lyα photons (see case-B recombination in Osterbrock, 1989).

In the 1960s the emission and absorption of Lyα was explored again, this time on cosmological scales. Partridge & Peebles (1967) performed the first calculation of the expected Lyα emission from a young, star forming galaxy, and determined correctly that fully 10 % of the bolometric luminosity would come from Lyα photons. This suggested at the time that observing Lyα emission would be a good indication of star formation in galaxies, however this detection would elude observers until the 1990s. Two years earlier, Gunn & Peterson (1965) studied the continuum of a $z \sim 2$ AGN, and noted a slight absorption of the photons blueward of its Lyα emission. They realised that as the photons blueward of Lyα underwent redshift they would eventually have the same wavelength as a Lyα photon. This is just the right amount of energy to ionise neutral hydrogen in the IGM, and therefore it will have an increased chance of being absorbed by this hydrogen and re-emitted in a random direction. From this idea they calculated that the IGM must be highly ionised as far back as $z \sim 2$, to better than 1 part in 5×10^6 given the assumed density of hydrogen, and that even an ionisation ratio as high as 1 part in 10^5 would still cause the IGM

to absorb and scatter 50 per cent of photons blueward of Lyα. Observations of this spectral absorption feature, referred to as the Gunn-Peterson trough, has become a standard tool to probe the Universe at high redshift. To use this technique requires a luminous background object with a well understood spectrum, and is most often conducted with quasars.

1.5 Quasars

A quasar is the brightest and most distant class of AGN, with their extreme luminosities – one hundred times that of the Milky Way galaxy – caused by the accretion and infall of matter onto the supermassive ($\geq 10^6\,M_\odot$) black hole housed at their centre. They were first observed by their radio emission (Greenstein & Schmidt, 1964), which like stars is point-like and not spatially resolved. Owing to this similarity they were originally designated as 'quasi-stellar radio sources', which was later informally shortened to 'quasars'. Because of their extreme distance – the most distant confirmed quasar being found at a redshift of ~7 (Mortlock et al., 2011) – quasar spectra are perfect background sources for measuring Lyα absorption caused by Gunn-Peterson absorption in the IGM. Quasar spectra were used by Fan et al. (2006) to show that the Universe was rapidly ionising by around z~6, indicating an effective end of the EoR.[3]

It is speculated that the dark matter haloes housing quasars and their host galaxies are among the first that formed in the Universe, as it is difficult to otherwise explain their ability to contain such a massive central black hole so soon after the Big Bang. Because of the large amount of time they have had to grow through mergers and the substantial accretion of nearby dark matter, these haloes are some of the largest in

[3]Direct imaging of galaxies by their Lyα emission at $z \gtrsim 7$, including one at $z \sim 8.7$ (Zitrin et al., 2015), promotes the theory that large pockets of the Universe were fully ionised much earlier. This suggests an extended and patchy reionisation history.

the Universe and are usually found at the centres of large galaxy clusters. This makes quasars easily detected tracers of large scale structure at high-redshift, a fact that is exploited in this thesis.

1.6 Dark matter haloes and their properties

The currently accepted cosmological model is built upon the assumption that the Universe is dominated by a form of matter that only interacts appreciably with other matter – even other dark matter – through gravitational attraction. This cold dark matter dominates the visible matter in the Universe by a factor of ~5.4 (Planck Collaboration et al., 2015), and through its dominance has shaped the structural history of the Universe.

Because of its negligible interaction with the electromagnetic force, dark matter cannot use the same mechanisms as visible matter to shed angular momentum. This causes dark matter to remain in diffuse distributions after forming bound objects, referred to as dark matter haloes, rather than collapsing to a point. The first galaxies were born within the gravitational well of these dark matter haloes, where hydrogen gas accumulated in sufficient densities to cool and fragment into stars.

Modelling shows that the formation of stars generates pressure waves that reduce the density of the surrounding gas, and that the radiation from the stars themselves can cause a heating of the surrounding gas (Kitayama et al., 2004; Alvarez et al., 2006). These effects can cause the gas required for star formation to escape from the host dark matter halo if its potential well is not sufficiently deep, smothering future star formation. It is therefore useful to define a set of quantities that help describe the potential well of a dark matter halo.

Most distributions used to model dark matter density have extended wings and, as a result, it is difficult to describe a useful physical size for a given halo. Because

dark matter only interacts meaningfully through gravitation, it is assumed that dark matter haloes eventually come to virial equilibrium. This is where the gravitational potential of the halo, U, is related to the final kinetic energy of the constituent dark matter, K, by the expression $U = -2K$. While there are multiple ways to use this relationship to quantify a dark matter halo (White, 2001), it is common in theoretical cosmology to use the virial theorem to define the radius, $r_{\rm vir}$, corresponding to the critical mass required to collapse a halo of mass M by redshift z:

$$r_{\rm vir} = 0.784 \left(\frac{M}{10^8\, h^{-1}{\rm M}_\odot}\right)^{1/3} \left[\frac{\Omega_{\rm m}}{\Omega_{\rm m}{}^z}\frac{\Delta_{\rm c}}{18\,\pi^2}\right]^{-1/3} \left(\frac{1+z}{10}\right)^{1/2} {\rm km\,s^{-1}}, \qquad (1.2)$$

where h is the dimensionless Hubble constant, $\Omega_{\rm m}$ and $\Omega_{\rm m}{}^z$ are the mass density of the Universe at the present-day and at the redshift of collapse respectively, and $\Delta_{\rm c}$ is the critical density at the collapse redshift. These four parameters are defined in terms of empirically measured cosmological values, with their exact form dependent on the assumed cosmology.[4] This virial radius is used in the literature, and within this thesis, to parametrise the radial extent of modelled dark matter haloes.

Related to the virial radius is the virial temperature, $T_{\rm vir}$, which describes the thermal temperature of material that has fallen into the potential well and reached equilibrium. This is expressed as:

$$T_{\rm vir} = \frac{\mu m_{\rm p} G}{2k_{\rm B}}\frac{M}{r_{\rm vir}}, \qquad (1.3)$$

where μ is the mean molecular weight of the Universe at the collapse redshift, $m_{\rm p}$ is the proton mass, and $k_{\rm B}$ is the Boltzmann constant. Thus, the virial temperature is a redshift-dependent parametrisation of the potential well depth of a halo, thereby

[4] See Barkana & Loeb (2001) for a comprehensive review of the mathematical formalism behind the first sources of light, and the origins of the EoR.

providing information on the ability of the halo to retain disturbed gas and how efficient the different available mechanisms for cooling that gas are.

1.7 Searches for Lyα emission

Owing to the high emission of Lyα compared with other spectral features, it is natural to assume that direct imaging of Lyα would be straightforward. However, it was not until the 1990s that the first direct detection of galaxies by their Lyα emission was accomplished, using purpose-built narrow-band filters (Lowenthal et al., 1991; Wolfe et al., 1992; Møller & Warren, 1993; Macchetto et al., 1993).

Direct searches for Lyα emitters (LAEs) – either galaxies or fluoresced hydrogen clouds – have to work around the fact that the feature of interest is a thin spike measuring 5 Å to 10 Å in width. Most filters used for galaxy surveys use a selection of broadband filters, each with a bandpass on the order of 1000 Å. This width makes it easy to contaminate the Lyα peak with other nearby features, such as the infrared photons emitted from OH molecules in the atmosphere, swamping the Lyα signal in a forest of strong peaks.

To get around these issues and identify the Lyα peak, most surveys that are directly targeting Lyα are conducted with a specially prepared glass filter with a narrow 25 Å to 100 Å bandpass corresponding to Lyα photons emitted at a specific redshift. To keep the signal-to-noise ratio as high as possible, it is important that the bandpasses in these filters lie within gaps in the background infrared sky noise. Figure 1.1 shows the infrared sky noise across the optical spectrum, with traditional broadband and narrowband filters overlaid. To fit within these gaps, the width and central wavelength of these narrowband filters in most blind, deep Lyα emitter surveys are limited to particular redshifts (see Ouchi et al., 2008). While this technique allows large Lyα emitter catalogues to be collected, it also forces the hand of the observer

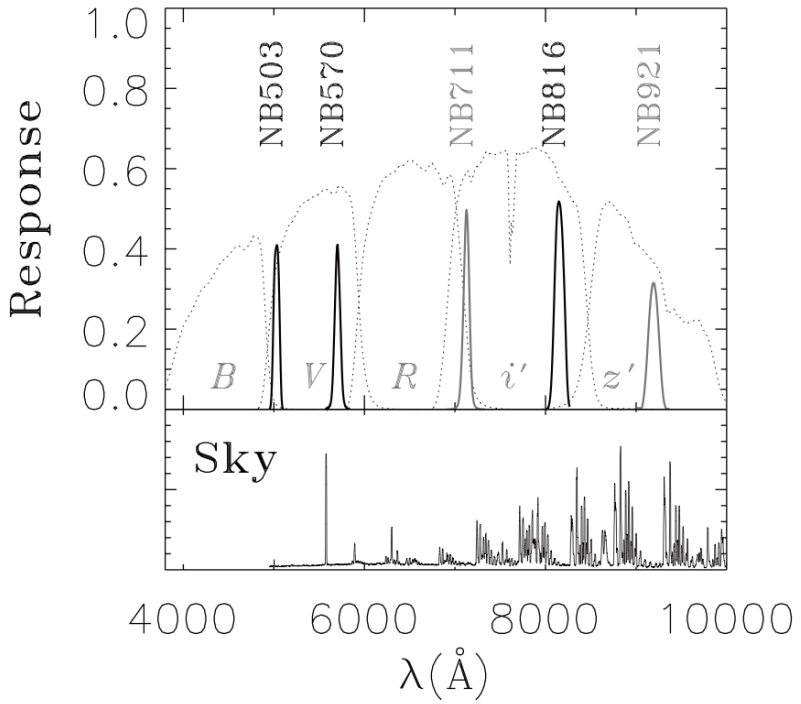

Figure 1.1: Sky infrared background, with narrowband and broadband filter transmission curves overlaid. Image from Ouchi et al. (2008).

in target selection.

1.8 Radiative suppression of star formation

The main motivation for the work in this thesis was an observation of the luminous $z = 2.168$ quasar PKS 0424-131 by Francis & Bland-Hawthorn (2004). Based on surveys done at similar redshifts, they expected to see between 6 and 25 fluorescing hydrogen clouds of varying sizes and $\gtrsim 10$ internally ionised Lyα emitting galaxies. However, their observations found no Lyα emission of any kind, leading them to the tentative conclusion that quasar induced photo-evaporation was destroying the clouds and supressing the formation of stars in nearby galaxies.

The exact ways in which the increased background of ionising radiation present during the EoR effected the evolution of young galaxies is an open question. In par-

ticular, authors have stressed the need to establish the critical ionising flux density for which star formation is suppressed, based in large part on observations of fluoresced Lyα clouds around quasars (e.g. Cantalupo et al., 2005; Adelberger et al., 2006; Gonçalves et al., 2008). The novel modelling and observational techniques discussed in this thesis aim to establish limits on this critical ionising flux, and to specifically analyse the observations around quasar PKS 0424-131.

The radiative suppression of dwarf galaxies ($T_{\rm vir} \leq 10^4$ K) has been studied extensively (e.g. Babul & Rees, 1992; Efstathiou, 1992; Thoul & Weinberg, 1996; Kepner et al., 1997; Barkana & Loeb, 1999; Kitayama et al., 2000, 2001) to determine if the ionising background that turns on during the EoR could have suppressed the formation of smaller galaxies, thereby skewing the statistics of observed galaxy size number densities. These models suggest that higher IGM temperatures found during the EoR in these ionised regions raised the virial temperature required for gas accretion onto dark matter haloes (Dijkstra et al., 2004), greatly increasing the critical mass required to form galaxies. This process of raising the minimum halo mass for galaxy formation is thought to have played a crucial role in the transition to an ionised IGM (Gnedin, 2000), and therefore learning how this mechanism works is vital to understanding the epoch of reionisation (Iliev et al., 2005).

The ionisation rate around PKS 0424-131 is calculated to be approximately 10^3 times the $z = 2.2$ background at the virial radius of the halo hosting the quasar, and still 80 times the background at ~3.5 times this distance. This is far in excess of the ionising flux range in the radiative transfer and hydrodynamical simulations used to model the reionisation epoch. This increased ionisation rate, coupled with the increased clustering of galaxies around quasars, suggest that the environments around PKS 0424-131 and similarly sized quasars are a perfect laboratory for determining the background ionisation rate required to suppress star formation.

Kashikawa et al. (2007) modelled the increased ultraviolet (UV) intensity in the vicinity of luminous quasars, specifically to study the dependence of galaxy formation on incident ionising radiation. They investigated the dearth of Lyα emitters near a large central quasar at $z = 4.9$ using hydrodynamical simulations that modelled UV fields of similar strength to those expected around PKS 0424-131. They found that the onset of nearby galactic star formation can be delayed by the increased UV intensity around a quasar, but that collapsed haloes are unaffected by the increased UV. Specifically, they found that galaxies with $T_{\rm vir} \sim 10^5$ K can be delayed from forming stars by $\sim 10^8$ years in environments with a UV field ~ 100 larger than the background. In contrast, galaxies with a $T_{\rm vir}$ greater than 10^6 K are unaffected by an enhanced UV intensity, even when the intensity is $\sim 10^3$ times that of the background.

Without properly modelling the IGM around PKS 0424-131 in the above scenario, it is impossible to distinguish the ionising suppression of galaxy formation from an IGM induced selection bias caused by using LAEs to trace galaxy populations. This thesis presents a novel semi-analytic model of the IGM in the vicinity of a quasar, and reinforces the scenario laid out above by ruling out any strong observational bias caused by the opacity of the IGM.

1.9 The structure of this thesis

The rest of this thesis is divided into five chapters. Chapter 2 describes a model for determining the visible luminosity of high-redshift galaxies by their Lyα emission. This is achieved by modelling the ionisation of the local IGM of a galaxy, both internally by the galaxy itself and externally from the UV background. Chapter 3 builds upon this, modelling the ionisation state of the IGM in a galaxy cluster with a large central quasar. This model accommodates arbitrary survey sizes and flux

limits, returning the expected number of observable Lyα galaxies. Chapter 4 explains the technology behind tunable narrowband filters and details their unique suitability for detecting high-redshift Lyα emission. It also describes observations of quasar environments using a tunable filter conducted to test the modelling performed in previous chapters. Chapter 5 discusses the unique calibration and data reduction processes required for this type of instrumentation, as well as the techniques developed for selecting candidate LAEs from the final science images. Finally, chapter 6 concludes the thesis with a summary of the models and observations presented, and their implications for determining the critical ionising flux required to suppress galaxy formation.

In this thesis distances are measured in megaparsecs (Mpc), where 1 parsec (pc) is defined to be the distance at which an object with a physical width of equal to the mean distance between the Earth and Sun has an observed angular size of one arcsecond. For reference, one parsec is equivalent to ~3.26 light years. To differentiate between co-moving and proper coordinates, the prefixes 'c' and 'p' are used respectively (e.g. cMpc and pMpc).

A standard Λ-CDM cosmology is assumed throughout this thesis, with parameters fit using the WMAP7 results (Komatsu et al., 2011): (Ω_m, Ω_Λ, Ω_b, h, σ_8, n_s) = (0.27, 0.73, 0.046, 0.70, 0.81, 0.96).

Chapter 2

Modelling Lyα galaxies

The objective of this thesis is to constrain the effects of radiative galaxy suppression during the EoR. The environments studied in this thesis are the densely populated galaxy clusters surrounding super-luminous quasars at redshifts 2.2 and 3.3, which mimic the intense background of ionising radiation found during the EoR and are observable with existing instrumentation. If galaxy formation is negatively impacted by these environments, then observations of the Lyα emission in the region will detect fewer galaxies than modelling predicts.

This chapter describes a model to determine the Lyα luminosity emitted by a galaxy, taking into account its local environment, redshift, and host dark matter halo mass. The model makes use of empirical, semi-analytic relationships, and the free parameters of the model are tuned by fitting to existing Lyα galaxy survey data. Most importantly, the IGM in the immediate environs of a galaxy are modelled in detail, both with and without a nearby quasar, to determine what fraction of emitted Lyα photons are observable.

2.1 Galactic Lyα luminosity

The production of Lyα photons is highly correlated with the formation of stars, so the first component of the galactic Lyα model is to determine the star formation rate. In broad strokes, calculating the star formation rate of a galaxy is straightforward: calculate how much of the galaxy's total mass is made of baryonic material that can

form stars, multiply this by how efficiently the galaxy can turn this matter into stars, and finally divide by the amount of time for which the galaxy has been forming stars up to the time of observation. Thus, for a halo with mass m at redshift z, the star formation rate is defined to be:

$$\dot{M}_\star(m,z) = \left(\frac{\Omega_\mathrm{b}}{\Omega_\mathrm{m}} m\right) f_\star \left(\frac{1}{\epsilon_\mathrm{DC}\, t_\mathrm{hub}(z)}\right) \mathrm{M}_\odot\,\mathrm{yr}^{-1}, \tag{2.1}$$

where Ω_b is the universal mass density of baryons, Ω_m is the universal mass density of all matter, m is the total mass of the galaxy, $f_\star$ is the efficiency at which a galaxy forms stars from baryonic mass, ϵ_DC is the star forming lifetime of the average galaxy as a fraction of the Hubble time, and $t_\mathrm{hub}(z)$ is the Hubble time at the observed redshift. The assumed cosmological model defines the constants Ω_b, Ω_m, and the function $t_\mathrm{hub}(z)$, leaving $f_\star$ and ϵ_DC as free parameters.

From the star formation rate of the galaxy the total Lyman continuum flux per unit mass of star formation (Q_H) is calculated by assuming a probability distribution for the sizes of stars formed. This initial mass function (IMF) of stars is calculated empirically by fitting to known stellar distributions. Following the work of Kennicutt (1998) this is done using the traditional Salpeter (1955) IMF, resulting in a fitted relationship of $\dot{M}_\star$ in terms of Q_H:

$$Q_\mathrm{H} = 9.26 \times 10^{52}\, \dot{M}_\star\, \mathrm{s}^{-1}, \tag{2.2}$$

assuming stellar masses ranging from $0.1\,\mathrm{M}_\odot$ to $100\,\mathrm{M}_\odot$. We note that more recently Schaerer (2003) provides a form of the Q_H to $\dot{M}_\star$ relationship which includes a dependence on the assumed IMF gas metallicity. If we assume a high-redshift, low-abundance ($Z = 0.05\,\mathrm{Z}_\odot$) scenario of galaxy formation following Dijkstra et al. (2007), the difference between the calculations in Schaerer (2003) and equation (2.2)

is a factor of 2.26. This value is small enough to be absorbed into the free parameters $f_\star$ and $f_{\rm esc}$ during the luminosity function fitting (section 2.3.1), thereby not affecting our results. Therefore, to avoid any specific assumptions about metallicity we use the simpler Kennicutt (1998) formulation throughout the rest of the calculation.

As the ionising UV photons generated by the galaxy stream out in all directions from their parent stars, a certain fraction of these photons escape the galaxy without first being absorbed ($f_{\rm esc}$). Of the ionising photons that do not escape the galaxy, two out of every three are assumed to be converted to Lyα (Osterbrock, 1989), giving the following equation for the Lyα luminosity ($L_{{\rm Ly}\alpha}$) as a function of $Q_{\rm H}$:

$$L_{{\rm Ly}\alpha} = 0.68\, h_{\rm p}\, \nu_{{\rm Ly}\alpha}\, (1 - f_{\rm esc})\, Q_{\rm H}\, {\rm erg\,s^{-1}}, \tag{2.3}$$

where $h_{\rm p}$ is the Planck constant, and $\nu_{{\rm Ly}\alpha}$ is the frequency of a Lyα photon.

Combining equations (2.1) to (2.3) gives us a final expression for $L_{{\rm Ly}\alpha}$ in terms of the total halo mass and redshift of the galaxy:

$$L_{{\rm Ly}\alpha}(m, z) = 6.30 \times 10^{52}\, h_{\rm p}\, \nu_{{\rm Ly}\alpha}\, f_\star \left(\frac{1 - f_{\rm esc}}{\epsilon_{\rm DC}\, t_{\rm hub}(z)}\right) \left(\frac{\Omega_{\rm b}}{\Omega_{\rm m}} m\right) {\rm erg\,s^{-1}}. \tag{2.4}$$

The three independent parameters $\epsilon_{\rm DC}$, $f_\star$, and $f_{\rm esc}$ are assumed to be mass independent for the galaxies in our model but will vary with some degree depending on the observed redshift. The fitting of these parameters to empirical observations will be discussed in section 2.3.1.

2.2 Lyα transmission

The Lyα photons produced at each galaxy, as calculated by equation (2.4), must traverse the IGM to arrive at our telescopes. The varying densities of neutral hydrogen gas (H I) in the IGM can severely impact the observability of the source galaxies. In-

transit photons emitted by a distant galaxy will redshift to longer wavelengths, and as they do the photons blueward of the Lyα wavelength ($\lambda_{\mathrm{Ly}\alpha}$) will eventually redshift through Lyα resonance. At this point they can be easily absorbed and scattered by the neutral hydrogen atoms onto a new random trajectory. Therefore a careful analysis of the transmission of Lyα photons through the IGM is a critical component of any model of a galaxy's observable Lyα luminosity, with a final goal of calculating the fraction of Lyα photons that make it to our telescopes through the IGM ($\mathcal{T}_{\mathrm{IGM}}$).

To determine the impact that the IGM has on the transmission of Lyα photons we must calculate the neutral fraction of hydrogen (χ_{IGM}) in the IGM in the vicinity of the emitting galaxy. To do this we make extensive use of the model outlined in Dijkstra et al. (2007). Following their work, we write equations for the density profile (ρ_{IGM}) and radial velocity (v_{IGM}) of the gas in the IGM, using the halo infall calculations of Barkana (2004):

$$\begin{aligned}
\rho_{\mathrm{IGM}}(r, r_{\mathrm{vir}}) &= \begin{cases} 20\,\bar{\rho}\,(r/r_{\mathrm{vir}})^{-1} & r < 10\,r_{\mathrm{vir}}, \\ \bar{\rho}\,[1 + \exp\,(2 - r/5\,r_{\mathrm{vir}})] & r \geq 10\,r_{\mathrm{vir}}, \end{cases} \\
v_{\mathrm{IGM}}(r, r_{\mathrm{vir}}) &= \begin{cases} \left(\frac{r - r_{\mathrm{vir}}}{9\,r_{\mathrm{vir}}}\right)[H(z)\,r] - v_{\mathrm{circ}} & r < 10\,r_{\mathrm{vir}}, \\ H(z)\,r & r \geq 10\,r_{\mathrm{vir}}, \end{cases}
\end{aligned} \tag{2.5}$$

where r is the distance from the centre of the halo, r_{vir} and v_{circ} are the radius of dark matter virialisation and the circular velocity of the virialised dark matter within the halo, and $H(z)$ is the Hubble parameter at redshift z.

Since the emitting galaxy is rotating, the shape of the Lyα line broadens slightly. The assumed shape of this Doppler-broadening is Gaussian, with its width set by the assumed dark matter circular velocity following Dijkstra et al. (2007). Subsequent work in this field by Dijkstra & Wyithe (2010) using more advanced simulations has

shown that galactic outflows of H I modify the Lyα spectral line shape and decrease the impact of the IGM on transmission, implying that our simple Gaussian model is a conservative calculation of $\mathcal{T}_{\rm IGM}$.

The density profile from equation (2.5) is combined with the assumed flux of ionising photons from the emitting galaxy along with any contributing external ultraviolet photon sources. The external sources of ionisation are combined in the hydrogen ionisation rate Γ and, without a nearby quasar or galaxy, will equal the z-dependent ultraviolet photon background $\Gamma_{\rm BG}$. These internal and external sources of ionising flux are used to get a distance dependent $\chi_{\rm IGM}(r;\Gamma)$. These values are then combined with the shape of the broadened Lyα line to give the total opacity of photons along the line-of-sight to our telescope as a function of their wavelength λ:

$$\tau(\lambda;\Gamma) = \int_{r_{\rm vir}}^{\infty} {\rm d}r \; \rho_{\rm IGM}\,(r) \;\; \chi_{\rm IGM}\,(r;\Gamma) \;\; \sigma_{{\rm Ly}\alpha}\,[\lambda, v_{\rm IGM}\,(r)], \tag{2.6}$$

where $\sigma_{{\rm Ly}\alpha}$ is the absorption cross-section for the Doppler-broadened Lyα emission line from the rotating galaxy, evaluated at wavelength λ, and blueshifted by the velocity field $v_{\rm IGM}$.

Equation (2.5) assumes a smooth distribution of H I in the IGM, rather than a more physical model that includes over- and under-dense clumps of H I. The over-dense clumps along the line-of-sight severely impact Lyα transmission, and to account for this we convolve the opacity from equation (2.6) with an assumed IGM density fluctuation distribution, following the simulated distributions in Miralda-Escudé et al. (2000). The resulting function, $\langle {\rm e}^{-\tau}\rangle(\lambda)$, gives the fraction of photons emitted at wavelength λ that are transmitted through the IGM without being scattered out of the line-of-sight. Finally, we integrate the function $\langle {\rm e}^{-\tau}\rangle(\lambda)$ over the range of wavelengths making up the broadened Lyα line to arrive at the final fractional trans-

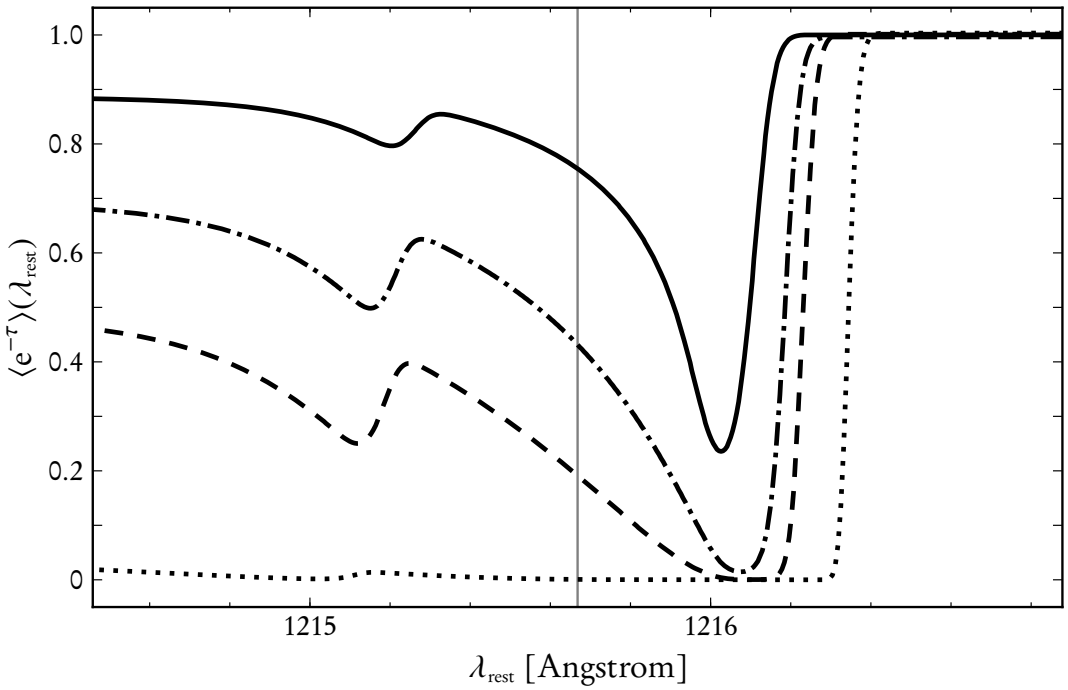

Figure 2.1: The fraction of Doppler-shifted Lyα photons transmitted through the IGM from a galaxy with total mass $10^{11}\,M_\odot$ as a function of wavelength for field conditions at redshifts (from top to bottom) $z = 2.2$, 3.1, 3.7, and 5.7. The integrated transmission across the broadened Lyα for each redshift is (from top to bottom) $\mathcal{T}_{IGM} = 0.74$, 0.48, 0.31, and 0.13. For reference the thin vertical line is the intrinsic $\lambda_{Ly\alpha}$.

mission, $\mathcal{T}_{IGM}$:

$$\mathcal{T}_{IGM}(\Gamma) = \frac{\int d\lambda \, \langle e^{-\tau} \rangle (\lambda) \, J(\lambda)}{\int d\lambda \, J(\lambda)}, \tag{2.7}$$

where Γ is the external hydrogen ionisation rate incident on the galaxy, and $J(\lambda)$ is the flux of the galaxy as a function of wavelength.

Figure 2.1 shows $\langle e^{-\tau} \rangle (\lambda)$ across the width of the rest frame Lyα line for a galaxy with mass $10^{11}\,M_\odot$ at four redshifts, $z = 2.2$, 3.1, 3.7, and 5.7. The different assumed IGM properties at these redshifts lead to corresponding integrated transmission fractions of $\mathcal{T}_{IGM} = 0.74$, 0.48, 0.31, and 0.13. For reference the vertical line is $\lambda_{Ly\alpha}$. The sharp drop in transmission around 1216 Å is caused by the blueshifted Lyα resonance as seen by photons escaping the galaxy through infalling hydrogen gas

from the IGM. Between 1215 Å and 1216 Å the combined ionisation rate provided by the internal ionisation of the galaxy and Γ_{BG} are able to decrease the opacity of the nearby IGM to Lyα photons causing the blueward wavelength roll-up in $\langle e^{-\tau} \rangle(\lambda)$. Γ_{BG} and the mean free path of UV photons (r_{mfp}) decreases with redshift, causing the roll-up to become less pronounced as the redshift increases, and to almost disappear in the $z = 5.7$ curve[1].

The shape of the transmission curve changes as the model components evolve with redshift. The biggest contributions come from the mean hydrogen density, which decreases from $5.8 \times 10^{-5}\,\mathrm{cm}^{-3}$ at $z = 5.7$ to $6.1 \times 10^{-6}\,\mathrm{cm}^{-3}$ at $z = 2.2$, and Γ_{BG}, which increases from $0.34 \times 10^{-12}\,\mathrm{s}^{-1}$ at $z = 5.7$ to $1.20 \times 10^{-12}\,\mathrm{s}^{-1}$ at $z = 2.2$ (Bolton & Haehnelt, 2007). The interplay between these two parameters causes the IGM transmission fraction to increase by a factor of 6 between redshifts 5.7 and 2.2. This illustrates the sensitivity of the Lyα transmission to these two environmental factors, and motivates the idea that the quasar environment may be reducing the transmission of nearby Lyα emitters by a significant amount.

Figure 2.2 shows $\langle e^{-\tau} \rangle(\lambda)$ convolved with an assumed Lyα line profile to simulate the continuum subtracted spectrum for a galaxy with total mass $10^{11}\,M_\odot$ at $z = 2.2$ in different background environments. The dotted curve is the original Lyα line shape assuming perfect transmission. The solid curve is the transmitted line shape at $z = 2.2$, assuming a mean ρ_{IGM} of $6.09 \times 10^{-6}\,\mathrm{cm}^{-3}$ and a Γ_{BG} of $1.2 \times 10^{-12}\,\mathrm{s}^{-1}$. The sharp absorption feature around 3852 Å is the blueshifted Lyα resonance as seen by photons escaping the galaxy through infalling hydrogen gas from the IGM. With a large enough UV flux from galactic and background sources, the neutral fraction of the IGM in the vicinity of the galaxy is lowered considerably.

[1]Note that the $z = 5.7$ curve has no special treatment to account for damped absorption resulting from the denser IGM expected in the high-redshift universe. Applying this model to high-redshift quasars will require a fuller accounting of the unique features of the high-redshift IGM.

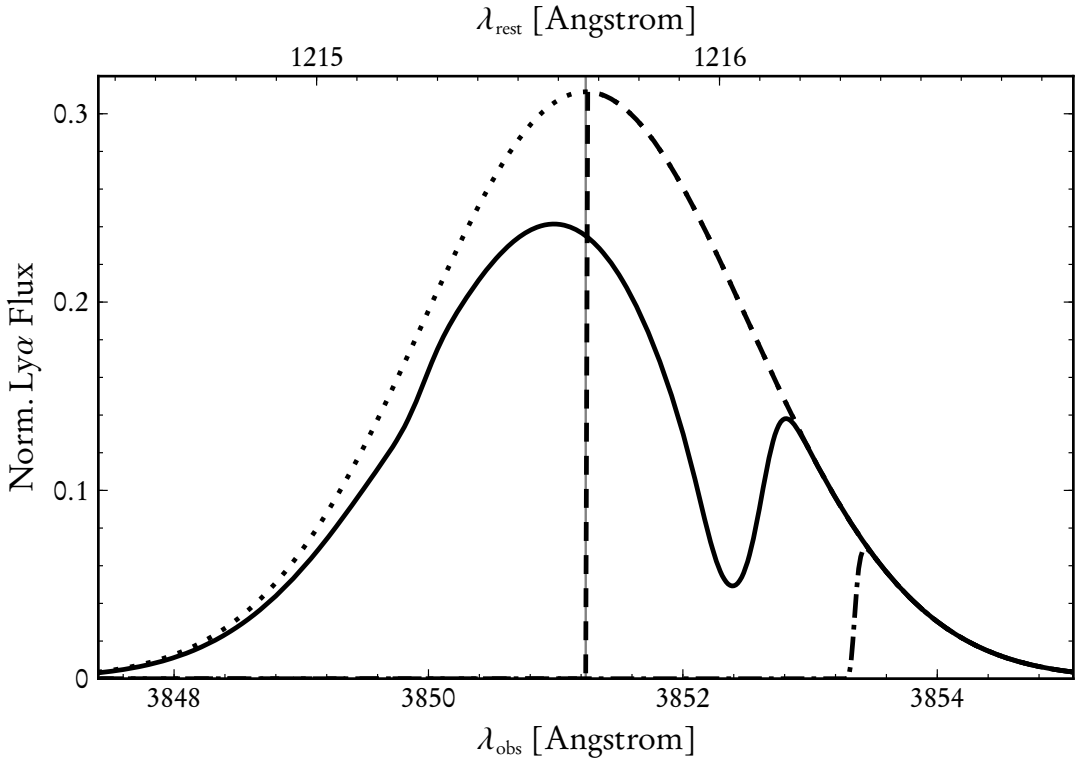

Figure 2.2: Lyα line shapes for a $10^{11}\,M_\odot$ galaxy at $z = 2.2$ under different assumptions about its local IGM. The dotted curve is the original Lyα line shape, the dashed curve is the transmitted line shape with the Gunn-Peterson approximation, the solid curve is the transmitted line shape assuming a mean ρ_{IGM} and Γ_{BG} at $z = 2.2$, and the dash-dotted curve assumes a fully opaque and infalling IGM. For reference the thin vertical line is the intrinsic $\lambda_{Ly\alpha}$.

This results in an increased transmitted fraction of the intrinsic Lyα luminosity of the galaxy. Without a strong UV flux, the entire line blueward of this shifted resonance is scattered out of the line-of-sight, making the integrated transmission far lower as seen in the dash-dotted curve. For comparison we also show the Gunn-Peterson (Gunn & Peterson, 1965) approximation in the dashed curve that assumes that the entire line blueward of rest frame $\lambda_{Ly\alpha}$ is scattered.

Recent work by Laursen et al. (2011) calculated $\mathcal{T}_{IGM}$ using a sophisticated hydrodynamics code that accounts for radiative transfer and interstellar resonant scattering. Our results are consistent with the lower end of their $\mathcal{T}_{IGM}$ values for similar

conditions. This implies that the much more easily calculated semi-analytic $\mathcal{T}_{\rm IGM}$ values used in this work are a conservative assessment of $\mathcal{T}_{\rm IGM}$.

2.3 Fitting free parameters

In order to use $L_{{\rm Ly}\alpha}$ as calculated by equation (2.4) in our models we must first fit the free parameters $\epsilon_{\rm DC}$, $f_\star$, and $f_{\rm esc}$. We do this empirically by using our calculated $L_{{\rm Ly}\alpha}$ and $\mathcal{T}_{\rm IGM}$ to construct a modelled luminosity function for Lyα galaxies and then compare this to observed data. A luminosity function is simply a curve that fits observed galaxy number densities and luminosities at a particular wavelength, in our case $\lambda_{{\rm Ly}\alpha}$. These functions evolve with redshift along with the overall complexion of galaxies, and so fitting the free parameters in our model with these observed functions ties them to a specific epoch. The work of Ouchi et al. (2008) in this space provides us with observed Lyα and UV-continuum (~1500 Å) functions at multiple redshifts, and allows us to fit our free parameters to the specific epoch of our observations.

To make use of the additional dataset provided by the UV-continuum luminosity function we need an equation analogous to equation (2.4) to provide a galaxy's UV-continuum. This is done using an empirical relationship between star formation rate and rest-frame UV-continuum luminosity ($L_{\lambda,{\rm UV}}$) as calculated by Kennicutt (1998):

$$L_{\lambda,{\rm UV}} = 7.1 \times 10^{27}\, f_{\rm dust}\, \dot{M}_\star \,{\rm erg\,s^{-1}\,Hz^{-1}}, \tag{2.8}$$

where $f_{\rm dust}$ is the fraction of UV-continuum luminosity that is not absorbed by dust in the galaxy. We assume $f_{\rm dust}$ to be luminosity independent and fit this as an additional free parameter in our model (Dayal & Ferrara, 2011). While this does add a fourth free parameter to our model, the additional constraints provided by the

UV-continuum luminosity data are worth the added complexity. We should note that we do not explicitly account for dust extinction in our treatment of $L_{\mathrm{Ly}\alpha}$ since any pre-IGM effects of dust on $L_{\mathrm{Ly}\alpha}$ are absorbed into f_{esc} while fitting to the Lyα luminosity function.

Combining this expression with equation (2.1) gives us the full relationship between UV-continuum luminosity and our free model parameters:

$$L_{\lambda,\mathrm{UV}}(m,z) = 7.1 \times 10^{27} \left(\frac{f_{\mathrm{dust}}\, f_\star}{\epsilon_{\mathrm{DC}}\, t_{\mathrm{hub}}(z)}\right)\left(\frac{\Omega_{\mathrm{b}}}{\Omega_{\mathrm{m}}} m\right) \mathrm{erg\,s^{-1}\,Hz^{-1}}. \tag{2.9}$$

Finally, to compare with the UV-continuum luminosity function in Ouchi et al. (2008), this is converted to an absolute AB magnitude[2]:

$$\mathrm{M_{AB}}(m,z) = -2.5 \log_{10}\left[L_{\lambda,\mathrm{UV}}(m,z)\right] + 51.6. \tag{2.10}$$

2.3.1 *Galactic Lyα and UV luminosity functions*

We constrain our Lyα model parameters ϵ_{DC}, $f_\star$, and f_{esc} by fitting the Lyα and UV-continuum differential luminosity functions presented in Ouchi et al. (2008) using the luminosity models presented above. For each luminosity bin in the observed Lyα and UV-continuum luminosity functions we determine the galaxy halo mass, m, required to generate that luminosity by inverting equations (2.4) and (2.10) respectively. This mass is then used to obtain the halo number density for that luminosity bin using the extended Press-Schechter mass function, $\mathrm{d}n/\mathrm{d}m$ (Sheth et al., 2001). This halo number density is then converted to a galaxy number density by assuming that only a fraction ϵ_{DC} of the haloes are occupied by star forming galaxies in the observed epoch, and therefore emitting a detectable $L_{\mathrm{Ly}\alpha}$ and $L_{\lambda,\mathrm{UV}}$. This

[2]See section 5.4.1 for a detailed discussion of the AB magnitude system.

Table 2.1: Best fit parameters for modelled Lyα and UV luminosity functions in Ouchi et al. (2008).

$\epsilon_{\rm DC}$	$f_\star \times 10^{-2}$	$f_{\rm esc} \times 10^{-2}$	$f_{\rm dust}$	$\chi^2_{\rm tot}/d$ ⋆	$\chi^2 \gtrsim \chi^2_{\rm tot}$ †
0.4	7.7	1.45	0.22	1.90	4 %
0.6	8.4	1.15	0.24	1.32	21 %
0.8	8.9	0.81	0.26	1.00	44 %
1.0	9.3	0.56	0.28	0.82	61 %

⋆ $d = 10$ is the degrees of freedom in the fit.
† Probability that a random χ^2 will be greater than $\chi^2_{\rm tot}$.

yields the following equations for the differential Lyα and UV-continuum luminosity functions:

$$\begin{aligned} n_{\rm Ly\alpha}(\mathcal{T}_{\rm IGM} \times L_{\rm Ly\alpha}) &= \epsilon_{\rm DC} \frac{{\rm d}n}{{\rm d}m} \frac{{\rm d}m}{{\rm dlog}_{10}L}, \\ n_{\rm UV}(M_{\rm UV}) &= \epsilon_{\rm DC} \frac{{\rm d}n}{{\rm d}m} \frac{{\rm d}m}{{\rm d}M_{\rm UV}}, \end{aligned} \tag{2.11}$$

where $n_{\rm Ly\alpha}$ is the number density of Lyα galaxies with luminosities between $\log_{10}L$ and $\log_{10}L + {\rm dlog}_{10}L$, and $n_{\rm UV}$ is the number density of UV galaxies with AB magnitudes between $M_{\rm UV}$ and $M_{\rm UV} + {\rm d}M_{\rm UV}$.

Both the Lyα and UV-continuum luminosity functions are fit simultaneously by comparing to the data points in Ouchi et al. (2008). The $z = 3.1$ luminosity function is the closest in their dataset to the observational redshifts we will analyse in chapter 3, namely $z = 2.2$ and 3.3, and is used for the fitting in this section. The combined value $\chi^2_{\rm tot} = \chi^2_{\rm Ly\alpha} + \chi^2_{\rm UV}$ is minimised by varying $f_\star$, $f_{\rm esc}$ (Lyα), $f_{\rm dust}$ (UV) for fixed values of $\epsilon_{\rm DC}$. The parameter $\epsilon_{\rm DC}$ is highly degenerate in our model and so the resultant best fits for a range of values are presented in table 2.1.

Figure 2.3 shows our model fits for the $z = 3.1$ Lyα and UV-continuum lumin-

osity functions presented in Ouchi et al. (2008). Best fit curves are shown with fixed values for the degenerate $\epsilon_{\rm DC}$ parameter corresponding to the upper and lower range of values that are in agreement with the data, $\epsilon_{\rm DC} = 0.4$ and 1.0. There are 14 binned data points in total, 8 for the Lyα luminosity function and 6 for the UV-continuum. This is fit with the 4 fitting parameters for a total of 10 degrees of freedom in the model. We found that $\epsilon_{\rm DC} = 1.0$ yields the best fit for the luminosity functions, with a reduced $\chi^2_{\rm tot}$ of 0.82. This corresponds to a 61 % probability that a randomised set of parameters would produce a larger $\chi^2_{\rm tot}$, and we use this value of $\epsilon_{\rm DC}$ for all calculations on the impact of a quasar environment in section 2.4. The quality of fit decreases monotonically with $\epsilon_{\rm DC}$, and we find that below a value of 0.4 the fit is in significant disagreement (< 4 %) with the data.

As a further check, we calculated and compared Lyα equivalent widths (EW) from our model to the mean observed at $z = 3.1$ in Ouchi et al. (2008). From their spectroscopic and photometric samples Ouchi et al. (2008) calculated a mean EW of 102 Å and 130 Å respectively. Our best fit model has a mean EW of 120 Å, in good agreement with these observations. Moreover, because the calculation of EW is proportional to the expression $\mathcal{T}_{\rm IGM}(1 - f_{\rm esc})/f_{\rm dust}$, this is independent evidence of a robust fit of our parameters to observation. Our range of $f_{\rm dust} = 0.22$ to 0.28 also matches with previous results from Bouwens et al. (2009) who inferred a range of 0.12 to 0.29 at $z \sim 2.5$ and more recent results in Blanc et al. (2011) who found this parameter to be between 0.20 to 0.30.

We noted previously that all of the constraints on our parameters are obtained by fitting to the $z = 3.1$ luminosity functions, and that this will be applied to observed environments at redshifts $z = 2.2$ and 3.3 in later chapters. Current published Lyα luminosity functions at $z < 3$ still suffer from cosmic variance (see Blanc et al., 2011, and references therein) and there exist no accompanying UV-continuum luminosity

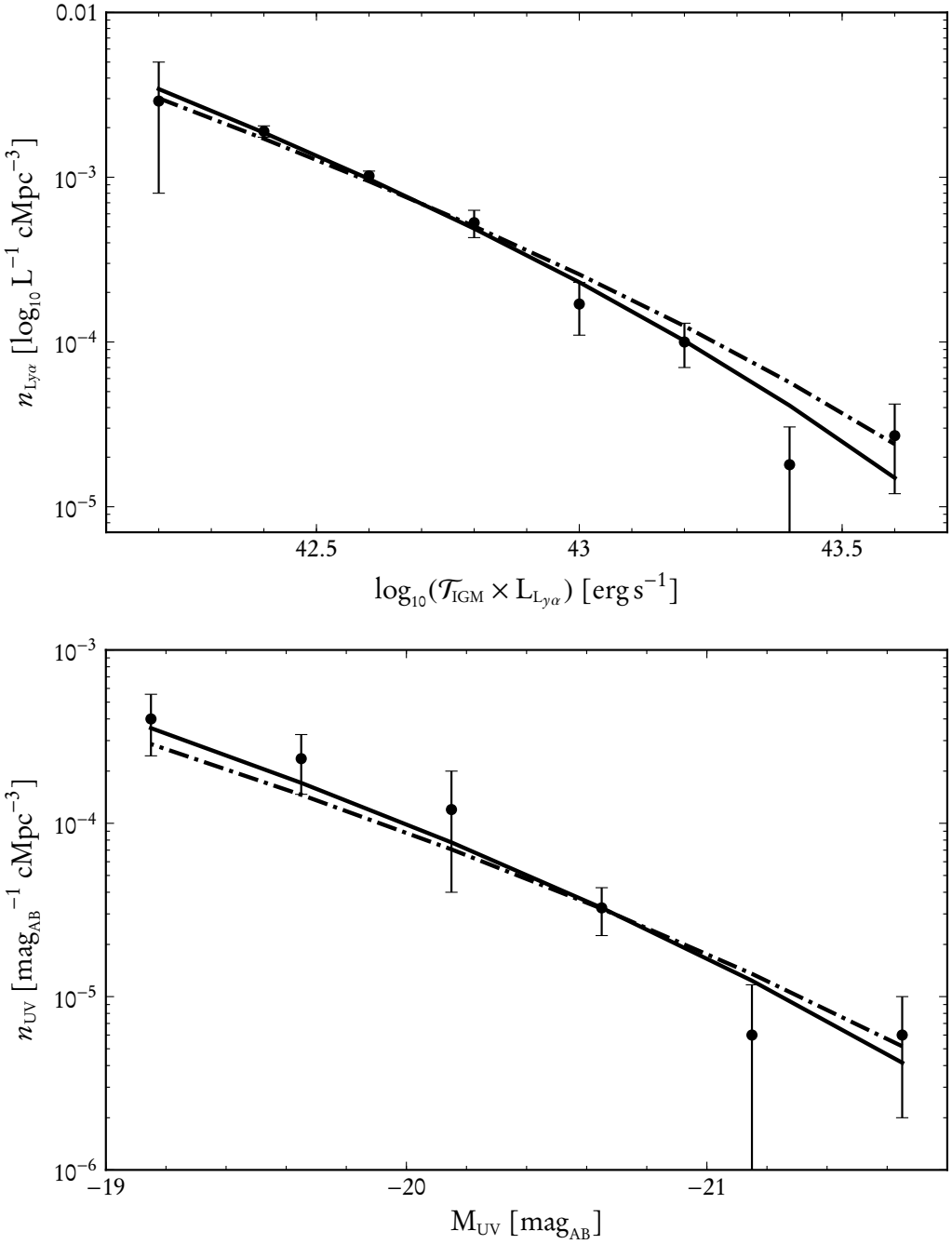

Figure 2.3: Lyα (*upper panel*) and UV-continuum (*lower panel*) fits to $z = 3.1$ differential luminosity functions for two values of ϵ_{DC}. The points and error bars are from Ouchi et al. (2008), figures 16 (upper panel) and 22 (lower panel). The best and worst fit values of ϵ_{DC} are plotted, $\epsilon_{DC} = 1.0$ (solid curves) and $\epsilon_{DC} = 0.4$ (dash-dotted curves), with a reduced χ^2_{tot} of 0.82 and 1.90 respectively. Intermediate values of ϵ_{DC} produce fits that lie between these two curves.

functions at these lower redshifts. Therefore fitting to data from $z = 3.1$ is the best that can be done to constrain the free parameters in the model the redshifts of interest.

Our model assumes long-term continuous galactic star formation for simplicity. Recent work by Sharp & Bland-Hawthorn (2010) showed that star formation is impulsive on timescales less than ten million years, and that for active galactic nuclei the timescales are much longer ($>10^7$ yr) corresponding to a greater than 3 cMpc light crossing time between cycles of star formation. This indicates that more sophisticated simulations will need a $\epsilon_{\rm DC}$ equivalent to multiples of 10^7 yr to be consistent with observation, and that our modelling of the ionising field around a quasar as a continuous event is justified on the scales we consider in this thesis.

It is therefore important to note that recent observations do show evolving properties of Lyα emitters with redshift. In particular the EW distribution at $z = 2.3$ (Nilsson et al., 2009) is described by a steeper exponential function than at $z = 3.1$ (Gronwall et al., 2007), yielding a base EW at $z = 2.3$ that is roughly two-thirds of the value found at $z = 3.1$. This suggests that Lyα photons are more difficult to detect relative to the UV-continuum from $z = 2.3$ galaxies than those emitted from $z = 3.1$. Therefore, to match the smaller $z = 2.3$ mean EW would require an increase in our $f_{\rm dust}$ and/or $f_{\rm esc}$ parameters. Without a matching set of Lyα and UV-continuum luminosity functions at this lower redshift we can only conjecture on exactly how this would affect our free parameters. Changing only $f_{\rm esc}$ to match this reduced EW would have the largest effect on our results. We therefore ran our simulations with this lower $f_{\rm esc}$ and found that the detected number of Lyα emitting galaxies was lowered by 35 %, but that this did not change the results shown in chapter 4. Throughout the rest of this work the fitted parameters in table 2.1 are used.

2.4 Quasar environmental effects

The main component of our model that goes beyond the single galaxy models in Dijkstra et al. (2007) concerns the environmental effects contributed by a nearby quasar. The same mechanisms that cause a galaxy to impact the density and ionisation of its local IGM also cause a quasar to increase these values on a much larger scale. In our model, the impact of a quasar amounts to a local boost to the background levels of $\rho_{\rm IGM}$ and $\Gamma_{\rm BG}$ felt by the galaxy, and can have a significant impact on the Lyα line shape and $\mathcal{T}_{\rm IGM}$.

We compute these two effects semi-analytically by parametrising a quasar by its observed redshift ($z_{\rm Q}$) and its B-band (centred on 4420 Å) apparent magnitude ($m_{\rm B}$). We first calculate the intrinsic B-band luminosity of the quasar relative to solar levels using $m_{\rm B}$ and $z_{\rm Q}$:

$$\begin{aligned} M_{\rm B} &= m_{\rm B} - 5\left[\log_{10} D_{\rm L}(z_{\rm Q}) - 1\right], \\ L_{\rm B} &= 10^{0.4\left(M_{\odot,\rm B} - M_{\rm B}\right)} \mathrm{L}_{\odot,\rm B}, \end{aligned} \tag{2.12}$$

where $D_{\rm L}$ is the luminosity distance to the quasar measured in parsecs, $M_{\odot,\rm B}$ is the solar B-band absolute magnitude, and $\mathrm{L}_{\odot,\rm B}$ are units of solar B-band luminosity.

If we then assume that the quasar is shining at the Eddington limit we are able to find the black hole mass required to emit at the observed luminosity. From this we infer the mass of the dark matter halo hosting the quasar following Wyithe & Loeb (2005):

$$\begin{aligned} M_{\rm bh} &= 1.75 \times 10^{-4}\, L_{\rm B}\, \mathrm{M}_\odot \\ M_{\rm halo} &= 1.15 \times 10^{3}\, \zeta(z_{\rm Q})^{-1/2} \left(1 + z_{\rm Q}\right)^{-3/2} \left(\frac{10^{12}\,\mathrm{M}_\odot}{M_{\rm bh}}\right)^{2/5} M_{\rm bh}, \end{aligned} \tag{2.13}$$

where $\zeta(z_{\rm Q})$ is composed of constants defined by the assumed cosmological model.

Combining equations (2.12) and (2.13) yields a final semi-analytic calculation of the host dark matter halo for a quasar given its observed redshift and B-band apparent magnitude:

$$M_{\rm halo}(m_{\rm B}, z_{\rm Q}) = 2.55 \times 10^4 \, \zeta(z_{\rm Q})^{-1/2} \left(1 + z_{\rm Q}\right)^{-3/2} \times \left(10^{5\log_{10} D_{\rm L}(z_{\rm Q}) - m_{\rm B} + M_{\odot,{\rm B}}}\right)^{6/25} {\rm M}_\odot. \quad (2.14)$$

From the host dark matter halo mass of the quasar we can calculate its virial radius $r_{\rm Q,vir}$ and again make use of equation (2.5) to determine the boost to $\rho_{\rm IGM}$ around a nearby galaxy. We first recast the density contribution of the galaxy's halo as a density excess relative to the universal mean IGM density $\bar{\rho}$ at the observed epoch:

$$\Delta\rho(r, r_{\rm vir}) = \rho_{\rm IGM}(r, r_{\rm vir}) - \bar{\rho}. \quad (2.15)$$

This density excess is then added to the underlying density contribution of the quasar to get the total effective density profile used in calculating $\mathcal{T}_{\rm IGM}$.

Thus, for a galaxy at a distance $r_{\rm Q}$ from a quasar with virial radius $r_{\rm Q,vir}$, the combined density of the local IGM a distance r from a galaxy with virial radius $r_{\rm vir}$ is

$$\rho_{\rm gal}(r, r_{\rm vir}) = \rho_{\rm IGM}(r_{\rm Q}, r_{\rm Q,vir}) + \Delta\rho(r, r_{\rm vir}). \quad (2.16)$$

With this formulation, a galaxy that is at the virial radius of the quasar ($r_{\rm Q} = r_{\rm Q,vir}$) has an effective density that ranges from a maximum value of $39\bar{\rho}$ at the galaxy's virial radius ($r = r_{\rm vir}$), to a minimum of $20\bar{\rho}$ at large distances from the galaxy ($r \gtrsim 30 r_{\rm vir}$). For a galaxy well away from the quasar ($r_{\rm Q} \gtrsim 30 r_{\rm Q,vir}$), the effective density ranges from $20\bar{\rho}$ at the galaxy's virial radius down to the mean IGM density $\bar{\rho}$ outside of the galaxy's influence.

To finish the calculation of the transmitted fraction of Lyα through the IGM, we must calculate the ionisation rate of the quasar. We follow the prescription of Schirber & Bullock (2003) and determine the quasar's flux at the Lyman limit ($J_{\rm LL}$) given the B-band luminosity calculated above:[3]

$$\begin{aligned} L_{\rm LL} &= 10^{18.05}\, L_{\rm B}, \\ J_{\rm LL}(r) &= \left(\frac{L_{\rm LL}}{4\pi\, r^2}\right) \frac{1}{4\pi}\, {\rm erg\,s^{-1}\,cm^{-2}\,Hz^{-1}\,sr^{-1}}. \end{aligned} \tag{2.17}$$

This, along with the assumed UV-continuum slope of the quasar and the absorptive cross-section of hydrogen, is used to calculate the number of hydrogen ionisations per second ($\Gamma_{\rm Q}$) as a function of quasar luminosity and distance from the quasar:

$$\Gamma_{\rm Q}(r, L_{\rm B}) \quad = \quad \frac{12.0}{3+\alpha_{\rm UV}} \left(\frac{J_{\rm LL}(r, L_{\rm B})}{10^{-21}\,{\rm erg\,s^{-1}\,cm^{-2}\,Hz^{-1}\,sr^{-1}}}\right) \exp\left(-r/r_{\rm mfp}\right) 10^{-12}\,{\rm s^{-1}}, \tag{2.18}$$

where $\alpha_{\rm UV}$ is the UV-continuum slope of the quasar equal to 1.57 following Schirber & Bullock (2003), and $r_{\rm mfp}$ is proportional to $(1+z)^{-4}$ following Faucher-Giguère et al. (2008). For each galaxy we generate the ionisation field for calculating $\mathcal{T}_{\rm IGM}$ using a two component model using the distance dependent quasar flux in equation (2.18) and a mean ionising background that is redshift dependent.

As an example, figure 2.4 shows the environmental effects on transmission for a $10^{11}\,{\rm M_\odot}$ galaxy 500 kpc p from a nearby quasar. The black curves assume a central quasar matching the properties observed in Francis & Bland-Hawthorn (2004), with an apparent B-band magnitude of 17.6, a corresponding B-band luminosity of $4.4\times10^{13}\,{\rm L_{\odot,B}}$, and inferred black hole and host halo masses of $7.6\times10^{9}\,{\rm M_\odot}$ and

[3]The Lyman limit corresponds to the energy required to fully ionise a hydrogen atom from its ground state, equivalent to the Rydberg constant, and corresponds to a wavelength of $\lambda_{\rm LL} = 912$ Å.

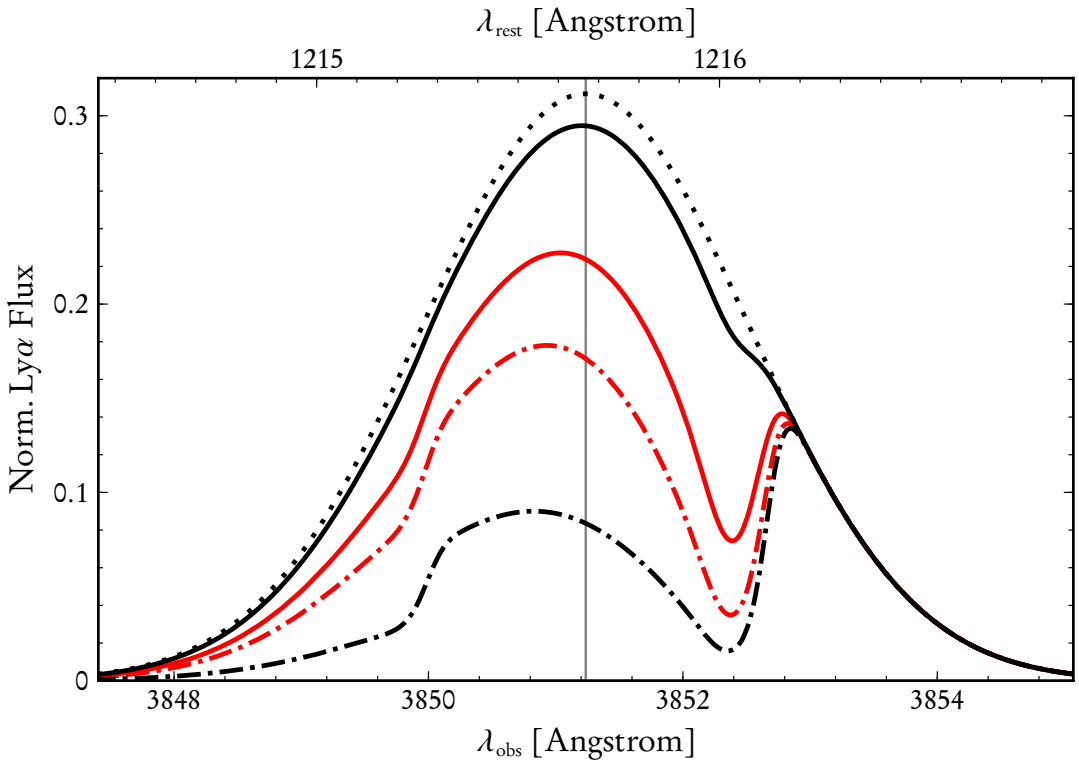

Figure 2.4: Lyα line shapes for a $10^{11}\,M_\odot$ galaxy at $z = 2.2$ in different quasar environments. The dotted curve is the original Lyα line shape, the solid **black** (**red**) curves show the impact of an increased IGM density and UV flux from the nearby quasar with a host halo size of $2 \times 10^{13}\,M_\odot$ ($10^{12}\,M_\odot$). The dash-dotted curves include the increased IGM density but without the quasar's contribution to the incident UV flux. For reference the thin vertical line is the intrinsic $\lambda_{Ly\alpha}$.

$2 \times 10^{13}\,M_\odot$ respectively. The ionising flux generated by the quasar in the vicinity of the galaxy nearly removes the IGM's effect on the Lyα line, yielding a transmission of 0.94, seen in the solid black curve. The black dash-dotted curve shows how the enhanced density of the IGM decreases the transmission when the UV flux is not enhanced by the quasar, resulting in a final transmission of 0.33. This is compared to the dashed curve showing the Lyα line assuming a mean IGM and background UV flux, with a total transmission of 0.74.

For comparison, the red curves show the same galaxy in the vicinity of a much smaller and less luminous quasar, with an apparent B-band magnitude of 23.0, a

corresponding B-band luminosity of $3 \times 10^{11}\,L_{\odot,B}$, and inferred black hole and host halo masses of $5.3 \times 10^{7}\,M_{\odot}$ and $10^{12}\,M_{\odot}$ respectively. For this smaller quasar the UV flux is only sufficient to compensate for the increased density of the IGM. This is seen in the solid red curve, which roughly matches the background curve with a total transmission of 0.71. Since the quasar has a smaller host halo the density boost to the IGM is not as strong at the same radius, which allows for a transmission of 0.56 in the absence of the quasar's UV flux seen in the red dash-dotted curve.

The presence of a nearby quasar also has the potential to ionise any optically thick gas clouds not bound to a galaxy, like those which Francis & Bland-Hawthorn (2004) were originally looking for. The quasar may also boost Lyα emission in a galaxy by externally ionising dense gas on its periphery, even in the absence of observable internal Lyα production. Neither of these scenarios were integrated into our modelling of potential Lyα sources causing our model to be a conservative estimate of expected Lyα emission. As will be shown in chapter 3, the modelled IGM transmission in the field observed in Francis & Bland-Hawthorn (2004) was boosted by the ionisation of its central quasar. The lack of any observed Lyα emission is all the more anomalous given this modelling, even in the absence any treatment of Lyα emission caused by external quasar ionisation. As deeper and more accurate observations are performed using the techniques outlined in the following chapters the modelling of additional sources of Lyα emission will need carefully considered, but for the purposes of this thesis they can be safely omitted.

The exact shape of the radiation fields emitted from a quasar is an open question in the quasar community. Most of the ionisation is emitted by the inner accretion disk of the quasar and is emitted isotropically. If a surrounding dusty torus is present around the accretion disk then the ionisation will be collimated around the spin axis, but even then the ionisation is still likely to be diffused through the volume by

either scattering off dust grains or via Thomson scattering off of electrons (Bland-Hawthorn et al., 1991; Sokolowski et al., 1991). The impact of these effects can be averaged by analysing large surveys containing observations similar to those in Francis & Bland-Hawthorn (2004). This allows for the limiting cases to be described by a dilution factor, $f_{\rm dil}$, representing the fractional solid angle that the radiation field emitted by the quasar permeates, where $f_{\rm dil} = 1$ corresponds to a perfectly isotropic quasar and $f_{\rm dil} = 0$ to a quasar emitting no ionising radiation. In subsequent chapters $f_{\rm dil}$ will be used to model a quasar's ionisation rate across entire galaxy clusters and for the purposes of this work we will mainly use it in calculating upper and lower bounds on visible galaxy counts.

An additional complication in a more realistic model of quasar ionisation is the duty cycle of a quasar's active period since only galaxies exposed to ionising radiation for a sufficient period should be subject to radiative suppression. We will not be directly modelling photo-evaporation and so will make no assumptions about the mechanism or timescales of the quasar induced radiative suppression in this thesis.

2.5 Summary

In this chapter we have laid out the equations and relationships that allow us to determine the transmitted Lyα luminosity from a galaxy in the vicinity of a quasar. These relationships are all semi-analytic models, with parameters obtained by fitting to observable values and to sophisticated numerical models. The main result from this chapter that the observable Lyα luminosity of a galaxy is influenced dramatically in the vicinity of a quasar, and depends strongly on the luminosity and host halo mass of the quasar. In the next chapter we will model the effect of a nearby quasar on the observability of not just a single galaxy, but on an ensemble of galaxies within a quasar-dominated galaxy cluster.

Chapter 3

Modelling Lyα surveys

The equations presented in chapter 2 give us the means to determine the observable Lyα luminosity of a galaxy in the vicinity of a quasar. The procedures laid out in this chapter apply those equations to an ensemble of galaxies in a modelled cosmological volume. We describe the creation of a dark matter scaffolding of the model volume, accounting for assumed clustering bias in constituent dark matter haloes, and the placement of Lyα-emitting galaxies within them. We determine the effects that a centrally placed quasar and other nearby galaxies have on the transmitted fraction of the Lyα luminosity of each modelled galaxy. We describe how to model specific survey volumes and how to account for redshift-space distortions that, if left uncorrected, bias galaxy counts in observations. Finally, we compare the results of this modelling with existing surveys in the literature and motivate the observations and analysis in chapters 4 and 5.

The example figures and calculations presented throughout this chapter contain masses, redshifts, and distances from the Lyα survey volume observed in Francis & Bland-Hawthorn (2004) (hereafter FBH04). A full analysis of that survey volume with the presented model is found in section 3.3.3.

3.1 Creating the dark matter scaffolding

The survey volumes modelled and observed in this thesis contain a quasar at their centre. For the observations taken of these volumes this is by construction; the

volumes are selected only by their luminous quasar, which is placed in the centre of the frame during the observation. When modelling these volumes the quasar is placed at the centre of the computational framework for the expedience afforded by spherical symmetry. However, no assumption is made regarding the location of the quasar within the physical galaxy cluster it inhabits, nor that it is contained within the largest galaxy within the cluster.

The surveys modelled in this thesis are of galaxy clusters containing a single visible quasar housed in a large host galaxy. The other galaxies in the modelled volume are assumed to be star forming galaxies, each of which are assumed to be contained within a dark matter halo with a mass proportional to its luminosity. For simplicity we neglect any additional dark matter structures and any non-star forming galaxies, as our primary focus is in calculating the transmitted Lyα luminosity of galaxies using only their nearby IGM conditions.

We assume an isotropic distribution of dark matter haloes building out from the central quasar-hosting halo in concentric shells of radius r and thickness dr, from $r_{\rm min}$ to $r_{\rm max}$. We assume for simplicity that the central halo is solely occupied by the quasar and accordingly set the minimum shell radius equal to the virial radius of the central halo so that $r_{\rm min} = r_{\rm vir,quasar}$. The largest shell radius $r_{\rm max}$ is dependent on the size of the survey and is set so that it just encloses the entire survey volume. Owing to the magnitude of distances involved the shells are distributed evenly in log-space for ease of plotting and the interpretation of results.

Within each of these radial shells we place dark matter haloes with mass m, ranging from a calculated minimum mass $m_{\rm min}$ – defined as the lowest mass required for a baryonic object to form at the modelled redshift – to a maximum mass $m_{\rm max} = 10^{15}\,{\rm M}_{\odot}$. The specific prescription for the placement of these haloes depends on the simulation technique, as will be discussed in section 3.2. In both the numerical

and analytic treatments, the range of masses is divided equally in log space in steps of $\mathrm{d}m$, and for each step the assumed number density of haloes is provided by the differential mass function for haloes, $\mathrm{d}n/\mathrm{d}m$.

3.1.1 The halo mass function

Formally, the differential mass function for dark matter haloes (hereafter referred to as the halo mass function) is defined as the number of dark matter haloes of a certain mass, m, per unit volume per unit mass, and is denoted by the equation $\mathrm{d}n/\mathrm{d}m$. The dark matter haloes we observe originally began as small overdensities – fluctuations on the order of 10^{-5} in terms of the average gravitational potential – in the pristine dark matter density field seen in observations of the cosmic microwave background. The gravitational collapse of these overdensities produce the large scale dark matter structures that makes up our the scaffolding in our model.

We characterise the size distribution of these overdensities statistically by defining the quantity $\sigma(r)$, the likelihood of finding an isolated sphere of radius r containing a single overdensity:

$$\sigma^2(r) = \frac{1}{2\pi^2} \int_0^\infty k^2 P(k) W^2(k; r)\, \mathrm{d}k, \tag{3.1}$$

where $P(k)$ is the linear power spectrum of fluctuations in the pristine dark matter density field, and $W(k; r)$ is the Fourier transform of a top-hat filtering function representing the size of the isolated sphere. To tie this analytic quantity to observation, $P(k)$ is normalised so that the value $\sigma(r = 8\,\mathrm{Mpc})$ matches the measured value from the assumed cosmology.

We can recast σ in terms of mass if, instead of the radius r, we work with the

mass m assumed to be contained by a sphere at the mean density of the Universe ρ_0:

$$\begin{aligned} r(m) &= \left(\frac{3}{4\pi}\frac{m}{\rho_0}\right)^{\frac{1}{3}}, \\ \sigma(m) &:= \sigma\left[r(m)\right]. \end{aligned} \tag{3.2}$$

Each overdensity exerts a small but continuous gravitational pull on its surroundings. This eventually dominates and collapses the mass within its gravitational influence forming a compact halo. To relate this process to $\mathrm{d}n/\mathrm{d}m$ analytically, we first define the function $f(\sigma, z)$ as the fraction of mass collapsed in haloes per interval in $\log \sigma^{-1}$ space at redshift z normalised to unity; the seemingly odd choice of parametrisation is to ease subsequent calculations. We refer to $f(\sigma, z)$ as the mass function (as distinct from the halo mass function) and its form is defined by the particular prescription of overdensity growth and halo collapse adopted. In this formulation of $f(\sigma, z)$, $\mathrm{d}n/\mathrm{d}m$ is defined to be:

$$\frac{\mathrm{d}n}{\mathrm{d}m}(m, z) = \frac{\rho_0}{m}\frac{\mathrm{d}\log\sigma^{-1}}{\mathrm{d}m} f(\sigma, z), \tag{3.3}$$

where $\mathrm{d}n/\mathrm{d}m$ yields the number density of dark matter haloes, $\mathrm{d}n$, with a mass between m and $m + \mathrm{d}m$.

Press & Schechter (1974) presented a simple analytical formulation of $f(\sigma, z)$ that assumes a random Gaussian overdensity field with linear gravitational growth and a final spherical collapse. The final form for this is compactly written in $\log \sigma^{-1}$ space as:

$$f_{\mathrm{PS}}(\sigma, z) = \sqrt{\frac{2}{\pi}}\frac{\delta_{\mathrm{c}}(z)}{\sigma}\exp\left(-\frac{{\delta_{\mathrm{c}}}^2(z)}{2\sigma^2}\right),$$

where $\delta_{\mathrm{c}}(z)$ is the critical overdensity of collapse extrapolated to redshift z. This was improved upon by Sheth et al. (2001) with the refined assumption that haloes

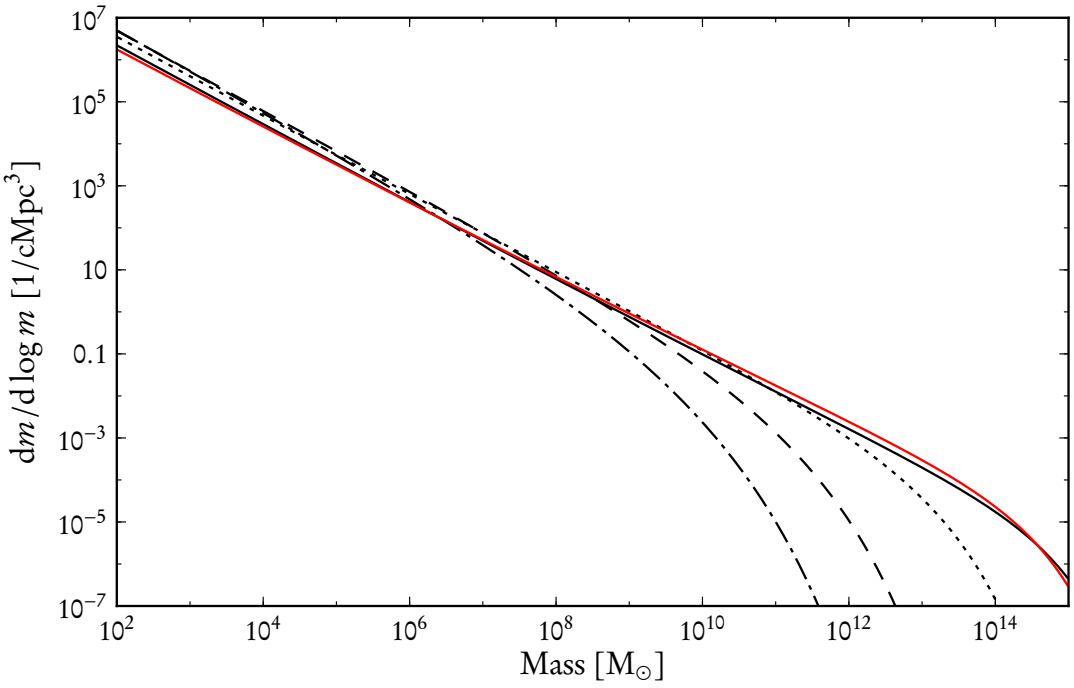

Figure 3.1: Halo mass function of the form $dn/d\log m$ at $z = 0,\ 2.2,\ 6,$ and 10 (the **black** solid, dotted, dashed, and dash-dotted curves respectively) using the $f_{\rm SMT}(\sigma, z)$ mass function. For reference the solid **red** curve shows the halo mass function using $f_{\rm PS}(\sigma, z)$ at $z = 0$.

collapse ellipsodially rather than spherically:

$$f_{\rm SMT}(\sigma, z) = A\sqrt{\frac{2a}{\pi}}\left[1 + \left(\frac{\sigma^2}{a\delta_{\rm c}{}^2(z)}\right)^p\right]\frac{\delta_{\rm c}(z)}{\sigma}\exp\left(-\frac{a\delta_{\rm c}{}^2(z)}{2\sigma^2}\right), \qquad (3.4)$$

where $A = 0.3222$, $a = 0.707$, and $p = 0.3$ are determined by fitting to numerical simulations. $f_{\rm SMT}$ provides better agreement with simulation than $f_{\rm PS}$ and is used in all calculations of dn/dm in this chapter.

Figure 3.1 shows the halo mass function at a number of redshifts in the more easily visualised form $dn/d\log m$, calculated using the $f_{\rm SMT}(\sigma, z)$ mass function. The black solid, dotted, dashed, and dash-dotted curves are calculated at $z = 0,\ 2.2,\ 6,$ and 10 respectively. For completeness the solid red curve is calculated using the $f_{\rm PS}(\sigma, z)$ mass function at $z = 0$. Two competing effects can be seen in the evolution

of the halo mass function with redshift: as redshift decreases the total fraction of dark matter that has settled into a halo increases, causing the low mass end to increase in number density as additional haloes form; at the same time the existing haloes increase in size due to accretion, causing the high-mass end of the curve to increase as haloes migrate from the low-mass end. As a higher fraction of dark matter is contained in haloes, the migration to the high-end dominates the formation of new haloes and the number density of smaller haloes begins to fall. This can be seen by comparing the slope and intercept of the $z = 0$ curve with those from higher redshifts.

More recent work has provided additional formulations of $f(\sigma, z)$ using N-body simulations (Reed et al., 2007)[1] but their usage is beyond the requirements of the analytical formulation presented in this chapter.

3.1.2 *Halo formation bias*

Following the accretion model for halo formation presented in section 3.1.1 it is assumed that the largest haloes at any particular epoch were those that collapsed first. This implies that, for a galaxy cluster with a central quasar, the dominant dark matter halo hosting the quasar collapsed first, followed by the smaller galaxy-hosting haloes. Because these smaller haloes are forming in a region that already contains the strong gravitational field formed by the central halo (which is streaming in higher-than-mean densities of dark matter) their time to collapse is shorter than the mean conditions assumed by $\mathrm{d}n/\mathrm{d}m$. Therefore, to properly build the dark matter scaffolding in our model quasar-dominated galaxy cluster, we need to introduce a positive bias to the calculated halo counts.

[1]The notation presented for describing $\mathrm{d}n/\mathrm{d}m$ in terms of $f(\sigma, z)$ is borrowed from Reed et al. (2007), who provide an introduction to the mathematics and motivation behind the halo mass function.

An analytic treatment of this bias was created by Mo & White (1996), building on the halo collapse formalism first introduced by Press & Schechter (1974). They begin with the two-point dark matter density correlation function:

$$\xi(d, r_1, r_2) = \frac{1}{2\pi^2} \int_0^\infty kP(k) \frac{\sin(kd)}{d} W(k; r_1) W(k; r_2)\, \mathrm{d}k, \tag{3.5}$$

where d is the separation between the two overdensity regions, r_1 and r_2 are the respective radii of the two isolated overdensity spheres, and $P(k)$ and $W(k; r)$ are defined as in equation (3.1). This can be recast in terms of mass following equation (3.2) which allows us to interpret this as the unbiased clustering pattern of overdensities dominating two masses, m_1 and m_2, a distance d apart in the pristine dark matter density field.

Mo & White (1996) then extend this to a later time z by taking into account the linear, gravitationally induced motion of the collapsed dark matter haloes. This yields a redshift-dependent correction to the correlation function:

$$b^2(m_1, m_2, z) = \left[\delta_c(0) + \left(\frac{{\delta_c}^2(z)}{\sigma(m_1)} - 1\right)\right] \left[\delta_c(0) + \left(\frac{{\delta_c}^2(z)}{\sigma(m_2)} - 1\right)\right] {\delta_c}^{-2}(z), \tag{3.6}$$

where $\delta_c(0)$ is the critical overdensity of collapse extrapolated to the present day ($z = 0$). Combining equations (3.5) and (3.6) gives the final linearly-biased correlation function:

$$\xi_L(d, m_1, m_2, z) = b^2(m_1, m_2, z)\, \xi(d, m_1, m_2). \tag{3.7}$$

Figure 3.2 illustrates the boost this formation bias can give to halo number densities on the distance scales used in our models. The black solid, dotted, dashed, and dash-dotted curves represent the fractional increase in likelihood of haloes forming at different distances apart for $z = 0,\ 2.2,\ 3.3,$ and 6 respectively. We can see how as

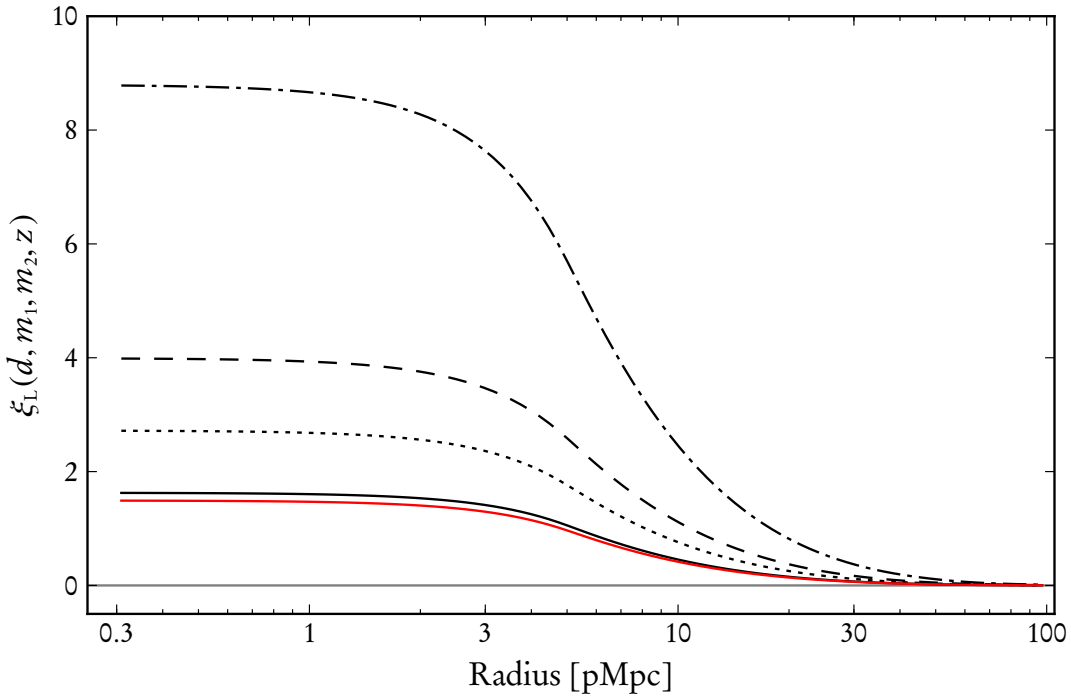

Figure 3.2: Dark matter halo biasing as a function of separation between centres of a halo of $2 \times 10^{13}\,M_\odot$ and $10^{10}\,M_\odot$ at redshifts of $z = 0,\ 2.2,\ 3.3,$ and 6 (the **black** solid, dotted, dashed, and dash-dotted curves respectively). For reference the **red** curve shows the $z = 0$ bias between a halo of $2 \times 10^{13}\,M_\odot$ and a smaller $10^9\,M_\odot$ halo.

compact objects grow in size with decreasing redshift, the likelihood of finding large dark matter haloes in close proximity increases.

Work has been done to extend this analytic approach to the non-linear regime with success (Scannapieco & Barkana, 2002; Iliev et al., 2003), showing a marked positive deviation from the linear theory at short separations. For the separations we are considering in this thesis the linear theory is sufficient and is used throughout our model.

3.1.3 Galaxy occupation counts

Putting together the results from sections 3.1.1 and 3.1.2 we are in a position to begin placing haloes in each concentric radial shell of the scaffolding: dn/dm allows us to

find the mean number density for each halo mass considered in our model; $\xi_{\rm L}$ gives the boost expected for each mass given the separation between a given concentric shell and the central halo; and $4\pi r^2 \mathrm{d}r$ gives the volume of the concentric shell by which to multiply the boosted halo number densities, yielding the mean expected haloes in a given shell. To convert halo counts to galaxy counts we assume that only a fraction $\epsilon_{\rm DC}$ of galaxies are forming stars and thereby emitting an observable $L_{\rm Ly\alpha}$.

Therefore the average number of haloes in a concentric shell with radius r and thickness $\mathrm{d}r$, with mass in the range $m \pm \mathrm{d}m/2$, with a separation of r from the central quasar halo with mass M, and at redshift z is:

$$\mathcal{N}_{\rm gal}(r, m, M, z) = \epsilon_{\rm DC} \frac{\mathrm{d}n}{\mathrm{d}m}(m, z) \left[1 + \xi_{\rm L}(r, m, M, z)\right] (4\pi r^2 \mathrm{d}r). \tag{3.8}$$

This matches the prescription found in §2.1.1 of Dijkstra et al. (2008), which describes the analytical clustering of galaxies around a central dark matter halo but which assumes a non-linear treatment of the separation bias.

3.1.4 Modelling the local IGM

The transmitted fraction of the Lyα luminosity of each galaxy placed in the scaffolding is the quantity of interest. To that end we make use of the formalism in chapter 2 to determine what effect position in the scaffolding has on the transmitted $L_{\rm Ly\alpha}$ of a galaxy.

For each of radial shell in the model we calculate the UV flux of the central quasar using equation (2.18) and combine it with the mean UV background at the modelled redshift. This gives the effective ionising rate[2] incident on each galaxy in

[2]To fully account for all the UV photons incident on a galaxy in the shell the escaped UV photons from each neighbouring galaxy must be considered as well. As we will show in section 3.2.2 this galaxy-galaxy UV contribution is negligible so we will ignore it in this formulation.

the shell, and from this we are able to determine the quasar-enhanced IGM density and IGM neutral fraction as detailed in section 2.4. Finally, we are able to calculate the transmitted Lyα luminosity for each galaxy mass at each radial shell in the model.

3.2 Realising the model

Two approaches were taken when placing the galaxy counts from equation (3.8) into the radial shells: a fully numerical model in which each individual galaxy is placed at a randomised location in the radial shell, and an analytic treatment where the halo counts for each shell calculated above are treated as a non-self-interacting ensemble. The practical difference between these two approaches is that the numerical model accounts for galaxy-galaxy ionisations in the calculation of $\mathcal{T}_{\rm IGM}$ while the analytic model ignores these galaxy-galaxy interactions.

To create concrete realisations of the model, either fully numerical or analytic, we first must quantise the mass range and shell radii range for sampling. We bin the mass range $m_{\rm min}$ to $m_{\rm max}$ in log-space into $n_{\rm m}$ equally spaced bins of width $\mathrm{d}\log(m)$. The radial dimension is similarly split into $n_{\rm r}$ equally spaced bins in log-space of width $\mathrm{d}\log(r)$ over the range $r_{\rm min}$ to $r_{\rm max}$.

We then define the two parameters that shape the size and density of the scaffolding: the redshift at the location of central quasar $z_{\rm Q}$, and its B-band apparent magnitude $m_{\rm Q}$. From these we also calculate $L_{\rm B}$ and $M_{\rm Q}$ via equations (2.12) and (2.14). With these properties defined we are ready to start calculating the values used to determine the observable Lyα for each galaxy in the model.

Since we are dividing up the mass and radial ranges in log-space, while our calculations are all done in real-space, we must first convert each bin value to real-space.

For each radial bin i from 1 to $n_{\rm r}$, we convert from log-space as

$$\begin{aligned} r_{\rm i} &= r_{\rm min} \exp\left[(i - 0.5)\, {\rm d}\log(r)\right], \\ {\rm d}r_{\rm i} &= r_{\rm i} \times 2 \sinh\left({\rm d}\log(r)/2\right), \end{aligned} \tag{3.9}$$

and calculate the following values:

$$\begin{aligned} V_{\rm i} &= 4\pi r_{\rm i}^2\, {\rm d}r_{\rm i}, \\ \Gamma_{{\rm Q\,i}} &= \Gamma_{\rm Q}(r_{\rm i}, L_{\rm B}), \\ \rho_{{\rm gal\,i}}({\rm r}) &= \rho_{\rm gal}({\rm r}, r_{\rm i}), \end{aligned} \tag{3.10}$$

where $V_{\rm i}$ is the volume of the concentric radial shell for the $i^{\rm th}$ bin, and $\Gamma_{\rm Q}$ and $\rho_{\rm gal}$ are defined in equations (2.16) and (2.18) respectively.

Similarly, for each mass bin j from 1 to $n_{\rm m}$, we convert from log-space as

$$\begin{aligned} m_{\rm j} &= m_{\rm min} \exp\left[(j - 0.5)\, {\rm d}\log m\right], \\ {\rm d}m_{\rm j} &= m_{\rm j} \times 2 \sinh\left({\rm d}\log m/2\right), \end{aligned} \tag{3.11}$$

and calculate the following values:

$$\begin{aligned} L_{{\rm Ly}\alpha\,{\rm j}} &= L_{{\rm Ly}\alpha}(m_{\rm j}, z_{\rm Q}), \\ L_{\lambda,{\rm UV\,j}} &= L_{\lambda,{\rm UV}}(m_{\rm j}, z_{\rm Q}), \\ {\rm d}n/{\rm d}m_{\rm j} &= {\rm d}n/{\rm d}m(m_{\rm j}, z_{\rm Q}), \end{aligned} \tag{3.12}$$

where $L_{{\rm Ly}\alpha}$, $L_{\lambda,{\rm UV}}$, and ${\rm d}n/{\rm d}m$ are defined in equations (2.4), (2.9) and (3.3).

For every combination of radial bin i and mass j we calculate:

$$\begin{aligned} \xi_{\mathrm{L}\,\mathrm{ij}} &= \xi_{\mathrm{L}}(r_{\mathrm{i}}, m_{\mathrm{j}}, M_{\mathrm{Q}}, z_{\mathrm{Q}}), \\ \mathcal{N}_{\mathrm{gal}\,\mathrm{ij}} &= \epsilon_{\mathrm{DC}}\, \mathrm{d}n/\mathrm{d}m_{\mathrm{j}}\, \xi_{\mathrm{L}\mathrm{ij}}\, V_{\mathrm{i}}, \end{aligned} \tag{3.13}$$

where ξ_{L} is defined in equation (3.7), and $\mathcal{N}_{\mathrm{gal}_{\mathrm{ij}}}$ is a modulation of equation (3.8).

For each radial shell in the model we take the incident ionising flux from the central quasar, $\Gamma_{\mathrm{Q}\,\mathrm{i}}$, and combine it with the mean ionising background at the modelled redshift, $\Gamma_{\mathrm{BG}}(z_{\mathrm{Q}})$. For the numerical model we add to this the ionising flux contribution incident on a galaxy from every other galaxy in the scaffolding, $\Gamma_{\mathrm{gal-gal}}$, and for the analytic model we ignore this contribution. As we will show in section 3.2.2, the calculation of $\Gamma_{\mathrm{gal-gal}}$ adds considerable complexity to the modelling process and has negligible impact on the calculated galaxy counts.

Combining these terms yields a final external ionising flux incident on a galaxy in the i^{th} radial bin:

$$\Gamma_{\mathrm{all}\,\mathrm{i}} = \Gamma_{\mathrm{Q}\,\mathrm{i}} + \Gamma_{\mathrm{BG}}(z_{\mathrm{Q}}) + \Gamma_{\mathrm{gal-gal}},$$

where $\Gamma_{\mathrm{gal-gal}} = 0$ in the analytical realisations of the model.

3.2.1 Analytical calculation of transmitted Lyα luminosity

Since the analytical calculation ignores galaxy-galaxy interaction, $L_{\mathrm{Ly}\alpha} \times \mathcal{T}_{\mathrm{IGM}}$ is calculated just once for each combined mass and radial bin as

$$L_{\mathrm{Ly}\alpha} \times \mathcal{T}_{\mathrm{IGM}\,\mathrm{ij}} = L_{\mathrm{Ly}\alpha\,\mathrm{j}} \times \mathcal{T}_{\mathrm{IGM}} \left[\Gamma_{\mathrm{all}\,\mathrm{i}}; \rho_{\mathrm{gal}\,\mathrm{i}}(\mathrm{r}), L_{\lambda,\mathrm{UV}\,\mathrm{j}}\right], \tag{3.14}$$

where $\mathcal{T}_{\mathrm{IGM}}$ is defined in equation (2.7), and the calculation for $L_{\mathrm{Ly}\alpha} \times \mathcal{T}_{\mathrm{IGM}\,\mathrm{ij}}$ uses the quasar influenced density $\rho_{\mathrm{gal}\,\mathrm{i}}(\mathrm{r})$ and continuum luminosity $L_{\lambda,\mathrm{UV}\,\mathrm{j}}$ in the embedded

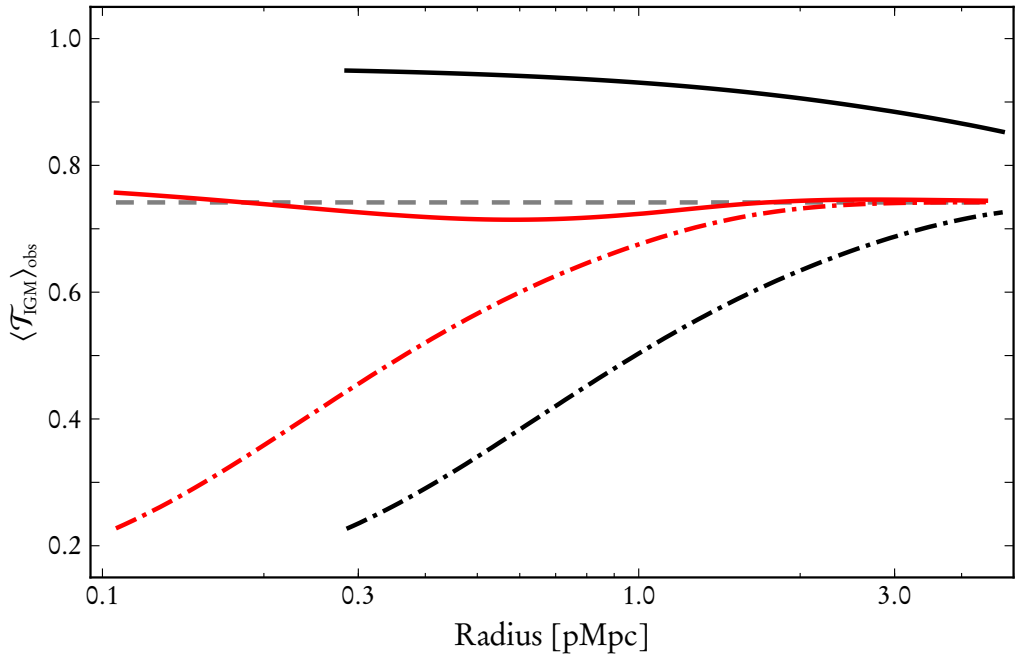

Figure 3.3: Averaged Lyα transmission as a function of distance from a central quasar, modelled with host halo masses of 2×10^{13} $M_\odot$ (**black** curves) and 10^{12} $M_\odot$ (**red** curves). The grey dashed curves assume an average transmission with a mean IGM density and UV flux. The solid curves include the density and UV flux from the nearby quasar and the dash-dotted curves include the increased density but with no UV boost from the quasar.

calculation of τ from equation (2.6).

Figure 3.3 shows an analytical calculation for $\mathcal{T}_{IGM}$ averaged over all observable galaxies at each radial shell, assuming the FBH04 detection limit (see section 3.3.3), as a function of distance from the quasar at $z = 2.2$. As in figure 2.2, the black and red lines represent central quasars with host halo masses of 2×10^{13} $M_\odot$ and 10^{12} $M_\odot$ respectively, the solid and dash-dotted lines show the effects of the quasar with and without the enhanced ionising flux from the central quasar ($f_{dil} = 1$ and $f_{dil} = 0$ respectively). The dashed grey line is the average transmission for a mean IGM. For each quasar the virial radius was used as the minimum radial distance in the model to avoid confusion in halo occupation, where the larger and smaller quasars have a minimum radius of 280 kpc p and 100 kpc p respectively.

For the smaller quasar (red curves) we see that the increased density of the IGM around the quasar and the increased ionisation rate from the quasar compensate for one another, leading to a radial transmission curve that is nearly equal to that of the mean IGM (in grey). The larger quasar (black curves) has a much larger UV flux and is able to ionise the denser IGM efficiently, leading to a transmission roughly 20 % higher than the mean. Assuming that the ionising flux of a quasar is isotropic, this implies that the Lyα transmission in the vicinity of a quasar at $z = 2.2$ is comparable to the mean IGM for modest-sized quasars and is higher for the more luminous quasars. Therefore if $\mathcal{T}_{\rm IGM}$ is the primary factor influencing detection of Lyα emission from galaxies near a luminous quasar, we would expect to see an increase in the number of observable Lyα galaxies in the vicinity of the quasar.

This is shown visually in figure 3.4, which plots the host halo mass for the smallest visible galaxy (again assuming the FBH04 detection limit) against distance from the central quasar. The Lyα luminosity of a galaxy in our model is proportional to host halo mass, and so the host halo mass of the faintest observable galaxy is determined by the Lyα transmission given a fixed flux limit. Thus the minimum host halo curves inversely follow the shape of the transmission curves in figure 3.3. At $z = 2.2$ the calculated background transmission gives the minimum host halo mass to be $9.6 \times 10^{10}\,\mathrm{M}_\odot$, seen in the dashed grey curve. Around the larger quasar the minimum host halo mass ranges between $7.6 \times 10^{10}\,\mathrm{M}_\odot$ and $3.2 \times 10^{11}\,\mathrm{M}_\odot$ and between $9.6 \times 10^{10}\,\mathrm{M}_\odot$ and $3.2 \times 10^{11}\,\mathrm{M}_\odot$ for the smaller quasar.

3.2.2 Numerical calculation of transmitted Lyα luminosity

The first step in the numerical treatment is to place a representative number of haloes in the $j^{\rm th}$ mass bin in each radial shell i based on the calculated value $N_{\mathrm{gal}\,ij}$.

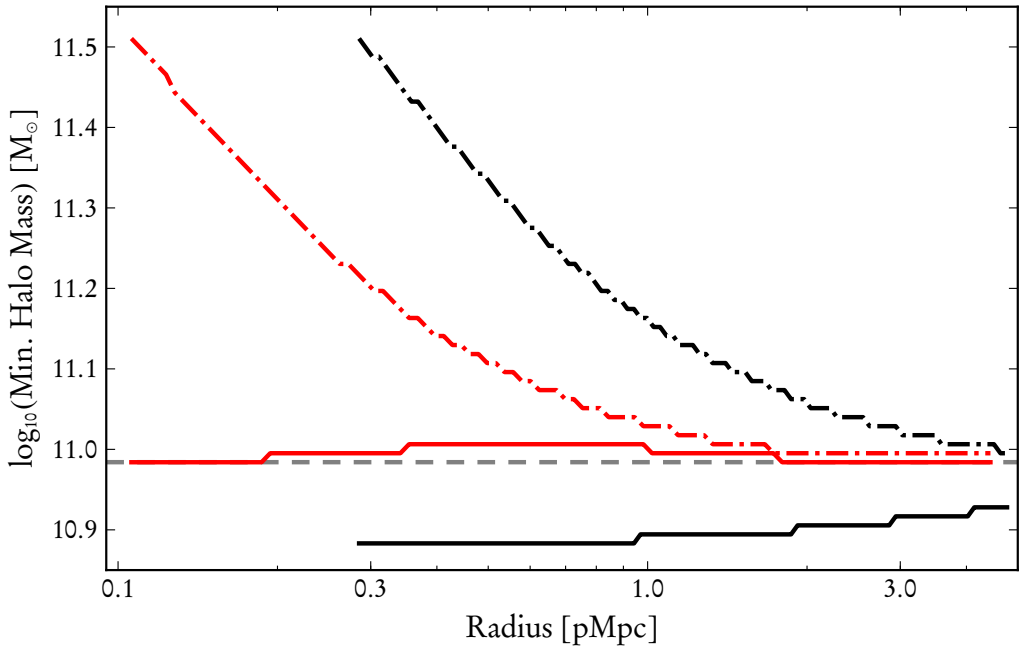

Figure 3.4: Faintest observable galaxy halo mass as a function of distance from a central quasar for quasar host halo masses of $2 \times 10^{13}\,M_\odot$ (**black** curves) and $10^{12}\,M_\odot$ (**red** curves). The solid curves include the density and UV flux from the nearby quasar and the dash-dotted curves include the increased density but with no UV boost from the quasar.

To do this in a way that accounts for the large, low-probability masses we randomly sample a Poisson distribution with a mean equal to $\mathcal{N}_{\mathrm{gal}\,ij}$. The resulting halo counts for each mass bin are distributed randomly upon the surface of the radial shell. This process is repeated for all radial shells, placing the galaxies for the model within the dark matter scaffolding unique to that realisation of the model.

Calculating the incident ionisation rate on every galaxy by every other galaxy in the model was computationally prohibitive given the resources available. To simplify this calculation, each shell in the model was divided into solid angles with roughly the same surface area, hereafter referred to as sectors. For each galaxy in the scaffolding, the neighbouring galaxies within a smoothing radius (on the order of 1 pMpc) were treated individually, each contributing to the incident ionising radiation. For galaxies within sectors outside this smoothing radius, the aggregate ionising lumin-

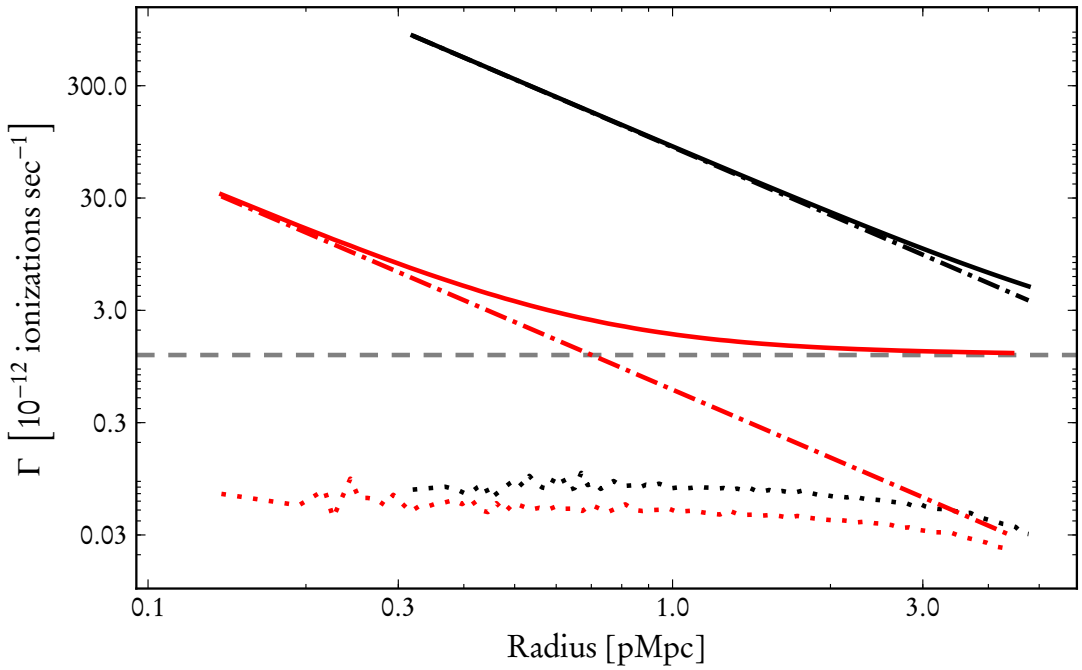

Figure 3.5: Average numerical ionisation rates as a function of distance from a central quasar with a halo size of $2 \times 10^{13}\,M_\odot$ (**black**) and $10^{12}\,M_\odot$ (**red**) for 100 model realisations at $z = 2.2$. The dashed grey line is the calculated ionising background rate, Γ_{BG}. The dotted lines are the radially averaged galaxy-galaxy incident ionisation rate $\Gamma_{gal-gal}$, the dash-dotted lines are the central quasar incident ionisation rate Γ_Q, and the solid lines are the total averaged incident ionisation rates Γ_{all}

osity produced by the galaxies contained in each of these sectors was assigned to its centroid, and a single contribution representing the total flux from the sector was made to the incident radiation calculation. The total from the nearby individual galaxies and the distant sectors were combined yielding a unique $\Gamma_{gal-gal}$, and thereby a unique $L_{Ly\alpha} \times \mathcal{T}_{IGM}$, for each galaxy in the scaffolding.

Figure 3.5 shows the average breakdown of Γ_{all} as a function of distance from a central quasar with a halo size of $2 \times 10^{13}\,M_\odot$ (black) and $10^{12}\,M_\odot$ (red) for 100 model realisations at $z = 2.2$. For the larger quasar, Γ_Q dominates the ionisation rate over the entire range, with $\Gamma_{gal-gal}$ making up $\sim 0.6\,\%$ of the total. For the smaller quasar, Γ_Q dominates at closer separations but dips below Γ_{BG} at larger separations.

This weaker $\Gamma_{\rm Q}$ causes $\Gamma_{\rm gal-gal}$ to form $\sim 3\,\%$ of the total. The erratic values of $\Gamma_{\rm gal-gal}$ at small separations is a numerical artefact from the small sample size of realisations and the roll-over at large separations is due to the sharp drop off in neighbouring galaxies at the edge of the simulation.

The small contribution of $\Gamma_{\rm gal-gal}$ justifies the usage of the much more easily calculated analytic model assumed in the rest of this chapter.

3.3 Modelling survey volumes

With a fully developed model for estimating the transmitted $L_{\rm Ly\alpha}$ we are in a position to apply this model to Lyα survey volumes. The process is straightforward: determine the dimensions of the observed volume to model based on the survey parameters, accounting for any redshift-space distortions; create and run the model with the largest radial shell that encloses the entire survey volume; clip the spherical model to match the non-spherical survey volume; count the number of galaxies in the model that have a transmitted Lyα luminosity above the detection limit of the survey; and, finally, compare this to the number of galaxies observed in the volume.

The motivation for much of the work in this thesis is from the Lyα survey conducted around quasar PKS 0424-131 in FBH04. We will describe in detail how we applied the steps outlined above to this observation and summarise the results of applying the same procedure to other existing Lyα surveys.

3.3.1 Determining initial model dimensions

The procedure used to calculate the physical bounding box on a Lyα galaxy survey is straightforward. From the design of the survey we are given the solid angle rectangle making up the survey, usually in units of arcminutes or arcseconds. From the target redshift of the survey (in our case the redshift of the central quasar) we can calculate

the angular diameter distance[3], giving a conversion factor from this angular separation to cMpc. This allows us to calculate the 'height' and 'width' of the survey; we will refer to the calculated real-space lengths of these dimension as V_x and V_y.

Determining the 'depth' of the survey, V_z, requires an understanding of the instrumentation and methodology employed during the observations. As will be discussed in chapter 4, narrowband Lyα galaxy surveys are conducted over a well-defined and narrow wavelength range. From this range and an understanding of the type of narrowband filter used for the observations, minimum and maximum detectable wavelengths can be deduced, with each corresponding to $\lambda_{\mathrm{Ly}\alpha}$ at a different redshift. These redshifts are then turned into comoving distances using the assumed cosmology, and their difference gives the final dimension V_z in cMpc.

The scaffolding defined in section 3.1 is built using units of pMpc and so we convert V_x, V_y, and V_z from cMpc to pMpc by dividing through by $1 + z$. With the dimensions from the survey in proper physical units we can finally calculate the appropriate r_{max} for the spherical shells defined in the model. We assume the central quasar will be in the exact centre of the survey volume, so all vertices in the three-dimensional bounding box of the survey will be the same distance from the centre. Thus, to ensure that the largest radial shell encloses the entire bounding box, r_{max} should be equal to the distance from the centre of the volume to a vertex:

$$r_{\mathrm{max}} = \sqrt{\frac{V_x^2}{2} + \frac{V_y^2}{2} + \frac{V_z^2}{2}}. \tag{3.15}$$

As we will show in the next section, this initial calculation of r_{max} needs to be modified to account for observational biases. To avoid confusion when we calculate corrections to these biases, we will denote this initial calculation of r_{max} as $r_{\mathrm{max,init}}$.

[3]Hogg (1999) gives a summary of all cosmological distances used in this section.

3.3.2 Accounting for redshift-space distortions

Calculating the distance to an observed Lyα galaxy is, by necessity, done first in redshift-space and later converted to real-space using an assumed cosmology. Converting from the observed redshift-space to the physical real-space would be straightforward if not for the Doppler shifts on observed spectral features introduced by line-of-sight motion relative to the Hubble flow. These non-Hubble peculiar velocities blueshift or redshift the observed photons and move the spectral features from their expected locations, leading to inaccurate distance measures when converting to real-space. These effects are collectively known as redshift-space distortions and two major flavours are present in galaxy surveys: the elongation of redshift-space galaxy distributions along the line-of-sight of an observer on small scales, dubbed the 'Finger of God' effect; and a flattening of galaxy distributions at larger scales, called the Kaiser effect (Kaiser, 1987).

The Finger of God effect is caused by galaxies close to centre of galaxy clusters. Due to the random initial velocities of the galaxies and the intense gravity in the heart of a galaxy cluster, the velocity vectors for these galaxies can vary widely. At lower redshifts the line-of-sight component of these velocities can become a non-trivial fraction of the Hubble flow, and in turn wildly shift the apparent distance to the galaxy. At higher redshifts these random velocities cause a smaller fractional deviation from the increased Hubble velocity and become less noticeable. Due to the stochastic nature of this effect, which is difficult to model without a proper treatment of galaxy kinematics, and its diminished strength at the redshifts we probe in this work, we will ignore it.

The Kaiser effect is also caused by peculiar velocities, but rather than random velocities close to the centre of the cluster it is caused by the gravitational infall of all galaxies towards the centre of a forming galaxy cluster. The attraction is towards

the centre of the cluster across all galaxies, causing a systematic blueshifting of the spectral features from galaxies on the far side of the cluster and a redshifting of galaxies on the near side. The aggregate effect is a perceived flattening of the galaxies in redshift-space. The coherent nature of this effect is noticeable over a larger distance than the stochastic mechanism behind the Finger of God effect, and is easily accounted for given the structure of our model.

Velocity induced real-space displacement

To account for the distortion caused by the Kaiser effect we first calculate the infall velocity at the largest radius in our model as defined in section 3.3.1, $r_{\mathrm{max,init}}$. From Peebles (1980) we can write the peculiar velocity vector described by linear theory, $\vec{v}_{\mathrm{pec}}$, as

$$\vec{v}_{\mathrm{pec}} = \frac{2}{3}\frac{(1+z)^2}{H(z)\Omega_{\mathrm{m}}}\frac{d\log\delta}{d\log a}(z)\vec{g}, \tag{3.16}$$

where $H(z)$ is the Hubble constant at redshift z, $\frac{d\log\delta}{d\log a}(z)$ is the logarithmic growth rate evaluated at redshift z (Lahav et al., 1991), and $\vec{g}$ is the peculiar acceleration vector.

For simplicity we assume that each radial shell in our model has a constant mass density, and thus at the $r_{\mathrm{max,init}}$ radial shell $\vec{g}$ becomes

$$\vec{g} = -\frac{GM_{\mathrm{enc}}}{r^2_{\mathrm{max,init}}}\vec{r}, \tag{3.17}$$

where G is the gravitational constant, M_{enc} is the mass enclosed by the $r_{\mathrm{max,init}}$ radial shell, and $\vec{r}$ is the radial unit vector.

To get the component of $\vec{g}$ along the line-of-sight we take the inner product of $\vec{g}$ with the line-of-sight unit vector $\vec{n}$, assumed to be at some angle α to $\vec{r}$, yielding $\cos\alpha|\vec{g}|$. Combining this with equations (3.16) and (3.17) yields a value for the

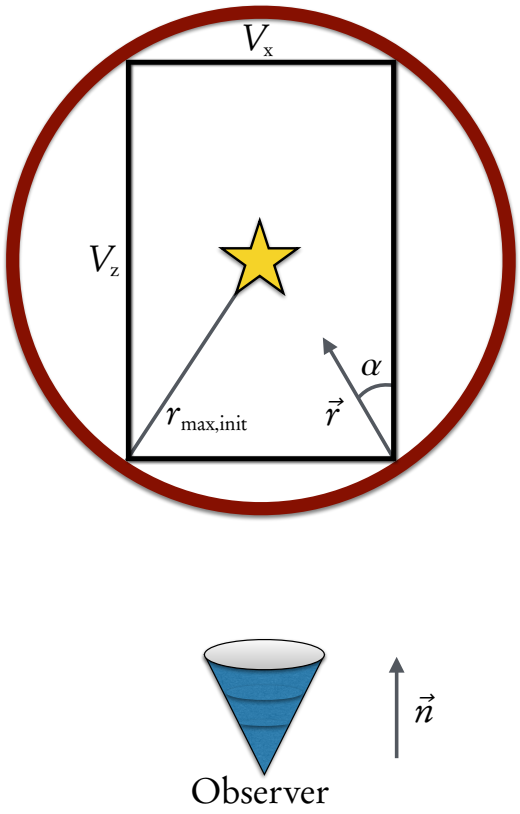

Figure 3.6: Geometry of survey bounding box and model radius from above, showing the line-of-sight and radial unit vectors $\vec{n}$ and $\vec{r}$.

magnitude of the line-of-sight peculiar velocity vector:

$$|\vec{v}_{pec}|_{los} = -\frac{2}{3}\frac{(1+z)^2}{H(z)\Omega_m}\frac{d\log\delta}{d\log a}(z)\frac{GM_{enc}}{r^2_{max,init}}\cos\alpha. \tag{3.18}$$

For our purposes these calculations will always assume that α is the angle to the point where the $r_{max,init}$ shell just touches the most distant vertex from the centre of the model along the line-of-sight. The geometry of this is shown from above in figure 3.6.

Finally we calculate the real-space line-of-sight displacement of the radial bin at

$r_{\mathrm{max,init}}$ at the V_z vertex, $x_{\mathrm{los-dis}}$, in units of pMpc, by dividing equation (3.18) through by $H(z)$ and a factor of $1+z$:

$$x_{\mathrm{los-dis}} = -\frac{2}{3}\frac{1+z}{H(z)^2\Omega_m}\frac{d\log\delta}{d\log a}(z)\frac{GM_{\mathrm{enc}}}{r^2_{\mathrm{max,init}}}\cos\alpha. \tag{3.19}$$

Because of this displacement, galaxies that are outside of the naïve survey bounding box defined by the dimensions V_x, V_y, and V_z will appear to be inside the survey after converting from redshift-space to real-space. We must compensate for this by increasing $r_{\mathrm{max,init}}$ so that it now includes these additional galaxies.

Accounting for the Kaiser effect

To successfully account for the Kaiser effect, we must choose a value of r_{max} large enough to encompass those galaxies shifted into the originally calculated $r_{\mathrm{max,init}}$ shell. We begin by calculating the initial displacement given in equation (3.19) and using it to extend the length V_z, accounting for the equal displacement both away from, and towards, the observer:

$$\begin{aligned} V_z' &= V_z + 2x_{\mathrm{los-dis}}, \\ \alpha' &= \arctan\left(\sqrt{\frac{V_x^2}{2}+\frac{V_y^2}{2}}\Big/\frac{V_z'}{2}\right), \\ r'_{\mathrm{max}} &= \sqrt{\frac{V_x^2}{2}+\frac{V_y^2}{2}+\frac{V_z'^2}{2}}, \end{aligned} \tag{3.20}$$

where V_z' is the effective depth of the bounding box in the model along the line-of-sight, α' is the angle to the new most distant vertex from the centre of the model along the line-of-sight, and r'_{max} is the effective r_{max} for the model using V_z'. This updated geometry can be seen in figure 3.7.

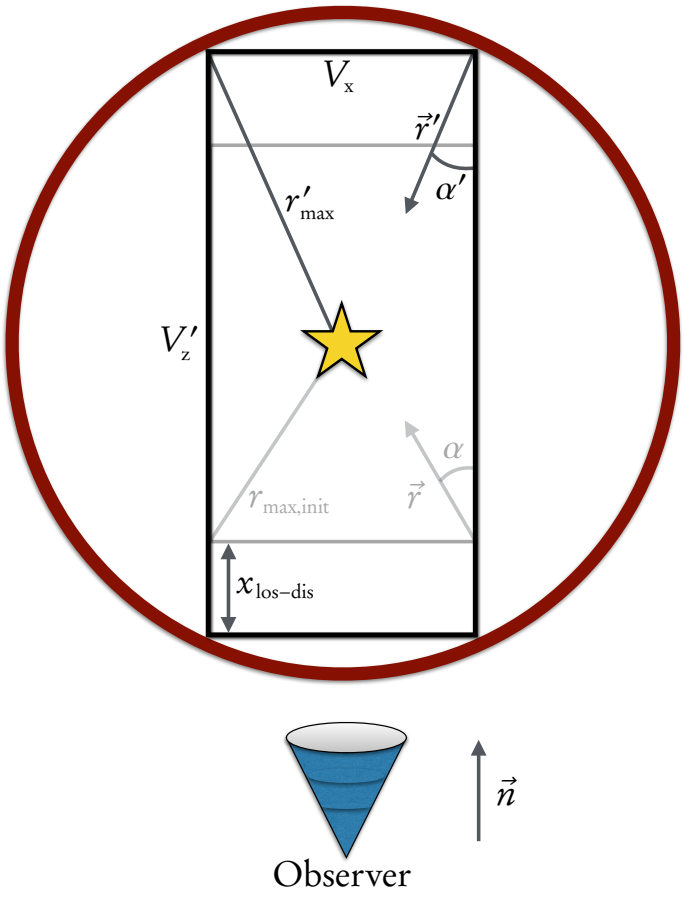

Figure 3.7: Geometry of survey and model from above, showing the calculated Kaiser effect displacement and the calculated r'_{max} and α'.

This process of extending r_{max} introduces a complication: a larger mass is enclosed by this larger radius, leading to a larger displacement. Thus r'_{max} is an underestimate of the required model radius. To get around this we are required to iterate this process of extending V_z, feeding r'_{max} and α' into equation (3.19) to get V_z'' and so on. This converges quickly, and when applied to the surveys analysed changed by less than one part in a thousand within three or four iterations.

3.3.3 *Lyα survey of PKS 0424-131*

FBH04 surveyed a field of view measuring 4.2 pMpc by 2.0 pMpc over a redshift

range of $\Delta z = 0.015$ centred on the $z = 2.168$ luminous quasar PKS 0424-131. This range corresponds to a physical depth of 6.5 pMpc at this redshift and an effective depth of 8.5 pMpc when accounting for redshift-space distortions. This yields an effective survey volume of 70 pMpc^3.

Their detection limit for Lyα emitting galaxies within this volume was 9.6×10^{-18} erg cm^{-2} s^{-1}, corresponding to an ideal ($\mathcal{T}_{\rm IGM} = 1$) minimum mass between 3.8×10^{10} M$_\odot$ ($\epsilon_{\rm DC} = 0.4$) and 7.1×10^{10} M$_\odot$ ($\epsilon_{\rm DC} = 1.0$). In our simulation we consider galaxies with host haloes ranging from this minimum detectable mass to a maximum of 10^{15} M$_\odot$, and use 500 mass bins distributed equally in log-space to span this range. Using the inferred mass of 2×10^{13} M$_\odot$ for PKS 0424-131, as calculated using the methods described in section 2.4, we calculated a virial radius of 280 pkpc which we used for the innermost spherical shell. The outermost shell was given a radius 4.84 pMpc, fully enclosing the rectangular observed volume. We used 100 radial shells to span this range of radii, distributed equally in log-space. For each radial bin that had a radius larger than 1.0 pMpc (i.e. the distance from the centre of modelled volume to the smallest dimension of the survey) we contribute only what fraction of the shell falls within the survey volume.

Figure 3.8 shows the results for this process over the allowed range of $\epsilon_{\rm DC}$ outlined in table 2.1. The solid black curve shows the average number of galaxies that should be visible within the volume surveyed by FBH04 as calculated by our model to be between 70 and 97. Even if the ionising flux from the quasar itself is omitted, as seen in the dash-dotted black curve, the average number of visible galaxies is still between 49 and 67. This can be contrasted with the grey dashed line which gives the expected number of galaxies assuming a mean density and IGM with no quasar, which ranges between 21 and 26. The clustering of galaxies around the quasar, combined with the higher than background transmission rates seen in figure 3.3, pushes the expected

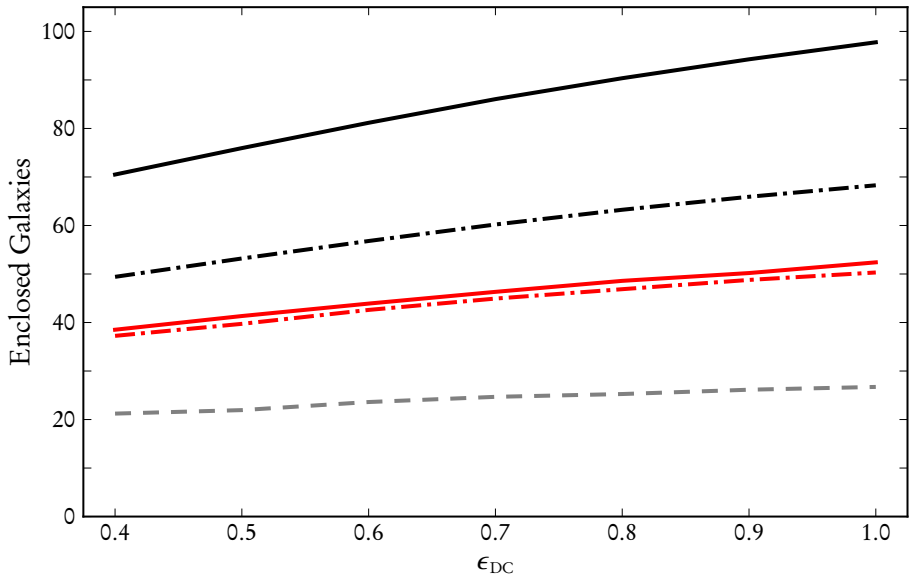

Figure 3.8: Predicted number of galaxies contained within the PKS 0424-131 survey volume as a function of modelled duty cycle, with host halo sizes $2 \times 10^{13}\,M_\odot$ (**black** curves) and $10^{12}\,M_\odot$ (**red** curves). The grey dashed curve corresponds to expected galaxy counts in the field and the solid (dash-dotted) curves include clustering and transmission effects including (excluding) the boosted UV flux from the quasar environments.

number of galaxies up well above background levels, in contrast with observation. These ranges also show that the while the value of ϵ_{DC} does influence the predicted number of visible galaxies appreciably in all circumstances, it does not change the value enough to account for a null detection.

We have also repeated the above calculation for the same observable volume and redshift but for a much less luminous central quasar. The mass of the dark matter halo hosting the quasar was set to $10^{12}\,M_\odot$ and the innermost radius of the spherical shell to the lower virial radius of this quasar, 100 pkpc, keeping the rest of the conditions the same. In this case the lower IGM density and lower UV flux conspire to give close to the same number of galaxies for conditions when the quasar UV flux is considered as when it is neglected. The solid and dash-dotted red lines show the expected galaxy count in these cases, which varies between 34 and 49 over the

allowed range in ϵ_{DC}.

Figure 3.9 shows the overdensity in each spherical shell of observable Lyα emitters in the modelled quasar environments compared to that of the modelled field for the $\epsilon_{DC} = 1$ case. This overdensity is a product of the linear bias of dark matter halo clustering around the host halo of the quasar, and the effects of Lyα transmission on observed luminosity. As before the black (red) curves indicate the model with a quasar host halo mass $2 \times 10^{13}\,M_\odot$ ($10 \times 10^{12}\,M_\odot$) and the solid (dash-dotted) curves include the boosted IGM density and UV flux (just IGM density) from the nearby quasar. The solid UV+density curves are shaped as one would expect from combining the monotonically decreasing shape of the clustering bias to the shape of the solid transmission curves in figure 3.3. Of more interest is the bump in radial overdensity of the dash-dotted density only curves, resulting from a monotonically decreasing clustering bias and the monotonically increasing $\mathcal{T}_{IGM}$ as the volume approaches background densities at large radius. This suggests that in a highly beamed ionising geometry (i.e. $f_{dil} \sim 0$) there should be a prominent overdensity feature even in the absence of galaxy suppression, peaking at ~ 1 pMpc from the central quasar in the case of PKS 0424-131.

Thus our model predicts a number of galaxies that is far in excess of the null-detection in FBH04. This galaxy excess could be due to an additional suppression of the Lyα signal that has not been modelled, PKS 0424-131 being in an unexpected environment without neighbouring star forming galaxies, or to some mechanism for the suppression of star formation in its neighbouring galaxies.

The mean number of galaxies required for the FBH04 null detection around PKS 0424-131 to be consistent with our model at the 68 % level is ~ 2.3, and at the 90 % level is ~ 1.1. Thus, for $\epsilon_{DC} = 1.0$ ($\epsilon_{DC} = 0.4$) our model must exclude masses below $2.5 \times 10^{12}\,M_\odot$ ($1.2 \times 10^{12}\,M_\odot$) in order to bring the mean number of galaxies

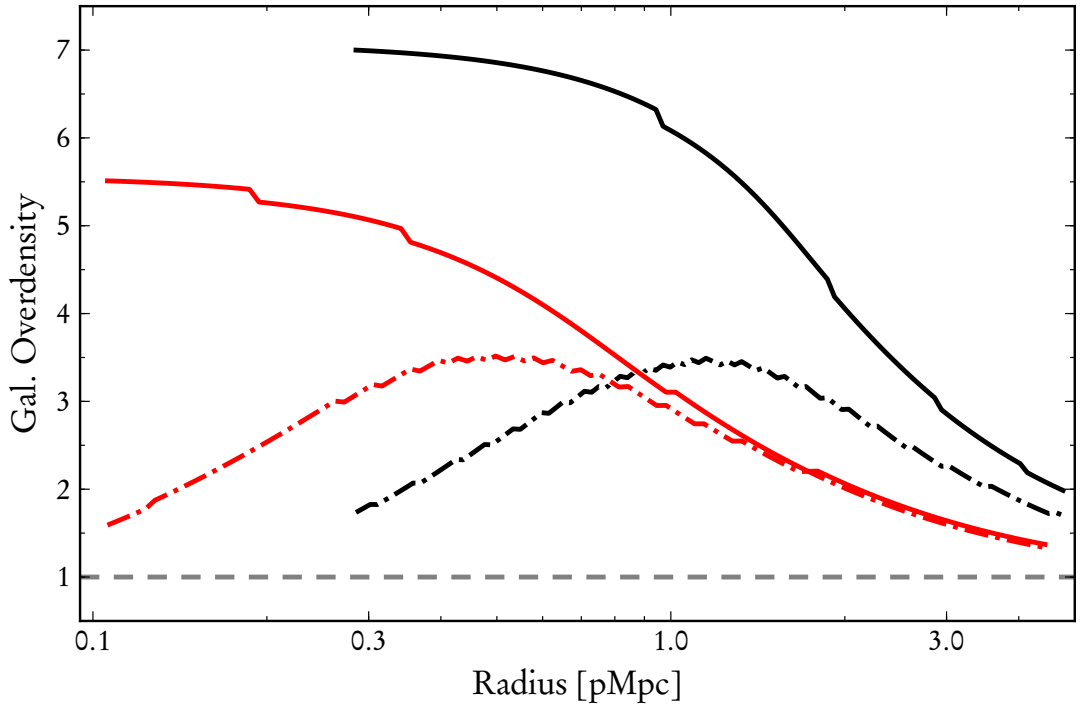

Figure 3.9: Predicted galaxy overdensity around PKS 0424-131 as a function of distance from the central quasar, assuming both a host halo size $2 \times 10^{13}\,M_\odot$ (**black** curves) and $10^{12}\,M_\odot$ (**red** curves). The grey dashed curve corresponds to expected galaxy overdensity in the field and the solid (dash-dotted) curves include clustering and transmission effects including (excluding) the boosted UV flux from the quasar environments.

down to a value consistent with observations at the 68 % level, and must exclude masses below $4.2 \times 10^{12}\,M_\odot$ ($2.1 \times 10^{12}\,M_\odot$ to be consistent at the 90 % level. This means that the most conservative virial temperature consistent with observation is $T_{\rm vir} \gtrsim 3.4 \times 10^6$ K, equivalent to $\sim 1.2 \times 10^{12}\,M_\odot$. This result may imply considerable suppression of galaxy formation by the nearby quasar.

Following Kashikawa et al. (2007) we describe a possible scenario for the null detection of LAEs around PKS 0424-131. A galaxy may first appear as a LAE during its initial starburst period (Shapley et al., 2001). These young galaxies can be hosted in haloes with virial temperatures as low as $\sim 3 \times 10^5$ K, with an initial active LAE phase lasting $\sim 10^6$ to $\sim 10^8$ years (Gawiser et al., 2006; Overzier et al., 2008; Pirzkal et al.,

2007), roughly the same timescale the active luminous accretion phase of a quasar (Shen et al., 2007). The enhanced UV radiation from the quasar could, under these conditions, delay nearby protogalaxies from beginning their star formation during the observed epoch and leading to a dearth of LAEs detected in the vicinity of PKS 0424-131. Larger haloes that had already collapsed and undergone star formation at the time PKS 0424-131 became active would not have been affected by the UV field of the quasar, but because they had grown out of their active LAE phase would also not be detected close to the quasar by Lyα specific narrow-band observation.

3.3.4 Additional Lyα surveys

Multiple studies have investigated the population of Lyα emitting galaxies near luminous quasars. Cantalupo et al. (2007) reported a detection of 13 Lyα sources clustered around a quasar at $z = 3.1$ in a $\sim 25\,\mathrm{pMpc}^3$ volume (sparsely sampled from a larger $\sim 200\,\mathrm{pMpc}^3$ volume), two of which they suggested were hydrogen clouds fluoresced by the ionising radiation of the quasar. Our model, accounting for the sparse sampling, predicts approximately 20 galaxies should be detected in this volume. The possible externally fluoresced sources suggest there is enough ionising flux around these high-redshift luminous quasars to strongly impact neighbouring H I.

Kashikawa et al. (2007) conducted a deep wide field narrow-band survey for Lyman break galaxies and LAEs around QSO SDSS J0211-0009 at $z = 4.9$. They surveyed $\sim 830\,\mathrm{pMpc}^3$ in the vicinity of the quasar and detected 221 LAEs. Our simulation predicted ~ 260 detectable LAEs for a similar volume, quasar, and redshift. Kashikawa et al. (2007) also found that the observed Lyman break galaxies formed a distributed filamentary structure which included the quasar, but that the LAEs were preferentially clustered around the quasar and avoided a vicinity of 4.5 cMpc

from the quasar. This region was calculated to have a UV radiation field roughly 100 times that of the background, and this was posited to be suppressing the formation of LAEs. This spatial distribution of LAEs reinforces the idea that the environment in the smaller volumes probed by our model – in the direct vicinity of the quasar – is where the majority of galaxy suppression takes place.

Venemans et al. (2007) made observations of clustered Lyα emitter overdensities around radio galaxies and found that these overdensities ranged from $1.2^{+0.8}_{-0.7}$ to $4.8^{+1.1}_{-0.8}$ in 9 fields at $z > 2$. We find that the integrated overdensity of observable Lyα emitters is a factor 3.7 (2.0) larger in the modelled quasar environment compared to that of the modelled field, assuming a quasar host halo of $2 \times 10^{13}\,M_\odot$ ($10^{12}\,M_\odot$) and an isotropically emitted UV field from the quasar. Assuming no quasar contribution to the UV we find an integrated overdensity of 2.6 (1.9). In both cases our model compares favourably with observation. We note that this is a cursory comparison; some radio galaxies are differentiated from quasars only by orientation while others may have different radiative mechanisms that are not modelled in this thesis.

Of more direct relevance, Swinbank et al. (2012) conducted a deeper LAE search around three high-shift quasars using the same instrumentation as FBH04. In each of the fields they searched observed they were able to detect candidate LAEs, including 17 around a $z \sim 4.5$ quasar, which they found to be a significant overdensity compared to the expected background density. The results from Swinbank et al. (2012) were published during the preparation of this thesis, and as such we were not able to model their fields directly with our simulations. Their results do suggest a qualitative agreement with the general results from our simulations.

3.4 Summary

In this chapter we have created a framework for modelling a quasar-dominated galaxy cluster, calculating the individual transmitted $L_{\mathrm{Ly}\alpha}$ of each galaxy according to the methodology outlined in chapter 2. This framework relies heavily on dark matter correlation functions, and assumptions about the size evolution and collapse of over-densities in the pristine dark matter density field. The main result of this chapter are the results from the detailed modelling of the environs around the quasar PKS 0424-131. The discrepancy between the observable galaxy count predicted by the model and the null detection in the observations by FBH04 is the motivation behind the observations that will be described in chapters 4 and 5.

Chapter 4

Tunable filter Lyα observations

The modelling presented in chapters 2 and 3 gives us the tools to estimate Lyα observability in quasar-dominated galaxy clusters. In this chapter we describe observations conducted specifically to test the accuracy of these models. We outline the design and usage of tunable narrowband filters, and their unique suitability for Lyα observations. We lay out the design and execution of an observing run conducted in April, 2012, using the Maryland-Magellan Tunable Filter (MMTF) to look for Lyα galaxies in the clustered environment around a quasar. Finally, we discuss the flux limits achieved for these observations and the corresponding number of detectable Lyα galaxies modelling predicts for these limits.

4.1 Tunable narrowband filters

A bandpass of ~100 Å – a representative size for most narrowband filters used to detect LAEs – translates into a line-of-sight distance of ~17 pMpc at $z = 3.3$. This is far larger than the volume of the quasar environments we are modelling, which allows for Lyα emitting galaxies in the field to contaminate any observational results. To probe just the region of interest around a quasar the bandpass must be small enough to give the required line-of-sight distance resolution while, at the same time, allowing for robust target selection. For this we turn to the Fabry-Pérot interferometer, an instrument which has the ability to create a narrowband filter with an order of magnitude smaller bandpass than traditional narrowband filters, and that can also

adjust its central wavelength electronically in real-time.

A Fabry-Pérot etalon is comprised of two parallel plates of glass separated by an air-gap measured in microns (see Jacquinot, 1960). The interior glass surfaces are covered with a highly reflective coating, and the light transmitted through the plates and air-gap of the etalon is limited to repeated Lorentzian shaped orders, as illustrated in figure 4.1. These orders have a central wavelength that is an integer multiple of an underlying fundamental wavelength. A broadband blocking filter with a bandpass narrower than the fundamental wavelength is placed in line with the etalon, and allows only a single order through to the camera. The resulting instrument is capable of acting as a wide-area, low-resolution spectrograph with a high efficiency advantage over conventional long-slit spectrographs. Each of these orders has a full-width at half maximum (FWHM) bandpass of ~10 Å, translating into a line-of-sight distance of ~2 pMpc at $z = 3.3$. This allows one of these orders to just enclose the central region of the quasar volumes modelled in chapter 3.

The fundamental wavelength is parametrised by the width of the air-gap. By precisely changing this width, one is able to tune the filter to the wavelength of interest. Until recently it had proven too challenging to maintain the parallelisation of the etalon and air-gap width as the telescope tracked objects throughout the night. Queensgate Instruments Pty Ltd finally solved this problem with precise servo-controlled etalons in the 1980s, and by the 1990s the first generation of astronomical instruments using Queensgate etalons were commissioned for 4 m class telescopes (Gebhardt et al., 1994). Among these was the Taurus Tunable Filter (TTF) (Bland-Hawthorn & Jones, 1998), installed on the 3.9 m Anglo-Australian Telescope in 1998. Now decommissioned, the TTF instrument was used by Francis & Bland-Hawthorn (2004) to search for Lyα emission in the observations that served as the inspiration for the modelling done in this thesis.

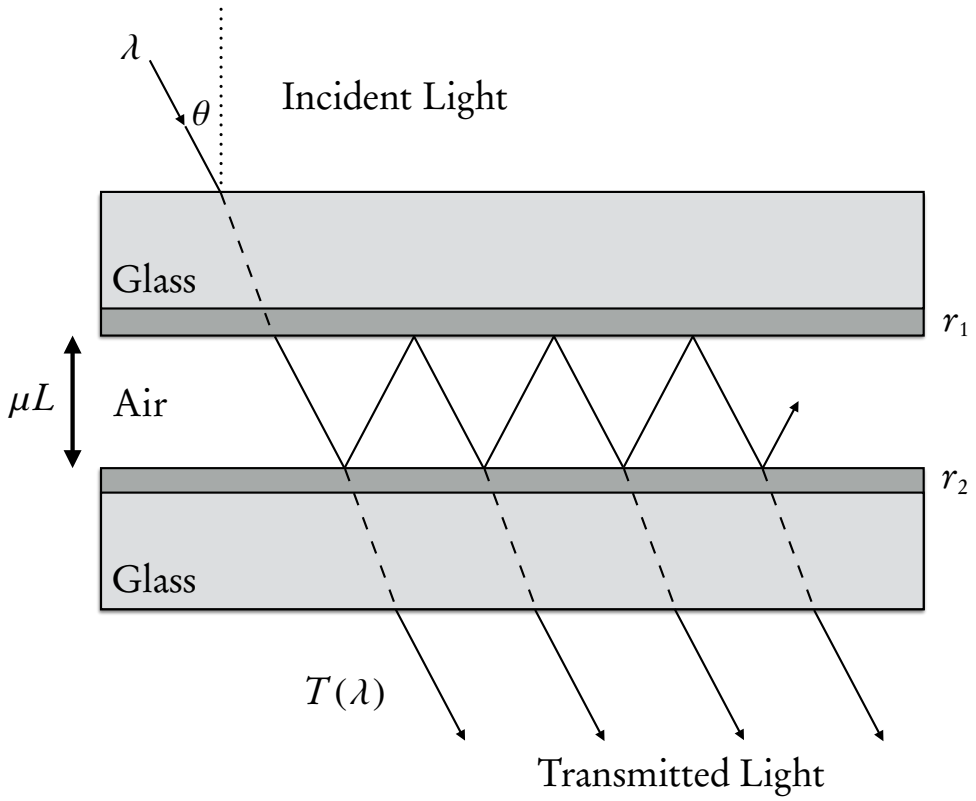

Figure 4.1: Diagram of a Fabry-Pérot etalon. Adapted from Jones (1999).

The TTF made use of large piezoelectric stacks controlled with a capacitance bridge to maintain precise separation and parallelisation of the two plates within the etalon. The electronics that maintained the air-gap separation also made it straightforward to vary the fundamental wavelength quickly, without having to physically swap out a filter as in traditional observing. This allowed multiple narrowband images to be taken without much overhead, allowing for bandpasses spanning hundreds of Å to be taken of the desired field of view on the same night, without the need to identify targets and prepare costly slit masks ahead of time (see Jones & Bland-Hawthorn, 2001).

The Maryland-Magellan Tunable Filter (MMTF) was the first tunable Fabry-Pérot etalon filter to be installed on a 6 m-class telescope (Veilleux et al., 2010). It is

built on a 150 mm clear aperture etalon, and can scan the wavelength range ~5000 Å to ~9200 Å with a bandpass varying from ~5 Å to ~15 Å with increasing wavelength. The MMTF is located in the disperser wheel of the Inamori Magellan Areal Camera and Spectrograph (IMACS) instrument of the Magellan-Baade Telescope, as seen in figure 4.2, and is capable of providing a monochromatic[1] field of view of ~14 arcminutes in diameter (Dressler et al., 2006). This field of view is equivalent to ~6.3 pMpc at $z = 3.3$, giving a cylindrical volume along the line of sight with roughly equivalent depth and diameter. Thus the MMTF gives us the opportunity to map out Lyα emission around a particular high-redshift quasar of interest, with a resolution that captures just the volume in its immediate vicinity.

4.2 Experimental design

We were allocated two nights in the 2012A observing semester on the Magellan-Baade telescope to detect galaxies near UV luminous quasars at $z \sim 3.3$ with the MMTF. Our experimental design was to observe the volumes around luminous quasars and count the number of star forming Lyα galaxies in their immediate vicinity. The distribution and counts of these galaxies would then be used to establish bounds on the critical ionising flux at which local star formation is quenched by the ionising radiation of the central quasar, Φ_0. In order to detect representative gas-rich dwarf galaxies would require a limiting flux of $2.5 \times 10^{-17}\,\mathrm{erg\,cm^{-2}}$ (3σ) on the MMTF. This corresponds to an integration time of 1 h under normal seeing[2] conditions for the MMTF with a 2×2 binning of the CCD pixels.[3]

Given the number of nights allocated we planned to observe two luminous

[1] The 'monochromatic spot' is defined to be the central region of the field of view, where the change in wavelength is not more than $\sqrt{2}$ of the etalon bandpass.

[2] Shorthand for 'seeing disc diameter', seeing is the FWHM of the point spread function (PSF), measured in arcseconds, giving an indication of how blurry the resultant images will be.

[3] `http://www.astro.umd.edu/~veilleux/mmtf/expcalc1.php`

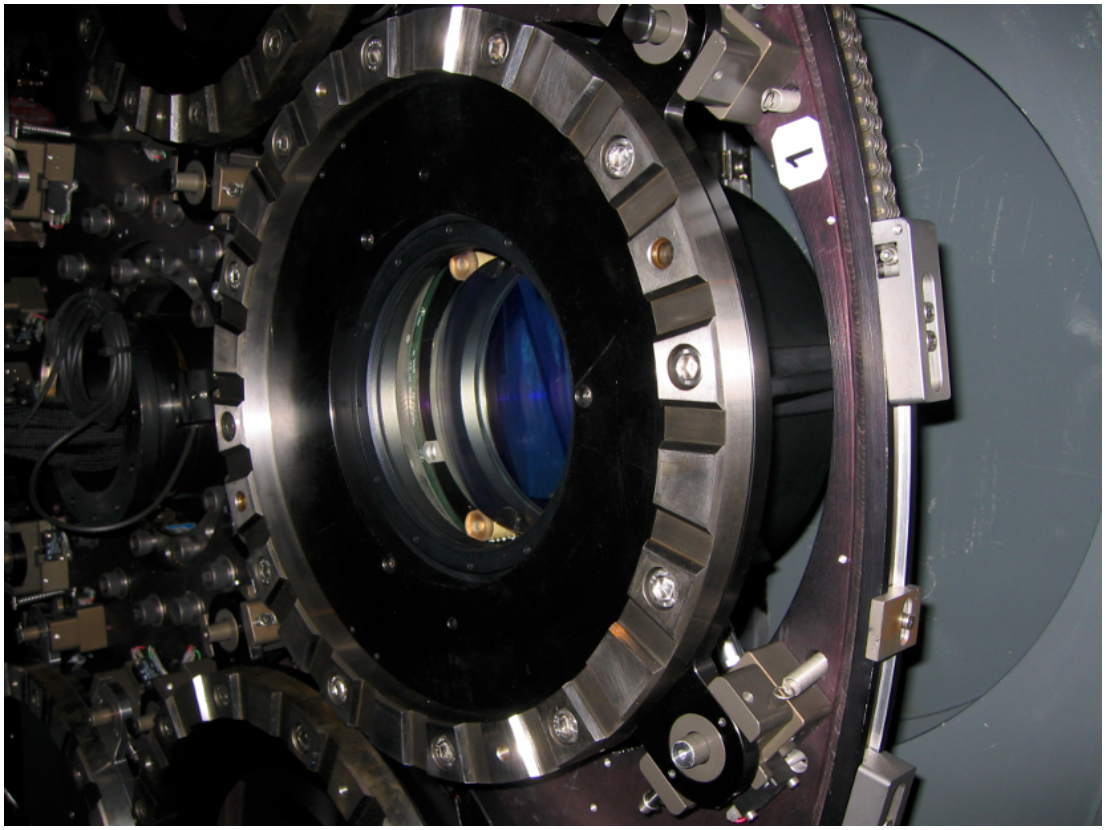

Figure 4.2: MMTF mounted in IMACS disperser wheel. From Veilleux et al. (2010).

quasars, each emitting more than $10^{47}\,\mathrm{erg\,s^{-1}}$, and one fainter quasar roughly one-hundred times less luminous as a control. Should any implied damping of star formation appear in the images of the two luminous quasars and not in those of the fainter control it would be evidence that the radiation field of the brighter quasars is suppressing star formation. Information about the environment of the galaxy cluster in each of the three quasar fields would also be extracted from the distribution of Lyα galaxies in each field to give insight as to whether any environmental bias may exist between the three survey volumes.

Five 1 h exposures would be taken, spaced by ~12 Å and contiguous in wavelength, with the central frame of the five corresponding to $\lambda_{\mathrm{Ly}\alpha}$ at the systemic redshift of the quasar. The Lyα galaxy candidates would then be those sources with larger re-

lative emission in just one of the five frames. A broadband image of the same area would be taken as well to help eliminate any obvious low-redshift objects. The modelling in chapter 3 suggested that we should be able to observe between ~30 and ~40 galaxies given the proposed integration time (see section 4.4.1 for the calculations), and by comparing the observed counts of Lyα galaxy candidates we would be able to determine if any evidence for photo-suppression was present. From this we would be able to calculate limits on the critical ionisation rate required for galaxy formation suppression.

4.2.1 Target selection for MMTF observing

The location of the observatory[4] limited the selection of quasars to those with the following characteristics: they must be visible in the Southern hemisphere, at a declination (dec) of less than 20°; they must be visible between the evening and morning twilight at Las Campanas Observatory on the allocated nights of the 11th and 12th of April, 2012, at a right ascension (RA) between 8°29′ and 18°22′; they must lie in a redshift range that falls within one order blocking filter of the MMTF to cut down on instrument overhead, at a redshift from 3.2 to 3.4; and, after these criteria have been met, they must represent both ends of the luminosity range so as to get the largest contrast between our experimental (super luminous) and control quasars.

563 quasars from the Veron Catalogue of Quasars & AGN, 13th Edition (Véron-Cetty & Véron, 2010) matched these specifications, and from this initial list two groups of candidates – 'bright' and 'faint' – were formed based on their V apparent magnitudes. The 'bright' group was made up of the 35 most luminous quasars, with apparent V-band magnitudes from 16.6 to 19 as seen in table 4.1; the 'faint' group was made of the 35 least luminous quasars, with apparent V-band magnitudes from

[4]Las Campanas Observatory: 29°0′52.56″ S, 70°41′33.36″ W, altitude 2380 m.

20.95 to 22.55 as seen in table 4.2.

These target lists were pared down to a final set of 5 'bright' and 5 'faint' targets, by selecting those with the smallest minimum airmass[5] on the night and whose time of minimum airmass allowed for maximum time on target. The plan to observe two objects a night necessitated the selection of objects whose time of minimum airmass roughly bisected the first and the last half of the night, referred to as 'early and 'late' respectively. Targets were given a shorthand label that encapsulated their experimental characteristics: time of visibility on the night, 'early' (*E*) and 'late' (*L*); their brightness, 'bright' (*B*) and 'faint' (*F*); and their two-digit priority within these categories based on their visibility throughout the evening. These final candidates and their observable properties are shown in table 4.3.

The first night would cover most of the filters for two objects, a 'bright' and a 'faint' object, as well as the required calibration images for later data reduction. The second night would finish any missing filter coverage of the two objects from the first night and would focus on a second 'bright' target, with any extra time being devoted to taking additional observations of opportunity on the three objects in the central narrowband wavelength range with the MMTF. The visible times for each target and the tracks these objects made through the sky on the observed nights is shown graphically in figure 4.3.

The final choice of targets was made on the night of the observations, after consultation with the telescope operator and instrument scientist, to ensure the best possible science outcome given their observability on the night. The three targets selected were EF02, LB01, and LB03. Figure 4.4 shows the tracks these objects made through the sky, along with the track of the Moon.

As will be discussed in section 5.2, only the observations of EF02 were completed

[5]Airmass is the relative optical path length for light through the atmosphere, defined to have a value of 1 at sea-level zenith.

Table 4.1: Most luminous 35 quasars from the Veron Catalogue of Quasars & AGN, 13th Edition, matching requirements of the April, 2012, observations ordered by apparent V-band magnitude.

Name	RA	dec	m_V	Redshift
TEX 1653+198	16°55′43.6″	19°48′47″	16.60	3.260
SDSS J09420+0422	9°42′2.0″	4°22′44″	17.47	3.276
CTQ 1061	10°48′56.7″	−16°37′10″	17.70	3.370
SDSS J12017+0116	12°1′44.4″	1°16′11″	17.74	3.233
Q 1410+0936	14°13′21.0″	9°22′5″	17.80	3.317
Q 0956+1217	9°58′52.2″	12°2′45″	17.91	3.306
Q 1052+04	10°55′5.2″	4°14′0″	18.10	3.391
SDSS J13071+1230	13°7′10.2″	12°30′21″	18.15	3.210
SDSS J10349+0358	10°34′56.3″	3°58′59″	18.25	3.369
SDSS J10251+0452	10°25′9.6″	4°52′46″	18.32	3.244
SDSS J11433+1934	11°43′23.7″	19°34′47″	18.36	3.357
SDSS J16553+1847	16°55′23.0″	18°47′8″	18.37	3.337
SDSS J13379+0218	13°37′57.9″	2°18′21″	18.48	3.333
SDSS J08402+1034	8°40′17.9″	10°34′29″	18.48	3.331
SDSS J09121+0547	9°12′10.4″	5°47′42″	18.51	3.241
SDSS J14279-0029	14°27′55.8″	−0°29′51″	18.57	3.365
SDSS J11169+0808	11°16′56.9″	8°8′29″	18.59	3.234
SDSS J15577+1540	15°57′43.3″	15°40′20″	18.59	3.287
SDSS J11439+1903	11°43′58.9″	19°3′27″	18.59	3.201
SDSS J08440+0503	8°44′1.9″	5°3′58″	18.67	3.346
SDSS J13337+1233	13°33′42.6″	12°33′53″	18.70	3.271
SDSS J10191+0254	10°19′8.3″	2°54′32″	18.74	3.390
SDSS J10137+1122	10°13′46.6″	11°22′31″	18.76	3.259
SDSS J11335+1447	11°33′30.2″	14°47′58″	18.76	3.244
SDSS J15158+1329	15°15′53.2″	13°29′26″	18.77	3.209
SDSS J11101+1804	11°10′7.3″	18°4′39″	18.83	3.270
SDSS J12532+1147	12°53′16.1″	11°47′20″	18.85	3.284
SDSS J15406+1054	15°40′42.0″	10°54′27″	18.86	3.278
SDSS J12239+1458	12°23′56.8″	14°58′23″	18.86	3.246
SDSS J09318-0000	9°31′53.1″	−0°0′52″	18.92	3.211
SDSS J15289+1504	15°28′56.3″	15°4′52″	18.94	3.389
SDSS J15026+0302	15°2′38.4″	3°2′28″	18.95	3.359
SDSS J11003+1629	11°0′21.0″	16°29′14″	18.97	3.381
SDSS J12027+1452	12°2′45.0″	14°52′29″	18.99	3.366
SDSS J09465+1251	9°46′32.8″	12°51′46″	19.00	3.300

Table 4.2: Least luminous 35 quasars from Veron Catalogue of Quasars & AGN, 13th Edition, matching requirements of the April, 2012, observations ordered by apparent V-band magnitude.

Name	RA	dec	m_V	Redshift
SDSS J15295+1921	15°29′31.5″	19°21′28″	20.95	3.217
SDSS J15021+0605	15°2′8.6″	6°5′12″	20.96	3.379
SDSS J10090+0956	10°9′1.3″	9°56′52″	20.96	3.332
SDSS J10079+1111	10°7′54.4″	11°11′7″	20.96	3.322
SDSS J15119+1453	15°11′59.3″	14°53′37″	20.96	3.258
SDSS J16579+1811	16°57′56.0″	18°11′56″	20.96	3.395
SDSS J12523+1048	12°52′21.0″	10°48′21″	20.97	3.338
SDSS J15580+1735	15°58′3.1″	17°35′19″	20.97	3.296
SDSS J09191+1014	9°19′6.2″	10°14′44″	20.98	3.259
SDSS J14302+1831	14°30′12.7″	18°31′46″	20.99	3.335
SDSS J13173+0809	13°17′23.2″	8°9′52″	21.00	3.392
SDSS J15263+1630	15°26′18.9″	16°30′54″	21.01	3.205
SDSS J12299+1942	12°29′57.0″	19°42′10″	21.01	3.363
SDSS J09256-0059	9°25′36.8″	−0°59′39″	21.03	3.385
SDSS J15421+0129	15°42′7.1″	1°29′18″	21.03	3.264
SDSS J11548+1427	11°54′49.7″	14°27′55″	21.03	3.372
SDSS J11038+0844	11°3′51.4″	8°44′34″	21.04	3.218
SDSS J09411+1423	9°41′8.0″	14°23′37″	21.05	3.295
SDSS J15151-0017	15°15′9.3″	−0°17′56″	21.07	3.267
SDSS J09535+0336	9°53′33.8″	3°36′24″	21.07	3.281
SDSS J09317+1557	9°31′45.5″	15°57′10″	21.07	3.296
SDSS J09147+0658	9°14′48.0″	6°58′28″	21.09	3.228
SDSS J13070+1759	13°7′4.5″	17°59′17″	21.09	3.346
SDSS J12379+1016	12°37′58.9″	10°16′54″	21.10	3.211
SDSS J14549-0027	14°54′55.4″	−0°27′59″	21.13	3.315
SDSS J10519+0018	10°51′54.8″	0°18′23″	21.17	3.305
SDSS J11412+0603	11°41′17.4″	6°3′32″	21.22	3.293
SDSS J16368+1250	16°36′49.0″	12°50′15″	21.24	3.302
SDSS J10067+0013	10°6′43.8″	0°13′48″	21.30	3.327
SDSS J15356+0607	15°35′36.0″	6°7′54″	21.52	3.341
SDSS J11236+1553	11°23′40.1″	15°53′54″	21.53	3.381
SDSS J09421+0219	9°42′7.8″	2°19′21″	21.79	3.211
SDSS J10126+1314	10°12′41.5″	13°14′10″	21.85	3.237
SDSS J14398+1333	14°39′52.1″	13°33′32″	21.92	3.270
QNQ J11192-1334	11°19′12.3″	−13°34′5″	22.55	3.252

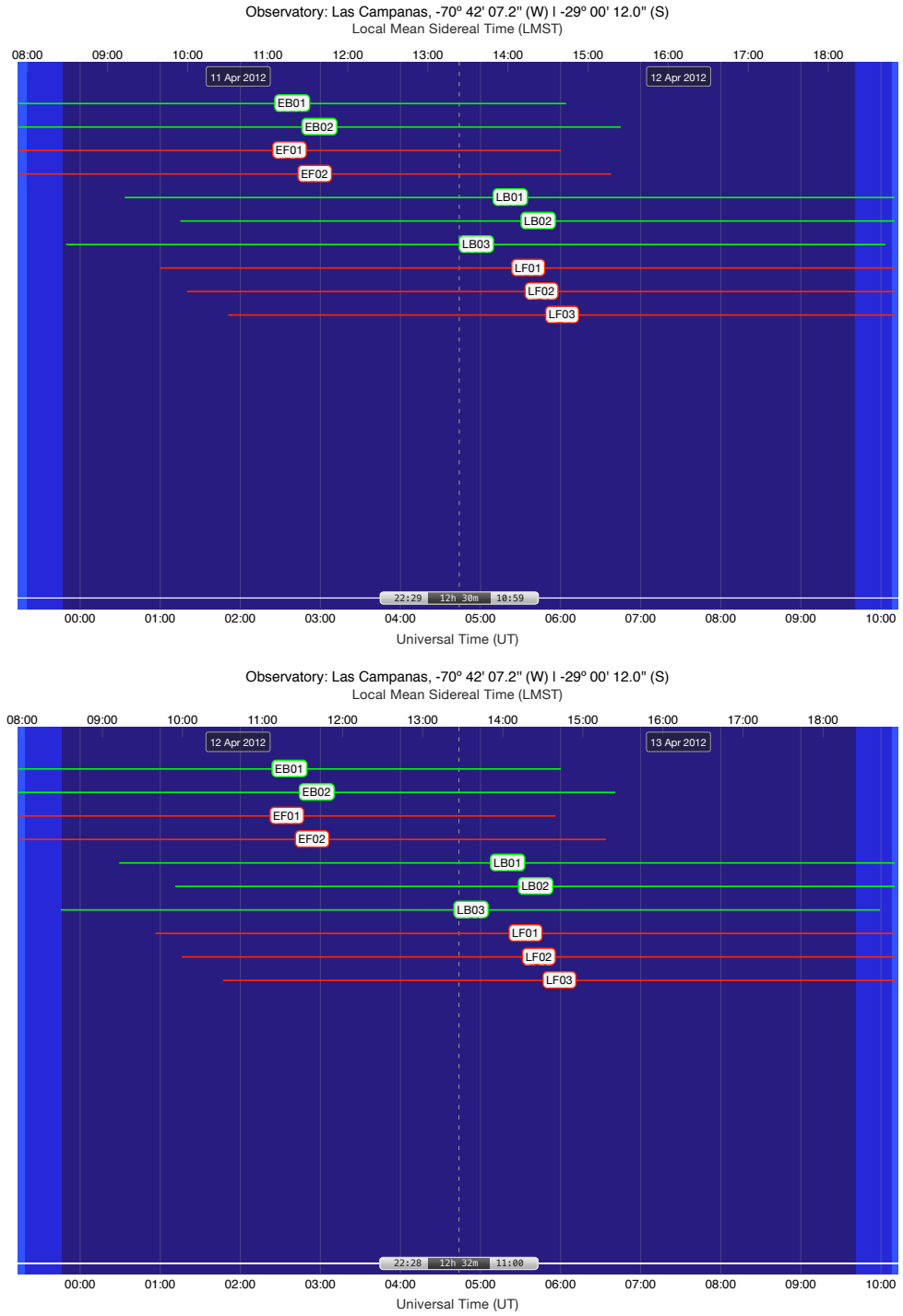

Figure 4.3: Shortlist target visibility for April 11th and 12th, 2012. The red (green) lines show the visible range of the 'faint' ('bright') targets, where a target is defined to be visible if it is at least 10° above the horizon and their airmass is below 5.76. Image prepared using iObserve: `http://www.onekilopars.ec/iobserve/`.

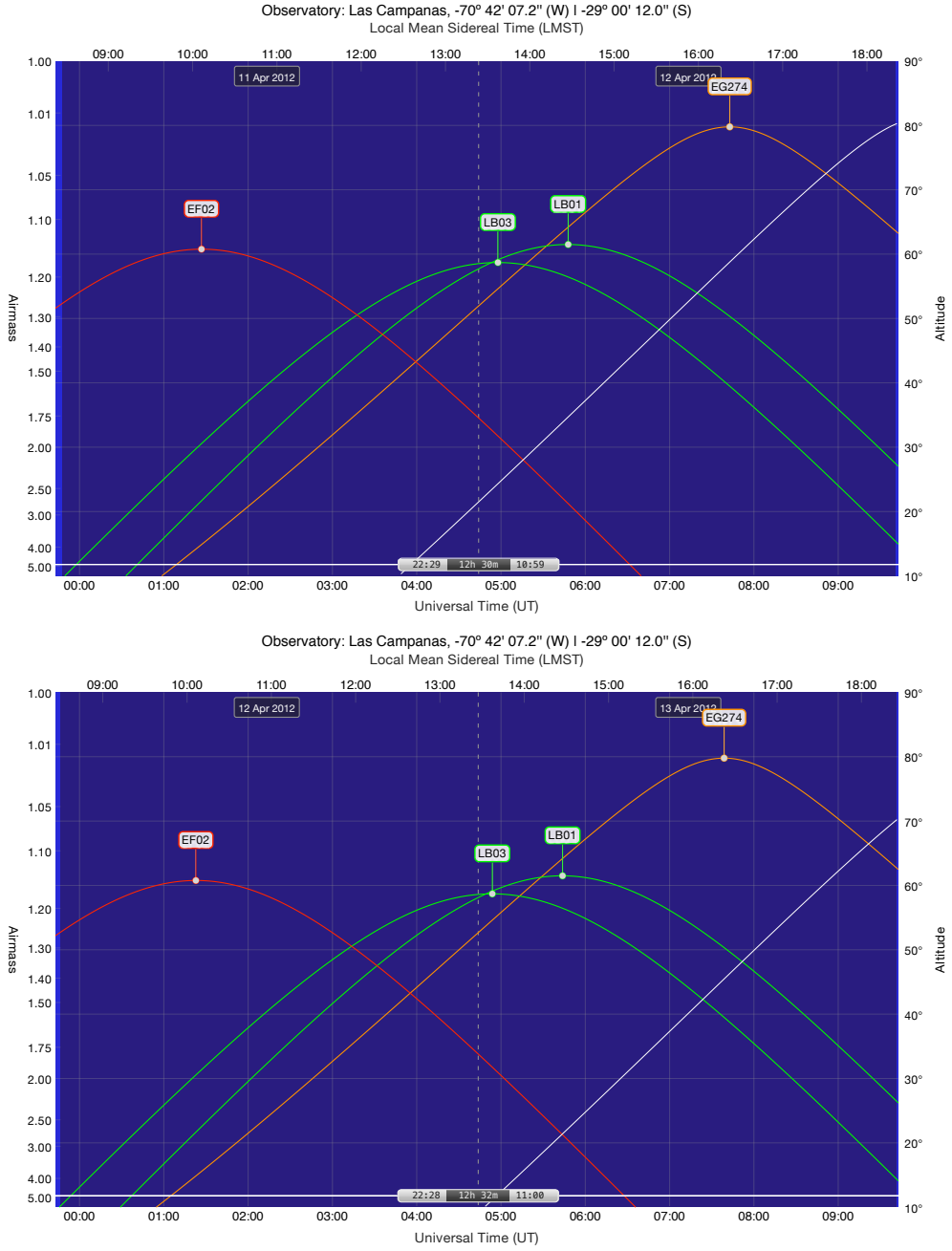

Figure 4.4: Observed object airmass tracks for April 11th and 12th, 2012. The red line is the airmass track of the 'faint' object EF02, the green lines are the airmass tracks for the 'bright' objects LB01 and LB03, and the orange line is the airmass track for the reference star EG 274. The white line shows the airmass track of the Moon. Image prepared using iObserve: `http://www.onekilopars.ec/iobserve/`.

Table 4.3: Full names, shorthand labels, redshift, V-band apparent magnitude, minimum airmass, and time of occurrence for the final target quasar list for the observations of April 11th and 12th, 2012, on the Baade Telescope at the Las Campanas Observatory.

Name	Label	Redshift	m_V	Min. Airmass	Time (UT)
SDSS J09318-0000	EB01	3.211	18.920	1.143	0:55:00
SDSS J10191+0254	EB02	3.390	18.740	1.178	1:40:00
SDSS J14279-0029	LB01	3.365	18.570	1.138	5:52:00
SDSS J15026+0302	LB02	3.359	18.950	1.180	6:28:00
SDSS J13379+0218	LB03	3.333	18.480	1.170	5:04:00
SDSS J09256-0059	EF01	3.385	21.030	1.133	0:49:00
SDSS J10067+0013	EF02	3.327	21.300	1.146	1:28:00
SDSS J14549-0027	LF01	3.315	21.130	1.138	6:19:00
SDSS J15151-0017	LF02	3.267	21.070	1.140	6:40:00
SDSS J15421+0129	LF03	3.264	21.030	1.160	7:07:00

successfully. LB01 was only partially imaged, and during analysis it was found that the image quality of the three LB01 frames observed were too severely impacted by variable wind and sporadic cloud cover to be worth discussing, even for pedagogical purposes. The field around LB03 was not observed at all. For the rest of this thesis we focus solely on the analysis of the completed EF02 field observations, and on a discussion of the general techniques for observing tunable filters.

4.3 Modelling the EF02 field

The flux limits achieved on the nights of April 11th and 12th, 2012, were not sufficient for us to expect to detect any candidate Lyα galaxies in the EF02 field. There were a number of factors that lead to the low sensitivity levels achieved: the lunar phase and the available quasar selection on the nights allocated, the decision on the day to use 1×1 CCD binning, and the poor weather on the night. A full discussion of the observational procedure and the conditions during the observations is presented in chapter 5.

We begin our discussion of these sensitivities by looking in detail at the expected

flux limits and corresponding expected galaxy counts, by comparing the conditions assumed in the proposal with those experienced during observation. In the process we quantify the effect that the conditions and decisions had on the final expected galaxy counts. To accomplish this, we need a model that converts a flux limit into an expected observable galaxy count. The model described in chapter 3 is purpose built for this, but requires some augmentation in order to account for the differences in quality between the five frames making up the EF02 observations.

4.3.1 Calculating the EF02 survey volume

The monochromatic spot for each MMTF exposure, as discussed in section 4.1, is 13.8 arcminutes in diameter at the wavelengths we observe at, centred on the optical axis. This translates to 4140 pixels on the Mosaic2 camera CCDs. Because this axis remains fixed on the CCDs between exposures, while the observed field does not, the monochromatic spot drifts slightly across the observation. Our goal is to compare the observed galaxies within the monochromatic spot of each of the five frames, and so we first create a mask of the monochromatic spot observed in each frame and stack these to create a composite mask used when detecting objects.

The composite monochromatic spot is smaller in area and no longer perfectly round, owing to the changing orientation of the component masks. To simplify modelling this irregular shape in our three-dimensional modelling of the survey, we counted the total number of unmasked pixels in the composite spot mask and determined the radius of a circle with the equivalent area. When stacked across all five of the frames, the equivalent spot shrinks from a diameter of 4140 pixels to an effective diameter of 3520 pixels, a 28 % reduction in total survey volume, yielding an effective survey area of 22.8 pMpc^2. Figure 5.2 (page 120) shows a visual comparison of the actual and effective monochromatic spot for the 5260 Å frame.

While this assumption does not model the edges of the volume perfectly, particularly where the mask shape is most irregular, it does accurately model the central volume where most of the galaxies are expected to reside. With a more sensitive observation, where the edges of the volume would account for a larger galaxy count, it would be possible to leave in these additional volumes and account for the wavelength drift outside of the monochromatic spot. However, this would increase the complexity of the modelling and candidate inspection, and given the sensitivities of the actual observations we neglected this additional complication.

The total depth of the survey spanned the wavelengths between 5230 Å and 5290 Å, spanning the FWHM across each of the five frames. This translates to a depth of 10.21 pMpc and, when we account for redshift space distortions, this stretches to 10.83 pMpc. If we consider just the central three frames, the combined depth is 6.125 pMpc, stretching to 6.547 pMpc considering redshift space distortions. For just the central frame alone, the depth is 2.042 pMpc, stretching to 2.204 pMpc with redshift space distortions.

This gives a cylindrical shaped total volume of 246.7 pMpc^3 across all five frames, 149.2 pMpc^3 across the central three frames, and 50.22 pMpc^3 for the central frame. We construct our spherical model so that the largest shell just encloses the entire cylindrical volume, and then determine the fraction of each concentric shell that falls within the volume to determine the final galaxy counts. This is done in a similar fashion to the rectangular survey volumes described in section 3.3.1 (page 53).

4.3.2 MMTF transmissivity

The transmissivity of the MMTF is a function of where the tunable central wavelength of observation falls on the blocking filter. The 5236 Å setting we used in the observation of EF02 falls on the shoulder of the MMTF5290 blocking filter's response curve.

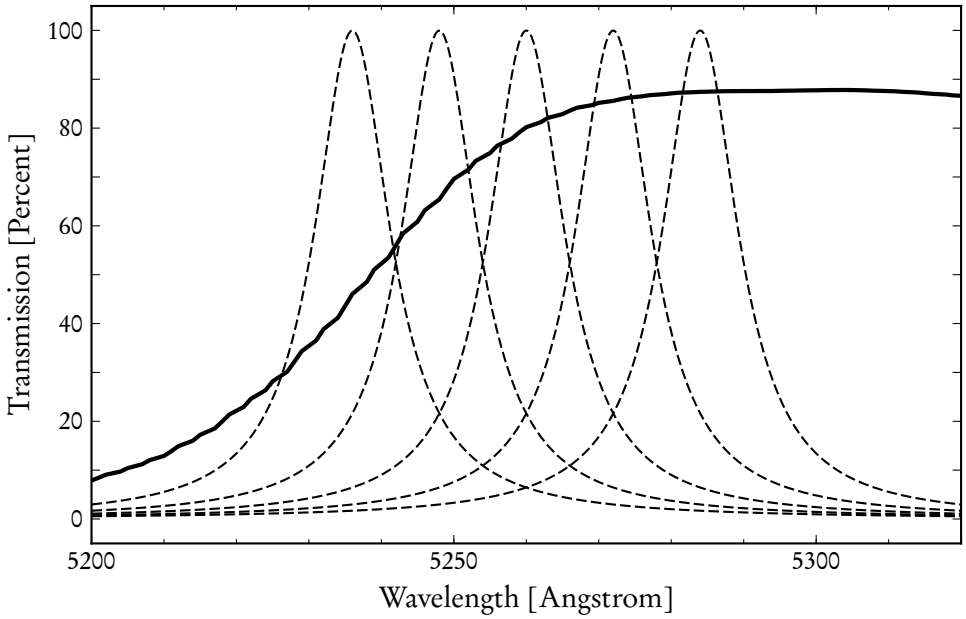

Figure 4.5: Response curves of the EF02 narrowband wavelengths relative to the MMTF5290 blocking filter. The solid black line is the response curve of the MMTF5290 blocking filter and the dashed lines are the five narrowband filters. The narrowband profiles are assumed to be Lorentzian, with a FWHM of 12 Å.

This causes the 5236 Å frame to have a total transmitted flux of 79 %, compared with the other four frames that fell within the flat plateau of the blocking filter's optimal transmissivity of ~90 %. This can be seen visually in figure 4.5.

This effect is accounted for in the MMTF exposure time calculator, and is a contributing factor to the lower flux limit and corresponding lower expected galaxy counts we find in the 5236 Å frame. This is later seen when comparing the flux limits of the 5236 Å and 5284 Å frames from the observing proposal, shown in table 4.4.

4.3.3 Accounting for frame-specific flux limits

With the survey volume model in place, the final variable required to calculate the number of expected visible galaxies is the minimum visible Lyα luminosity, which is derived from the flux limit of the observations. This is complicated for our five

frame observations of EF02, as each frame has a unique minimum sensitivity based on the variable observing conditions and the transmissivity of the MMTF5290 blocking filter. Because of the symmetric nature of both our modelling, and cylindrical volume surveyed, we can account for this through geometry.

We first divide the simulated full-survey volume into two sub-volumes, one corresponding to the volume of just the central 5260 Å frame and one corresponding to the volume of the three central 5248 Å, 5260 Å, and 5272 Å frames. In both cases we account for redshift-space distortions. We then calculate the galaxy counts expected in the full volume and each of the sub-volumes for the specific flux limits in each of the five wavelength frames.

For the two outside frames, at 5238 Å and 5284 Å, we calculate the expected galaxy count by taking their specific galaxy counts for the full-survey volume and subtracting their specific expected galaxy counts for the three-frame sub-volume. Dividing this total by two we arrive at the total expected galaxy count for each of the two outer frames. We repeat this process for the two middle frames, at 5248 Å and 5272 Å, this time subtracting the expected galaxy counts for the central single frame sub-volume from the expected galaxy counts of the three-frame sub-volume, and dividing by two. For the central 5260 Å frame, we simply calculate the expected galaxy counts for the central single frame sub-volume.

In each case, the individual frame flux limits were used to pull galaxy counts out of a single run of the computationally intensive analytical simulation using different minimum Lyα luminosity cuts. This makes it a simple matter for us to calculate the expected galaxy counts for the entire volume assuming a number of different experimental configurations and conditions.

4.4 Flux limits and expected galaxy counts

Given the large disparity between the flux limits we calculated in our proposal and the experimentally observed limits, it is useful to compare the different contributions to the final flux quantitatively. In particular, the impact of the lunar phase, the seeing on the night, and the CCD binning were all important factors in the observations of EF02 that deserve particular attention.

In this section we lay out the calculated flux limits for a series of scenarios, starting with the most optimistic flux limits from the proposal and going through the major causes of signal quality degradation, ultimately arriving at the actual flux limits from the observations taken in April, 2012. In each case we outline the values used to calculate the frame-specific limiting flux – using the MMTF exposure time calculator[6] – and the associated expected galaxy counts for the volume of each frame, as calculated using the methods described in section 4.3.

4.4.1 Proposal flux limits

When writing the proposal, we assumed the following parameters to calculate a set of generally expected flux limits:

- 0.6″ seeing: the median seeing of the Las Campanas observatory,
- 1.2 airmass: assuming an 80° altitude apex, this is the largest airmass over the best five hour observing period for an object,
- −2 coarse Z: the coarse adjust for the etalon air-gap appropriate for z~3.3 observations of Lyα emission,
- 4 lunar phase: on a scale of 0 (new moon) to 14 (full moon),

[6] `http://www.astro.umd.edu/~veilleux/mmtf/expcalc1.php`

- 2×2 CCD binning: the size of the output image, with a larger binning trading off spatial resolution for an increased SNR and decreased camera readout time, and

- 1 h exposure time: a reasonable integration time that ensures enough time to observe a full five frame volume in one night.

We used these values, along with the individual central wavelengths of the EF02 frames, to calculate the point source flux limits shown in table 4.4. For comparison we included values assuming a SNR of both 3 and 5, the lower of which allows for the detection of objects straddling across two adjacent frames. The main difference in the flux limits between the frames are the different transmissivities across the central wavelengths shown in figure 4.5.

To calculate the minimum Lyα luminosity, presented in table 4.4 and used throughout the rest of this analysis, we assume the Lyα galaxies are emitting equally in all directions. From the redshift that corresponds to rest frame $\lambda_{\mathrm{Ly}\alpha}$ emission, we calculate the luminosity distance to the object and use this to convert from the flux limit to the minimum detectable Lyα luminosity in each frame.

These flux limits correspond to an average expected galaxy count for the entire volume between 32 and 41, depending on how prevalent the quasar's UV flux is within the volume. For comparison, our model predicts a count of 16 galaxies in the field, assuming the same volume at the same redshift without a central quasar. These galaxy counts would have given the statistical leverage necessary to explore the suppression of galaxy formation. Table 4.5 gives the expected counts for each frame volume and the total for a SNR of both 3 and 5.

Table 4.4: Flux limits in each of the five EF02 wavelength frames, assuming the settings and conditions outlined in the proposal.

	SNR 3		SNR 5	
Frame [Å]	Flux limit*	$L_{Ly\alpha}{}^\dagger$	Flux limit*	$L_{Ly\alpha}{}^\dagger$
5236	1.70	1.75	2.98	3.07
5248	1.54	1.60	2.71	2.81
5260	1.55	1.62	2.71	2.83
5272	1.50	1.58	2.71	2.85
5284	1.45	1.54	2.54	2.70

$^\star[10^{-17}\,\mathrm{erg\,cm^{-2}\,s^{-1}}]$ $^\dagger[10^{42}\,\mathrm{erg\,s^{-1}}]$

Table 4.5: Expected galaxy counts in each of the five EF02 wavelength frame volumes, assuming the proposal flux limits in table 4.4. Galaxy counts are presented for the average expected without a quasar present (Field), with a quasar present and assuming an isotropic UV boost (Q_{ON}), and with a quasar present with no UV boost (Q_{OFF}). These counts are given assuming a SNR of both 3 and 5.

	SNR 3			SNR 5		
Frame [Å]	Field	Q_{ON}	Q_{OFF}	Field	Q_{ON}	Q_{OFF}
5236	2.5	4.0	3.7	1.1	1.8	1.6
5248	3.5	8.6	7.0	1.5	4.0	3.1
5260	3.5	15	9.5	1.5	7.2	4.4
5272	3.5	8.7	7.0	1.4	3.9	3.1
5284	3.0	4.8	4.4	1.3	2.2	2.0
Total	16	41	32	6.7	19	14

Table 4.6: Flux limits in each of the five EF02 wavelength frames, assuming a seeing of 0.6″ and a lunar phase of 9. The limits are shown assuming both a 2×2 and 1×1 CCD binning. The remaining settings and conditions are unchanged from the proposal, and assume a target SNR of 5.

	2×2 binning		1×1 binning	
Frame [Å]	Flux limit*	$L_{\mathrm{Ly}\alpha}{}^\dagger$	Flux limit*	$L_{\mathrm{Ly}\alpha}{}^\dagger$
5236	4.56	4.70	8.99	9.27
5248	3.85	4.00	7.60	7.88
5260	3.98	4.16	7.84	8.20
5272	3.78	3.98	7.45	7.84
5284	3.58	3.80	7.06	7.49

$^\star[10^{-17}\,\mathrm{erg\,cm^{-2}\,s^{-1}}]$ $^\dagger[10^{42}\,\mathrm{erg\,s^{-1}}]$

4.4.2 Optimal seeing flux limits

With full knowledge of the target selection from the nights eventually allocated, we can degrade the proposal flux limits to a best case scenario for observing EF02 at a seeing of 0.6″. We begin by changing lunar phase from the assumed dark/grey value of 4 to the grey/bright value of 9, matching the conditions on April 11$^{\mathrm{th}}$ and 12$^{\mathrm{th}}$, 2012. Because of the MMTF's high reflectivity, the additional moon glow adds to the sky background and lowers the SNR, raising the minimum detected flux. This change, from 4 to 9, yields a new set of flux limits listed in table 4.6.

Considering just the 5260 Å frame, this change in lunar phase causes the flux limit to jump from the proposal value of $1.55 \times 10^{-17}\,\mathrm{erg\,cm^{-2}\,s^{-1}}$ to $3.98 \times 10^{-17}\,\mathrm{erg\,cm^{-2}\,s^{-1}}$, a reduction of the flux limit by a factor of ~2.5. It is clear that the lunar phase played a much larger role than expected, demanding a requirement for darker conditions in future proposals.

Our decision to change the CCD binning to 1×1, while ensuring that we would be able to better resolve the smaller candidate Lyα galaxies, had a significant impact

on the flux limit. This decision gave a new flux limit of 7.067×10^{-17} erg cm^{-2} s^{-1}, with a corresponding minimum Lyα luminosity of 7.511×10^{42} erg s^{-1}. This increased the flux limit a factor of 1.9 beyond the lunar phase limit, for combined impact of 4.8 over the proposal limits.

These flux limits, assuming a 2×2 CCD binning, correspond to an average expected galaxy count for the entire volume between 8.1 and 11, depending on how prevalent the quasar's UV flux is within the volume. For comparison, our model predicts a count of 3.7 galaxies in the field, assuming the same volume at the same redshift without a central quasar. Assuming a 1×1 CCD binning, the expected galaxy count drops to between 2.6 and 3.7 including the quasar's effects, and 1.1 in the field.

With a 2×2 binning, these galaxy counts would have been significant enough to provide a test for the quasar model and for tunable filter Lyα searches, but would not have been able to provide the spacial clustering statistics needed to explore the suppression of galaxy formation. Table 4.7 gives the expected counts for each frame sub-volume and the totals for both 2×2 and 1×1 CCD binning.

4.4.3 Actual seeing flux limits

To determine the actual seeing flux limits for each observed EF02 frame, we add in the seeing and airmass of the individual observations to the exposure time calculator. The observed airmass values were clustered around our assumed proposal value of 1.2. Only the 5236 Å and 5260 Å frames noticeably deviated from this, with observed airmasses of 1.60 and 1.33 respectively. The main degradation came from the final calculated seeing for each frame. These ranged from 0.957″ to 1.39″, and were exacerbated by the requirement in the data reduction pipeline to degrade the three exposures for each frame to match the one with the worst seeing. The airmass,

Table 4.7: Expected galaxy counts in each of the five EF02 wavelength frame volumes, assuming the optimal seeing flux limits in table 4.6. Galaxy counts are presented for the average expected without a quasar present (Field), with a quasar present and assuming an isotropic UV boost (Q_{ON}), and with a quasar present with no UV boost (Q_{OFF}). These counts are given assuming both a CCD binning of 2×2 and 1×1.

	2×2 binning			1×1 binning		
Frame [Å]	Field	Q_{ON}	Q_{OFF}	Field	Q_{ON}	Q_{OFF}
5236	0.52	0.91	0.81	0.15	0.28	0.25
5248	0.81	2.3	1.8	0.24	0.78	0.60
5260	0.80	4.2	2.4	0.23	1.4	0.79
5272	0.81	2.4	1.8	0.24	0.79	0.60
5284	0.75	1.3	1.2	0.22	0.41	0.37
Total	3.7	11	8.1	1.1	3.7	2.6

seeing, flux limit, and corresponding Lyα luminosity limit from the exposure time calculator can be seen in table 4.8.

Our observations of the 5236 Å frame suffered the most from conditions on the night, with the flux limit jumping by an additional factor of 2.3. The 5260 Å frame, which had the lowest seeing at 0.957, still had a jump in its flux limit of 1.6. When we compare the proposal flux limits – which assumed 2×2 binning, a darker lunar phase, and reasonable weather conditions – with those achieved on the night for our best quality frame, 5260 Å, we find that the flux limits were 8 times higher than expected. This corresponds to a raising of the minimum detectable Lyα luminosity from 1.62×10^{42} erg s^{-1} to 1.30×10^{43} erg s^{-1}.

These flux limits correspond to an average expected galaxy count for the entire volume between 0.83 and 1.3. Assuming we had observed with a 2×2 CCD binning, these numbers rise to between 3.0 and 4.4. Table 4.9 gives the expected counts for each frame volume and the total for both 2×2 and 1×1 CCD binning.

Table 4.8: Flux limits in each of the five EF02 wavelength frames using the individual frame viewing conditions in the exposure time calculator during the observations of April, 2012. The limits are shown assuming both a 2×2 and 1×1 CCD binning. The remaining settings and conditions are unchanged from the optimal conditions analysis and assume a target SNR of 5. Note the changed flux and luminosity units as compared with the previous flux limit tables.

			2×2 binning		1×1 binning	
Frame [Å]	Seeing [″]	Airmass	Flux limit*	$L_{Ly\alpha}{}^\dagger$	Flux limit*	$L_{Ly\alpha}{}^\dagger$
5236	1.39	1.60	1.0	1.1	2.1	2.1
5248	1.10	1.15	0.70	0.73	1.4	1.4
5260	0.957	1.33	0.63	0.66	1.2	1.3
5272	1.17	1.26	0.73	0.77	1.4	1.5
5284	1.32	1.18	0.78	0.82	1.5	1.6

$^\star[10^{-16}\,\mathrm{erg\,cm^{-2}\,s^{-1}}]$ $^\dagger[10^{43}\,\mathrm{erg\,s^{-1}}]$

Table 4.9: Expected galaxy counts in each of the five EF02 wavelength frame volumes, assuming the actual observed flux limits in table 4.8. Galaxy counts are presented for the average expected without a quasar present (Field), with a quasar present and assuming an isotropic UV boost (Q_{ON}), and with a quasar present with no UV boost (Q_{OFF}). These counts are given assuming both a CCD binning of 2×2 and 1×1.

	2×2 binning			1×1 binning		
Frame [Å]	Field	Q_{ON}	Q_{OFF}	Field	Q_{ON}	Q_{OFF}
5236	0.11	0.21	0.19	0.02	0.05	0.04
5248	0.28	0.90	0.69	0.07	0.26	0.19
5260	0.36	2.1	1.2	0.09	0.65	0.33
5272	0.25	0.83	0.63	0.06	0.24	0.17
5284	0.18	0.35	0.32	0.04	0.09	0.08
Total	1.2	4.4	3.0	0.29	1.3	0.83

4.4.4 *Directly calculated flux limits*

We finally calculate the flux limits directly from the data itself. This is usually done in one of two ways: either by using the measured RMS sky counts in each of the images and extrapolating this background noise to the photometric aperture used, or by inserting and recovering artificial sources. Using artificial sources is the more powerful technique but for our purposes – mainly as a check of the exposure time calculator efficacy – we will use RMS sky method.

To obtain the flux limits from the data directly we first begin by choosing an appropriate size for the photometry aperture. At redshift 3.3 the galaxies we wish to resolve are ~1.6″ in diameter, which at the observed 1×1 binning is equivalent to a diameter of 8 pixels. To ensure we collect all the counts from the galaxies we increase this diameter by a number of pixels equal to the measured seeing in the observations. We assume a circular aperture and multiply this area, in units of square pixels, by the measured RMS sky counts of each observation to get a rough value for the total background counts within an aperture. We want a flux limit for a detection at a SNR of 5, so we multiply the calculated background counts by 5 and divide through by the exposure time of 3600 s to arrive at the minimum detectable flux in units of cts s^{-1}. These fluxes are then converted into the magnitudes shown in table 4.10 using the photometric calibration described in section 5.4.1 (page 112).

These magnitudes are converted to flux limits in the desired units of erg cm^{-2} s^{-1} and to minimum detectable $L_{\mathrm{Ly}\alpha}$ using equation (5.9) (page 119). To better compare with the other flux limit calculations in this chapter an estimation of the direct flux limit was made assuming a 2×2 CCD binning. This rough calculation was done by halving the aperture size and doubling the RMS sky and recalculating the magnitudes shown in table 4.10. The final flux limits for both a 1×1 CCD binning and a 2×2 CCD binning are shown in table 4.11.

Table 4.10: Directly measured magnitudes for the five EF02 wavelength frames using the reduced photometric images for the observations of April, 2012. Aperture width and extinction magnitude calculated using the seeing and airmass values from table 4.8 assuming a 1×1 binning.

Frame [Å]	Aperture*	RMS sky†	SNR5 flux‡	m_{INST}	m_{EXT}	m_{ZPT}	m_{TOT}
5236	15.0	21.0	5.12	−1.77	0.256	22.1	20.6
5248	13.5	11.5	2.29	−0.898	0.184	22.2	21.5
5260	12.8	13.7	2.44	−0.970	0.213	22.3	21.5
5272	13.9	10.1	2.11	−0.812	0.202	22.3	21.7
5284	14.6	8.41	1.96	−0.728	0.189	22.3	21.7

*[px] †[cts px^{-1}] ‡[cts s^{-1}]

Table 4.11: Flux limits in each of the five EF02 wavelength frames, calculated directly from the images. The limits are shown assuming both a 2×2 and 1×1 CCD binning assuming a minimum SNR of 5.

	2×2 binning		1×1 binning	
Frame [Å]	Flux limit*	$L_{\mathrm{Ly}\alpha}{}^\dagger$	Flux limit*	$L_{\mathrm{Ly}\alpha}{}^\dagger$
5236	2.3	2.4	4.6	4.7
5248	0.97	1.0	1.9	2.0
5260	0.95	0.99	1.9	2.0
5272	0.83	0.88	1.7	1.8
5284	0.79	0.84	1.6	1.7

*[10^{-16} erg cm^{-2} s^{-1}] †[10^{43} erg s^{-1}]

Table 4.12: Expected galaxy counts in each of the five EF02 wavelength frame volumes using the directly measured flux limits in table 4.11. Galaxy counts are presented for the average expected without a quasar present (Field), with a quasar present and assuming an isotropic UV boost (Q_{ON}), and with a quasar present with no UV boost (Q_{OFF}). These counts are given assuming both a CCD binning of 2×2 and 1×1.

	2×2 binning			1×1 binning		
Frame [Å]	Field	Q_{ON}	Q_{OFF}	Field	Q_{ON}	Q_{OFF}
5236	0.020	0.044	0.037	0.003	0.008	0.007
5248	0.16	0.55	0.41	0.037	0.15	0.11
5260	0.17	1.1	0.61	0.038	0.31	0.15
5272	0.22	0.72	0.55	0.050	0.19	0.14
5284	0.20	0.37	0.34	0.048	0.096	0.085
Total	0.77	2.8	1.9	0.18	0.76	0.49

Comparing the flux limits in tables 4.8 and 4.11 we can see that the exposure time calculator underestimated the directly measured 1×1 CCD binning flux limits: by ~6 % for the 5284 Å frame, by ~25 % for the 5248 Å and 5272 Å frames, by ~35 % for the 5260 Å frame, and by ~55 % for the 5236 Å frame. Given the observing conditions on the night, particularly the intermittent cirrus clouds throughout the observing and which were especially present during the 5236 Å observations, the calculator gave reasonable estimates for our measured flux limits.

These flux limits correspond to an average expected galaxy count for the entire volume between 0.49 and 0.76. Assuming we had observed with a 2×2 CCD binning, these numbers rise to between 1.9 and 2.8. Table 4.12 gives the expected counts for each frame volume and the total for both 2×2 and 1×1 CCD binning.

To test the sensitivity of this model to the accuracy of the inferred quasar halo mass we ran the simulation varying only the quasar halo mass. In these modified simulations the assumed ionising flux from the quasar was unchanged, only the halo scaffolding hosting the potential Lyα galaxies changed to reflect the changed quasar

halo mass. Assuming a halo mass of twice that inferred directly from the measured quasar flux the expected galaxy count for the entire volume was between 0.53 and 0.83. For an assumed halo mass half that inferred from the quasar flux the expected galaxy count was between 0.45 and 0.69. These results show that the simulations of EF02 are not overly sensitive to exact quasar halo mass inferred. For future simulations predicting tens or hundreds of objects a more robust analysis of this relationship is likely warranted in order to give better constraints on any observed Lyα galaxy exclusion zones.

Given how small these expected galaxy counts are, it is likely that an analysis of these observations will result in a lack of candidate Lyα galaxies. To quantify this, we use a Poisson distribution with a mean equal to the average expected galaxy count to approximate our chances of detecting small numbers of Lyα galaxies in the data. The chances of detecting no Lyα galaxies is between 47 % and 61 %, depending on how influential the quasar's UV flux is on nearby transmission. Assuming a 2×2 CCD binning, this drops to between 6 % and 14 %, suggesting that we would most likely have detected at least one galaxy candidate. Regardless of CCD binning, these numbers are far too small to be of use in constraining the UV suppression of galaxies. These likelihoods are provided in table 4.13.

We note that this modelling assumes no suppression of galaxy formation, and so represents an upper bound on the likelihood of detection. However, the galaxies that would be detectable given the high flux limits would most likely be immune to any direct UV suppression owing to their size and $T_{\rm vir}$.

4.4.5 Future observations

There were a number of decisions and observing conditions that led to the large flux limits in these observations: deciding to use 1×1 over 2×2 binning on the

Table 4.13: Poissonian likelihood of detecting galaxies in observations assuming the average expected galaxy counts in table 4.12. Likelihoods are presented as percentages for the average expected galaxy counts without a quasar present (Field), with a quasar present and assuming an isotropic UV boost (Q_{ON}), and with a quasar present with no UV boost (Q_{OFF}). These percentages are given assuming both a CCD binning of 2×2 and 1×1.

	2×2 binning			1×1 binning		
Count	Field [%]	Q_{ON} [%]	Q_{OFF} [%]	Field [%]	Q_{ON} [%]	Q_{OFF} [%]
0	46	6	14	84	47	61
1	36	17	28	15	36	30
2	14	24	27	1	13	7
3	4	22	17	0	3	1
4	1	16	8	0	1	0
5	0	9	3	0	0	0

CCD, the comparatively high airmass of the quasar candidates that were visible on the allocated observing nights, the abnormally poor seeing during the observations, and the weather conditions that cut short the second night of observations. Any two or three of these setbacks would have led to a flux limit that modelling suggests would have allowed for the detection of ~10 galaxies across at least two quasar fields. Taken together they led to an expected galaxy count of ~1 on just the one quasar field. Any future proposals to repeat or extend this experiment can mitigate these issues through a more detailed observation plan. Below we suggest improvements to our methodology based on our experience during the April, 2012, observations.

- Select 20 to 30 specific quasars in the proposal, and request windows of time that have them tracking across the sky optimally. While using a tunable filter is flexible in that there are year-round targets, the ultimate goal is to measure the field around some of the most luminous $z \sim 3$ quasars and compare them to those ~100 times less luminous. The objects present during our allocated time did not provide the range of luminosities to best test our hypothesis, nor

were they high enough in the sky to provide an optimal time-on-target during the observations.

- Better appreciate the long overhead times when calculating the time required per quasar field. The nature of the targets available on the nights allocated meant that the additional overhead required for 1×1 binning, and the time needed to compensate for the inclement weather was not practical. A combination of pre-selected targets that were better staggered throughout the night and an earlier discussion of how to best image these specific targets with the instrumentation scientist will ensure a much higher chance of a successful observation.

- Plan to observe two objects per night, ensuring that the visible track of the two quasars are staggered across the observing night, and that they are at a high enough elevation to ensure good viewing throughout the night. This will ensure there is enough time to account for all calibration and CCD readout requirements for a minimal level of field completion at low airmasses. The observations of the central and middle two frames are the most important and should be observed at the lowest airmass with the highest priority, followed by the outer two frames. This should be repeated for as long as the objects are visible, getting as much additional integration time as possible.

- Have your modelling for each of the proposal targets completed ahead of time, and be ready to recalculate expected galaxy counts given the conditions on the night. Had the modelling been easily accessible and flexible to changes in flux limit, the decision to change from 2×2 to 1×1 binning would have been overturned given the worsening conditions on the night. In the preparation of this thesis we have built the software framework needed to model these

surveys quickly, producing the values found in tables 4.4, 4.6, 4.8 and 4.11 in a matter of minutes once the initial quasar field modelling had been processed. Any continuation of this work would make good use of these tools during both the proposal generation and the actual observations.

4.5 Summary

In this chapter we have discussed tunable narrowband optical imaging and its application to Lyα galaxy searches at high-redshift. We have described how to apply the modelling laid out in chapters 2 and 3 to the design of the five frame observations of the EF02 quasar, and how to combine this modelling with the observational flux limits to calculate the expected number of visible Lyα galaxies. Details on how the allocated observing nights and the seeing conditions during the observations impacted upon the expected Lyα galaxy count were presented, breaking down the impacts of each deviation from the observing proposal. Finally, we made suggestions for the design of future tunable filter Lyα galaxy searches based on this analysis. The main result from this chapter is that the observations taken were not able to reach the necessary sensitivity expected for the detection of Lyα galaxies, nor were enough fields imaged to conduct the designed experiment properly. A through discussion of the observations taken of the EF02 field is presented in chapter 5, along with an overview of the novel techniques required to reduce and interpret tunable filter observations.

Chapter 5

Analysis of the EF02 quasar field

The observations of the EF02 field provide us with the opportunity to discuss the novel techniques needed to reduce and analyse data from tunable filter observations. In this chapter we outline the calibrations required to observe with the MMTF instrumentation and describe in detail data reduction required to produce science images using the MMTF pipeline. We also perform a full analysis of the science images produced by the April, 2012, observations and show that these images contain no detectable Lyα galaxies, which is consistent with the modelling presented in chapter 4.

5.1 Calibration of the MMTF

Compared to most traditional observations with broad- and narrowband filters the calibration process of the MMTF is a complicated affair. In addition to standard camera readout calibrations, the piezoelectric control system for the two plates that make up the etalon in the MMTF must also be calibrated and the pixel location of the optical axis on the IMACS camera must be determined. This requires calibration during the afternoon prior to an observing run, and corrections to the calibration must be made throughout the observations themselves. In the following sections a brief outline of the calibration process is presented.[1]

[1]The entire calibration process is described on the official MMTF website: `http://www.astro.umd.edu/~veilleux/mmtf/`

5.1.1 Calibrating the air-gap controller

The optics behind the interference pattern produced by the etalon dictate that the transmitted wavelength of the etalon changes as a function of radius from its centre. This does not affect our observations because this variation is small enough to ignore in the central monochromatic region where we conduct our observations. This fact can, however, be used to quickly calibrate the etalon plate orientation to high precision.

To begin calibration, a single element light source is chosen that has identifiable spectral features falling within the chosen blocking filter. The etalon spacing is roughly set so that the central wavelength is slightly different from a spectral feature of the light source, preferably a single peak. The light from this spectral line will therefore transmit not in the central, monochromatic region of the filter, but rather in a narrow concentric ring some radius from the centre of the etalon. This ring and its derived properties are the key to the calibration process.

If the two plates forming the etalon are not optimally parallel this ring will deviate from circular and it is this deviation which allows for a controlled calibration of the etalon. This is done by taking an image of the ring and averaging the pixel values azimuthally around the etalon centre point. Plotting the resultant pixel average gives a one-dimensional emission-line spectrum of the original monochromatic light source. This emission-line should be symmetric and its peak should match the expected line profile. Images of the ring are taken at multiple piezoelectric controller settings and presented for visual inspection. The optimal settings are those that provide the narrowest and most symmetric emission-line profile. This parallelisation process is done the afternoon before observing and is monitored throughout the night, though it is usually not necessary to perform this calibration a second time during the same observing run.

Once the plates are parallel, we calibrate the optical axis of the MMTF. This is the location on the pixel grid of the camera that falls directly under the centre of the etalon. This is always in the centre of the field of view, but shifts slightly between MMTF observations due to the periodic remounting of the IMACS camera. This calibration makes use of the fact that there is a faint reflection between the camera and the etalon (~0.5 %) which is symmetric around the optical axis. A pinhole mask is placed in front of the MMTF that contains eight square aperture holes in the upper half of the central field of view. The screen making up the IMACS hatch is then back-lit with light from a quartz-halogen lamp. This light travels through the eight apertures and onto the camera, where a fraction of the light reflects back onto the etalon and then back onto the camera. This faint reflection appears in the bottom half of the central field of view, exactly symmetric to the eight apertures around the optical axis. The optical axis is then simply the point at which the lines connecting the eight apertures and their reflection ghosts intersect, given in camera pixel coordinates.

Finally we calibrate the width of the air-gap between the two etalon plates. This is accomplished by taking a low-resolution spectrum of the rings generated by the same light source used in parallelisation, fitting this to a high-resolution reference, and mapping the controller settings to the wavelengths of the known features. The low-resolution spectra are produced by taking ~100 images at wavelengths over the range of roughly two full orders of the fundamental wavelength. The resulting 'data sausage' – a data cube narrow in X and Y but extended in Z – is then created by performing the same azimuthal average done in the parallelisation calibration for each image, finding the intensity of the peak in the resulting emission-line spectra, and plotting these intensities as a function of the corresponding controller settings. This fitting provides the reference air-gap controller settings to be used throughout

the observations that night. This process takes approximately thirty minutes, dominated mainly by the readout speed of the camera.

Thermal expansion and contraction throughout the night causes the air-gap width to drift throughout the observing run and must be continually calibrated. This calibration is performed by taking a single ring image, using the same light source as above, at a specific controller setting that matches a calibrated reference ring image. The difference in radius of the calibration image to the reference image gives the drift of the instrument in wavelength, and therefore in the width of the air-gap. This is converted into the appropriate piezoelectric controller settings via a simple linear process, returning the filter to the desired wavelength. During the early part of the observing run, when thermal fluctuations are at their peak, this drift calibration will need to be conducted roughly once every twenty to thirty minutes. As the temperature stabilises later in the night this correction is only needed once every hour. This update takes about five minutes, and this time is dominated mainly by the readout speed of the camera.

Our observation of $\lambda_{\mathrm{Ly}\alpha}$ at $z \sim 3.3$ corresponds to an observed wavelength of ~5250 Å, therefore the MMTF's 5290 Å blocking filter was used throughout the experiment. At this wavelength the appropriate choice of monochromatic light for calibration was the internal neon arc lamp built into the IMACS instrument, which was used for the ring-based calibrations mentioned above.

5.1.2 Calibration images

The usual optical calibrations used in broadband observing still apply to tunable filters, and are related to the camera in the IMACS instrument that houses the MMTF. IMACS has two cameras, Mosaic1 and Mosaic2, at the $f/4$ and $f/2$ focal points respectively. MMTF uses the Mosaic2 camera which consists of a mosaic of eight

rectangular charge-coupled devices (CCDs), each with a grid of 2048×4096 pixels. Each pixel in the CCD has its own noise level due to the electronics involved, and has a different sensitivity to light due to the optical system that light travels through before being recorded. This pixel-to-pixel variation in the CCDs is what is measured during the camera calibration and then removed from science images produced by the MMTF.

Measuring the baseline electrical noise of the CCDs is straightforward: ensure there is no light incident on the camera and that the temperature of the camera is similar to that during observing your science images, and then take multiple images with an exposure time of zero seconds. Averaging these images gives the in-built CCD noise and this can be subtracted from the science images to ensure that only the signal accumulated by the objects of interest are in the reduced science images. A similar effect is produced when there is a charge accumulation on the CCD not related to incident light during an exposure. For the modern CCDs in the Mosaic2 camera, this 'dark current' is negligible – typically only a handful of counts per hour – and is therefore not part of the image calibration.[2]

Determining the pixel-to-pixel light sensitivity caused by the optical system is known as flat-fielding. In the Mosaic2 camera, artefacts are introduced to the image by the shadows from random out-of-focus dust, and from consistent vignetting caused by the tertiary mirror and its mounting assembly. Removing these artefacts is accomplished by taking a series of short, blank images with each observing filter of the IMACS hatch screen, back-lit with the light from a quartz-halogen lamp. Averaging the resultant images and subtracting them from the science images removes these effects.

A final set of calibration images, not related to the calibration of the camera,

[2] `http://www.lco.cl/telescopes-information/magellan/instruments/imacs/user-manual/the-imacs-user-manual`

is taken in each filter of a known reference object with a well measured spectrum. These images are corrected for CCD bias in the same way that the science images are, and are used to tie objects detected in the science images to a particular system of brightness measure for comparison with previously detected objects. The particulars of the photometric calibration process will be described in section 5.4.1.

5.2 Observational procedure

Before we began observing our shortlist[3] of candidate quasars was vetted by the telescope operator to ensure their suitability for observations. For the two early bright objects, EB01 and EB02, and one of the two early faint objects, EF01, there were no guide-stars available in their immediate vicinity. This meant that there was no way to track them across the sky during a long integration with any stability, and required that we choose the remaining early faint object, EF02, as the first target to observe. We paired EF02 with the late bright object LB01 to provide the target selection for the first night. For the second night our primary objective was to ensure that any missing wavelengths from EF02 and LB01 were recorded and then, time-permitting, complete a third set of frames for the object LB03.

We were informed by the instrumentation scientist that using a 2×2 binning on the CCD was not advisable, as it would lower the spatial resolution for our desired objects. At redshift 3.3 the galaxies we wanted to resolve were ~1.6″ in diameter, which at a 2×2 binning would be equivalent to 4 pixels. This would effectively double the readout time of the camera, to the point where the time margin for completing observations in all frames for EF02 and LB01 would be thin. We relied on this advice and used a 1×1 binning throughout the experiment. This meant that our estimated minimum detectable $L_{\mathrm{Ly}\alpha}$ doubled to $\sim 3 \times 10^{42}\,\mathrm{erg\,s^{-1}}$ but that

[3] See table 4.3 (page 78).

we would have a better resolution for detecting galaxies.

EF02 has a redshift of $z = 3.327$, placing the redshifted Lyα wavelength of the quasar at 5260 Å. We chose the other wavelengths relative to this central wavelength in 12 Å increments, matching the expected FWHM of the MMTF at this wavelength range. Two wavelengths were chosen on either side for a total of five, contiguous, 12 Å filters: 5236 Å, 5248 Å, 5260 Å, 5272 Å, and 5284 Å. This same procedure was conducted for the other two targets. LB01, at redshift $z = 3.365$, had corresponding filters: 5282 Å, 5294 Å, 5306 Å, 5318 Å, and 5330 Å. LB03, at redshift $z = 3.333$, had corresponding filters: 5343 Å, 5355 Å, 5367 Å, 5379 Å, and 5391 Å.

From the filters loaded into the IMACS camera at the time of observing we selected the CTIO I $f/2$ filter, with a bandpass covering 7000 Å to 9000 Å, to provide shallow broadband imaging in the area around each quasar. Choosing the broadband filter on the night from those that were currently loaded into IMACS cut down on any wasted time required from switching instruments during the observing run, while still providing a check for low-redshift interlopers during candidate selection.

We next calibrated the MMTF as described in section 5.1. This included adjusting the air gap to obtain a visible neon reference ring and taking multiple images to parallelise the etalon. After that we took a data sausage of the neon lamp to calibrate the wavelength. We next took a set of pinhole images to determine where the optical axis fell on the pixel grid of the camera, which rounded out the baseline MMTF-specific calibrations. Finally we took a set of flat-field images using the quartz-halogen lamp at each of the ten wavelength settings used on the MMTF for EF02 and LB01. We took a neon reference ring before the flat-field images for each object and used this to maintain calibration of the air-gap throughout calibration.

We began observations of EF02 in earnest with the onset of twilight on April 11$^{\text{th}}$, 2012. Four of the five narrowband frames were completed before EF02 set

for the evening, leaving the broadband frame and one narrowband frame for the following night. For each of these narrowband wavelengths, three twenty-minute observations were taken. Between each of these exposures there was roughly ten minutes of overhead, so each wavelength took roughly ninety minutes to complete. This included the target reacquisition between exposures, camera readout times, and MMTF wavelength calibration. To ensure the etalon maintained its parallelisation as the telescope tracked across the sky, we rotated the telescope between each target acquisition to the same relative gravity angle. This cut down on the amount of gravitational sagging that the etalon air-gap controller had to compensate for, meaning that we did not need to perform any additional parallelisation calibration during the observations.

For LB01 we completed the broadband frames and three of the five narrowband frames before it set for the night. The broadband images were taken as a set of three five-minute exposures, and for LB01 these had to be taken twice due to poor visibility conditions. In general the conditions on the night of the 11^{th} were bad for observing, with an average seeing of 0.94″ recorded in the control room during the observations for EF02, and 1.1″ for LB01. For reference, the median seeing at Las Campanas Observatory is 0.6″, with fifty percent of the seeing between 0.4″ to 0.8″ (Persson et al., 1990).

Finally, we took the required calibration images to end the observation. The first set were of reference star EG 274[4], chosen for its visibility at the end of the night after LB01 had set. We observed this star with each of the ten MMTF narrowband wavelengths for two fifteen-second exposures, and with the broadband filter for three one-second exposures. For the broadband filter the telescope was defocused to avoid over-saturation of the pixels in the camera. We took flat-field images

[4] http://www.eso.org/sci/observing/tools/standards/spectra/eg274.html

of the broadband filter with the quartz-halogen and a set of fourteen zero-second bias exposures to calibrate the science images during data reduction. Finally, we took quartz-halogen back-lit flat-field images for the five wavelengths specific to the final target, LB03.

During the second night inclement weather prevented most of the scheduled observations from taking place. Only the final narrowband frame and the broadband images of EF02 were completed before the observing run was cancelled. This occurred before LB01 was high enough in the sky to complete any of the missing frames on that target.

5.2.1 Summary of observations

Of the three objects to be observed, only the observations of EF02 were completed successfully. LB01 was missing both the 5318 Å and 5330 Å frames, and those frames that were observed were of poor quality. LB03 was not observed at all.

The first night had the better conditions of the two, with an average seeing of 1.0″. Of the 11hr of possible dark observing time, 80min were spoiled due to clouds. The second night had an average recorded seeing of 1.1″, and of the 11hr of possible dark observing time, only 130min were usable. Taken together, 46 % of the allocated observing time was unusable, and even the usable time was far below the median seeing conditions for the telescope. At the average seeing recorded at the telescope facility during the observations, the exposure time needed to reach the desired flux limit in each frame was approximately doubled (6700 s versus 3600 s).

The final data from the observations were not able to deliver the data quality required to detect Lyα galaxies at the target redshift. The final flux limits achieved for each science image in EF02 and their consequences for Lyα galaxy visibility are discussed in section 4.4 (page 83).

5.3 Data reduction

The raw data was reduced following the standard MMTF data reduction pipeline.[5] This process involves running a selection of software scripts provided by the MMTF team, written in the Perl programming language, that calls modules from the Image Reduction and Analysis Facility[6] (IRAF) to process the unique images from MMTF. These scripts handled the bookkeeping required to merge the individual readouts from each of the eight CCDs in the IMACS Mosaic2 camera, aligning them properly to form the final full-size science images. In the following sections we briefly describe each step in this process to give a feel for how raw exposures are turned into useful science images.

5.3.1 Overscan calibration

We first need to remove any short-timescale noise caused by the temperature of the individual CCDs at the time of observing. The ability to correct for this is built into the software that runs the CCD readout process. Before the stored science data is read out, the CCD is asked to make sixty-four virtual reads from the electronics along both the rows (x-direction) and the columns (y-direction) of the pixel array. The levels from these virtual reads are added to two edges of the science images as pixels, making up the 'overscan' region of the science image. This increases the number of rows and columns in the image from each CCD from 2048×4096 to 2112×4160.

The x-direction overscan pixels store calibration data about any short-term temporal variations in the camera electronics noise during the parallel transfer of electrons while performing a readout of the CCD. For each row, the overscan pixels

[5] http://www.astro.umd.edu/~veilleux/mmtf/datared.html
[6] http://iraf.noao.edu/

are averaged – rejecting any values more than three standard deviations from the mean – and the mean is subtracted from each pixel in the corresponding row. Once this is taken into account the x-direction overscan pixels are removed from the image, returning the number of columns to the original 4096. This process is repeated for all images, and for the zero-second exposure this ensures that any counts left are caused by longer-term effects in the CCD rather than simply short-term temperature conditions.

The y-direction overscan pixels store calibration data about how charge builds up in the pixels closest to the readout port. The net effect of this build-up is a gradient across the image, and this same gradient is stored in the levels over the range of the sixty-four overscan pixels. The overscan pixels are fit with a cubic spline, which is then subtracted from the entire column. The y-direction overscan pixels are removed from the image, returning the number of rows to the original 2048. Because the bias images are zero-second exposures they are not susceptible to charge build-up, and this correction is not performed on them. For all other images the correction is performed after the x-direction overscan and before the corrections described in the next section.

5.3.2 Bias subtraction and flat-fielding

The first step in bias subtraction is to combine the multiple zero-second exposures into a single master bias image for each of the eight chips that make up the Mosaic2 CCD array. This is done by first correcting for the x-direction overscan, and then creating a composite image containing the average value of the zero-second exposures for each pixel. These master bias files are then used in the preparation of the flat-field images and the science images by subtracting them on a pixel-by-pixel basis.

The master flat-field images, made up of images from each of the eight chips of

the Mosaic2 CCD, are created in a similar way to the master bias image. First the x- and y-direction overscan calibrations are performed, and then the master bias is subtracted. The bias-corrected flat-field images are then averaged to form a master image for each chip in each filter set. The goal of the flat-fielding process is to produce combined science images that are even across all eight chips, thus each of the master images in a filter set need to be normalised relative to each other. The centre of the camera's field of view, which falls on a particular chip in the Mosaic2 array, is normalised to a value of ~1. The normalisation required for this is applied to each of the flat field images in the set, ensuring that when combined each science image is even across the entire field of view.

Finally, all these processes are performed on each of the sets of science images. For each chip image the x- and y-direction overscan calibrations are performed, the bias is subtracted, and the normalised flat-field is divided through. At this point all the science images are now free of biases introduced in the act of observing. This leaves calibrating and cleaning the data itself, and combining the multiple chip images into a single, full-field science image.

5.3.3 Cosmic ray removal and sky subtraction

In addition to the steady stream of visible photons incident on the IMACS camera via the filters, stochastic, high-energy charged particles also impact the CCDs during exposures. When cosmic protons and alpha particles moving at relativistic speeds hit molecules in the atmosphere, they generate a shower of particles that strike the CCD. The charged particles, mainly muons, liberate electrons on the CCD that cause false readings within the science image (Groom, 2002). These artefacts, referred to in astronomy as 'cosmic rays', are easily recognised by their sharp edges as they are unaffected by the PSF that softens the edges of real objects. This makes

it easy to identify and mask out cosmic rays programatically, and for the corrected science images we apply the L.A.Cosmic algorithm (van Dokkum, 2001) to create these masks automatically. The MMTF scripts configure this algorithm with settings specific to the IMACS camera and augment the generated cosmic ray masks with additional masking for known bad pixels and columns within the CCDs.

The atmosphere itself has a diffuse glow that adds a background to each science image. The removal of this background is done using a process similar to the reference ring calibration of the MMTF air-gap controller. Using the calibrated optical axis location, along with the known mapping of the pixels on the CCD to the focal plane, the sky spectrum is azimuthally averaged and subtracted. During this process the cosmic ray and bad pixel masks are used to filter out sharp artefacts to ensure the smoothest sky calculation possible.

For our observations the sky noise dominated the error budget relative to CCD readout noise. The Mosaic2 camera, at the time of the observations, had a readout noise in each pixel averaged across the eight component chips of 5.90 cts. This is compared to a sky background ranging from 105 cts to 454 cts across the three observations of the five frames. This implies that the readout noise fraction of the error budget ranged from 1.3 % to 5.3 %, well in the sky-dominated regime in all science images.

5.3.4 Astrometry corrections and mosaicking

We next need to ensure that the astrometry for each image is properly calibrated, which is to say that we need to map the pixels in the image map to sky coordinates in a linear fashion. The combination of plane projection from the optical system of the IMACS camera, coupled with irregularities in the physical placement of the CCDs combine to cause distortions in the relative locations of objects across the field

of view. To correct for this, the pixel locations on each image must be mapped to a trusted coordinate system and the deviations from a linear mapping between pixels and sky coordinates are catalogued and corrected. The distortions in the IMACS optical system have been calibrated against dense star fields to high accuracy, allowing for the creation of astrometry error maps correcting for the higher-order distortions that do not change from exposure to exposure.

These maps are combined with metadata about the telescope orientation at the time of observation and the geometry and spacing of the chips making up the IMACS camera to calculate the high-order corrections required to linearise the pixel-to-sky relationship. These corrections are applied to each chip image separately, and afterwards each set of eight 2048×4096 chip images are combined into a single 8192×8192 mosaicked image. The cosmic ray and bad pixel masks are also corrected and combined using the same process, allowing for the final full-image astrometry corrections to mask out these artefacts properly.

The low-order astrometry corrections are the last stage of fixing the astrometry of these images. These corrections differ from exposure to exposure based on errors in the orientation of the telescope and the atmospheric conditions on the night. These distortions are determined programatically by comparing stars in the field of view to a catalogue of known stellar locations. These stars create tie points for the algorithm to stretch and skew the full mosaicked science images into a final properly flattened astrometric state.

5.3.5 PSF-matching, registering, and stacking exposures

For each filter we then need to stack the multiple exposures into a single science image. This is done by aligning the images (a process known as registering), degrading them to the lowest quality image, and summing their pixel values into a composite

image. The point-like objects in each image are catalogued, and their effective PSF is calculated. From this catalogue of PSF values, the mode is determined for each image and stored in its header. Next the images are registered against one another by comparing the coordinate system metadata in each image and linearly mapping the data from each image onto a common pixel grid. This mapping process uses the same algorithms and image transformation tools as the astrometry process in the previous steps. Once the images are registered, all the images are degraded to match the stored PSF of the image with the worst seeing. This is done by convolving the image with an appropriate Gaussian kernel to ensure each image has the same effective PSF. The exposures are then summed pixel-by-pixel, producing the final science image for each filter.

In our observations there was not a significant variation in seeing across the field in any of the individual exposures. Similarly there was not a significant variation between exposures at the same wavelength. All exposures were used in the final stacking process.

This results in a single, one-hour exposure for each wavelength imaged by the MMTF, a single fifteen-minute exposure for the broadband filter, and a series of short (1 s to 15 s) exposures of reference star EG 274 for photometric calibration.

5.4 Analysis of EF02 observational data

Based on the expected galaxy counts provided in section 4.4.4 (page 90), it was not surprising to find that no candidate Lyα galaxies were detected in the analysis of the EF02 science images. However, due to the uniqueness of the MMTF and the design of the five frame approach it is still worth discussing the process used to analyse this data set in depth.

We begin by discussing photometric calibration in section 5.4.1, and how to apply

it to MMTF observations, and then move on to a discussion of how to stack the five frames and pick out candidates in section 5.4.2. The topic of ghost stellar reflections is likely of most interest to future observations using tunable filters. This is discussed in section 5.4.3, and describes how these ghost images can easily be misidentified as emission-line sources given the MMTF reduction and analysis pipeline.

5.4.1 Photometric calibration

The final science images we produce are stored as a two-dimensional array of digital counts recorded by the CCD. In order to determine the flux of potential candidate Lyα galaxies in standard units, we first convert these counts to the AB magnitude system. The relationship between our observed counts in the telescope instrumentation and the AB magnitude system is:

$$m_{\mathrm{AB}} = m_{\mathrm{INST}} + m_{\mathrm{ZPT}} - m_{\mathrm{EXT}}, \tag{5.1}$$

where m_{AB} is the magnitude of the object in the AB magnitude system, m_{INST} is the magnitude determined from the counts recorded by the instrumentation, m_{ZPT} is the conversion factor between the m_{INST} magnitude system and the AB magnitude system, and m_{EXT} is the calculated atmospheric extinction for the particular observation.

Our observations of the reference star EG 274 provide us with values for m_{AB}, m_{INST}, and m_{EXT} in equation (5.1), allowing us to calculate the constant m_{ZPT} for each of our narrowband filters.

AB magnitude system

The AB magnitude system[7] is a logarithmic measure of an object's brightness, calibrated in absolute units rather than to a specific reference object (as in the Vega magnitude system). It is based on units of spectral flux density, defined as the rate at which electromagnetic energy is transmitted through a surface per unit area, per unit frequency. The zero point of the system (i.e. where $m_{\mathrm{AB}} = 0$) is set to 3631 Jansky, originally chosen to give the actual flux of the star Vega when measured in the V-band. The Jansky (Jy) is a common unit used to record spectral flux density in radio astronomy, where 1 Jy is defined to be $10^{-26}\,\mathrm{W\,m^{-2}\,Hz^{-1}}$ in SI units and $10^{-23}\,\mathrm{erg\,cm^{-2}\,s^{-1}\,Hz^{-1}}$ in the cgs unit system used throughout this thesis.

The AB magnitude of an object with a spectral flux density of f_ν is expressed mathematically as:

$$m_{\mathrm{AB}} = -2.5\log_{10}\left(\frac{\int f_\nu(\nu)\, R(\nu)\, \nu \mathrm{d}\nu}{\int 3631\,\mathrm{Jy}\, R(\nu)\, \nu \mathrm{d}\nu}\right), \tag{5.2}$$

where $R(\nu)$ is the effective response of the telescope's optical system, usually dominated by the transmissivity curve of the filter used. The normalised integral within the $\log_{10}$ term weights the flux by the response of the telescope, ensuring that an accurate representation of the flux received in the camera.

Given that all of our measurements have been made in terms of wavelength rather than frequency it is convenient to rewrite equation (5.2) in terms of a spectral energy density per unit wavelength λ, f_λ. This is a straightforward substitution using the speed of light c:

$$f_\nu = \frac{\lambda^2}{c} f_\lambda,$$

[7] See Oke (1974) and Oke & Gunn (1983).

and including unit conversions becomes:

$$\frac{f_\nu}{\mathrm{Jy}} = 3.336 \times 10^4 \left(\frac{\lambda}{\text{Å}}\right)^2 \frac{f_\lambda}{\mathrm{erg\,cm^{-2}\,s^{-1}\,Å^{-1}}}. \tag{5.3}$$

Combining equations (5.2) and (5.3) we arrive our desired definition of m_{AB}:

$$\begin{aligned} m_{\mathrm{AB}} &= -2.5\log_{10}\left(\frac{\int\left[3.336\times10^4\lambda^2\left(\frac{\mathrm{Jy}}{\mathrm{erg\,cm^{-2}\,s^{-1}\,Å^{-1}}}\right)f_\lambda(\lambda)\right]R(\lambda)\,\lambda\mathrm{d}\lambda}{\int 3631\,\mathrm{Jy}\,R(\lambda)\,\lambda\mathrm{d}\lambda}\right), \\ &= -2.5\log_{10}\left(\frac{\int f_\lambda(\lambda)\,R(\lambda)\,\lambda\mathrm{d}\lambda}{\int 1.086\times10^{-1}\,\mathrm{erg\,cm^{-2}\,s^{-1}\,Å^{-1}}\,R(\lambda)\,\lambda^{-1}\mathrm{d}\lambda}\right), \\ &= -2.5\log_{10}\left(\frac{\int f_\lambda(\lambda)\,R(\lambda)\,\lambda\mathrm{d}\lambda}{\int R(\lambda)\,\lambda^{-1}\mathrm{d}\lambda}\right) - 2.5\log_{10}\left(\frac{1}{1.086\times10^{-1}}\right), \\ &= -2.5\log_{10}\left(\frac{\int f_\lambda(\lambda)\,R(\lambda)\,\lambda\mathrm{d}\lambda}{\int R(\lambda)\,\lambda^{-1}\mathrm{d}\lambda}\right) - 2.408. \end{aligned} \tag{5.4}$$

AB Magnitude of EG 274

The first step in flux-calibrating our science images is to determine what the flux of the standard star should be, assuming no degradation in the image quality by the atmosphere or the MMTF optical system. Our reference star, EG 274, has been observed in detail previously, and its calibrated spectrum is known to high accuracy (Hamuy et al., 1994). This spectrum, shown in figure 5.1, is used to determine the expected AB magnitude EG 274 for each of the MMTF filters.

The width of each wavelength bin in the EG 274 spectrum is 50 Å, much broader than the 12 Å FWHM of the narrowband images. Thus it is unnecessary for us to weight the response curve, and we therefore make use of the monochromatic version of equation (5.4) to calculate the filter-specific standard magnitude of EG

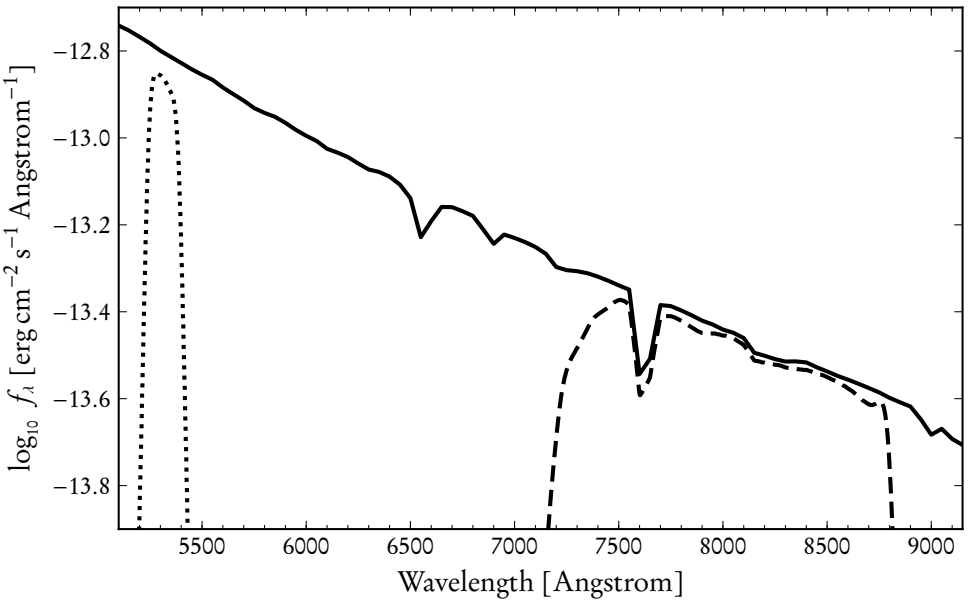

Figure 5.1: Spectral wavelength flux of reference star EG 274 as measured by Hamuy et al. (1994). For reference, the dotted line is the portion of this flux transmitted by the 5290 Å MMTF blocking filter, and the dashed line is portion transmitted by the CTIO I $f/2$ filter.

274, $m_{\mathrm{STD,MMTF}}$:

$$m_{\mathrm{STD,MMTF}} = -2.5\log_{10}\left(f_{\lambda,\mathrm{MMTF}}\right) - 5\log_{10}\left(\lambda_{\mathrm{MMTF}}\right) - 2.408, \tag{5.5}$$

where λ_{MMTF} is the central wavelength of the MMTF specific narrowband filter. The 5250 Å bin of the EG 274 flux curve has a spectral flux of 1.651×10^{-11} erg cm^{-2} s^{-1} Å^{-1} and this value was used to calculate m_{STD} for each filter. These values can be found in table 5.1.

SExtractor

For detecting candidate objects and measuring their flux we make use of the SExtractor software package (Bertin & Arnouts, 1996). SExtractor works by processing the science image with the following pipeline:

- a measure of the background and its RMS noise is made across the image, optionally excluding pixels flagged in a mask file;
- this background is then subtracted from the image;
- the entire image is then convolved with a filter to increase the SNR of candidates relative to their local backgrounds;
- a thresholding algorithm is then applied to isolate connected groups of pixels that are each a set multiple of the local background;
- the objects are then deblended, broken up into different objects based upon their intensity profile;
- the positions and shapes of the objects are then determined in preparation for classification and photometry;
- the objects are then cleaned by reconsidering detections by accounting for contributions from neighbouring sources;
- photometry is performed on each object measuring the total counts and corresponding magnitude, with the default algorithm using a moment based approach inspired by Kron (1980);
- a classification algorithm is run scoring each object on how star-like or galaxy-like each object is, utilising a neural net trained with simulated data; and
- finally a catalogue is produced with an entry for each object on its location and flux along with optional values detailing the above pipeline.

Throughout this chapter we utilise the default FLUX_AUTO and MAG_AUTO algorithms for our photometry.

Instrumentation magnitude of EG 274

In each band of the science imaging of EG 274 we used SExtractor to sum the number of counts detected by the CCD for each pixel associated with EG 274. Dividing these counts by the exposure time of the image we arrive at a flux for EG 274, in units of counts per second (cts s^{-1}). This flux is converted to an instrument magnitude, m_{INST}:

$$m_{\mathrm{INST}} = -2.5\log_{10}(C/t)\,. \tag{5.6}$$

For each filter we average the fluxes from the two observations of EG 274 to arrive at a single m_{INST} per filter as shown in table 5.1.

Atmospheric extinction

As cosmic photons travel through the atmosphere they have a chance of interacting with atmospheric molecules and scattering out of view. This attenuation of the signal is dependent on the path length through the atmosphere and the wavelength of the incident photon. The path length is dependent on the altitude angle of the observed object, with the minimum length at an altitude angle of 90° defined to be one airmass (am), increasing towards a maximum at the horizon. The amount of extinction per airmass at a particular wavelength is denoted κ_λ and is given in units magnitude per airmass (mag am^{-1}). These units allow us to calculate the extinction magnitude m_{EXT} by multiplying the appropriate κ_λ by the observed airmass A_λ:

$$m_{\mathrm{EXT}} = \kappa_\lambda A_\lambda. \tag{5.7}$$

κ_λ is unique for each observatory, and is measured across the wavelength range of each instrument during commissioning. Table 5.1 gives the airmass and corresponding κ_λ, as well as the averaged m_{EXT} for each pair of observations in the five filters.

Table 5.1: Measured and calculated values used to flux-calibrate the MMTF science images taken of the EF02 field.

Filter	Counts*	Duration†	$A_\lambda{}^\ddagger$	$\kappa_\lambda{}^\S$	m_{EXT}	m_{INST}	m_{STD}	m_{ZPT}
5236-1	3.622	15	1.140	0.16	0.18	−10.96	10.95	22.10
5236-2	3.639	15	1.143					
5248-1	4.144	15	1.132	0.16	0.18	−11.10	10.95	22.23
5248-2	4.149	15	1.136					
5260-1	4.384	15	1.125	0.16	0.18	−11.16	10.94	22.29
5260-2	4.374	15	1.129					
5272-1	4.365	15	1.148	0.16	0.18	−11.16	10.94	22.28
5272-2	4.350	15	1.152					
5284-1	4.282	15	1.156	0.16	0.19	−11.14	10.93	22.26
5284-2	4.267	15	1.160					

$^\star[10^5\,\mathrm{cts}]$ $^\dagger[\mathrm{s}]$ $^\ddagger[\mathrm{am}]$ $^\S[\mathrm{mag\,am^{-1}}]$

Calculating candidate luminosity

Finally, we calculate the zero-point magnitude m_{ZPT} by rearranging equation (5.1):

$$m_{\mathrm{ZPT}} = m_{\mathrm{STD}} - m_{\mathrm{INST}} + m_{\mathrm{EXT}}, \tag{5.8}$$

The variable m_{ZPT} is the point where the magnitude of flux as measured in the instrument is equal to the 3631 Jy zero-point of the AB system, bringing the two systems into agreement. The calculated zero-points for each filter are shown in table 5.1.

Once a candidate is detected, and its instrument magnitude is recorded, we then must convert this to a final Lyα luminosity. This is done using the fact that the transmitted flux through a Fabry-Pérot etalon is defined to be $f_\lambda \times \pi/2 \times \mathrm{FWHM}$ (Swinbank et al., 2012), where f_λ is the spectral flux density of the object at the central frequency of the tunable filter. Following from this fact, we can again rearrange

equation (5.1) to arrive at the Lyα luminosity of the detected object, $L_{\mathrm{Ly}\alpha}$:

$$\begin{aligned} L_{\mathrm{Ly}\alpha} &= \frac{\pi}{2}\left(\frac{\mathrm{FWHM}}{\lambda^2}\right) 10^{-0.4(m_{\mathrm{INST}}+m_{\mathrm{ZPT}}-m_{\mathrm{EXT}})-0.9632}\left(4\,\pi\left[\frac{D_{\mathrm{L}}}{\mathrm{cm}}\right]^2\right), \\ &= 2\,\mathrm{FWHM}\left(\frac{\pi}{\lambda}\frac{D_{\mathrm{L}}}{\mathrm{cm}}\right)^2 10^{-0.4(m_{\mathrm{INST}}+m_{\mathrm{ZPT}}-m_{\mathrm{EXT}})-0.9632}, \end{aligned} \tag{5.9}$$

where D_{L} is the luminosity distance to object measured in cm, and m_{INST} is the measured instrument magnitude.

5.4.2 Candidate selection

From the final science images of the EF02 field we need a process that will detect all possible candidate Lyα galaxies, while at the same time excluding all non-emission line objects. This candidate selection process will require us to align each of the science images to a single pixel grid, create object catalogues in each of the five frames, and finally stack these catalogues by cross-referencing objects detected in multiple frames.

Frame registration

To begin candidate selection we first register each of the five frames to a common pixel grid. This is achieved by finding matching coordinates in each of the five frames and then plotting a transformation solution to produce the final registered images. Because the 5260 Å frame is our highest quality image we transform the other frames relative to it. The final science image of the 5260 Å frame can be seen in figure 5.2, with the pixels outside of the monochromatic spot masked.

Before registration we generate two masks for each of the frames: a field of view mask to remove the telescope housing and vignetting from the outer rim of the image, and a monochromatic spot mask to removes everything outside the 13.8′

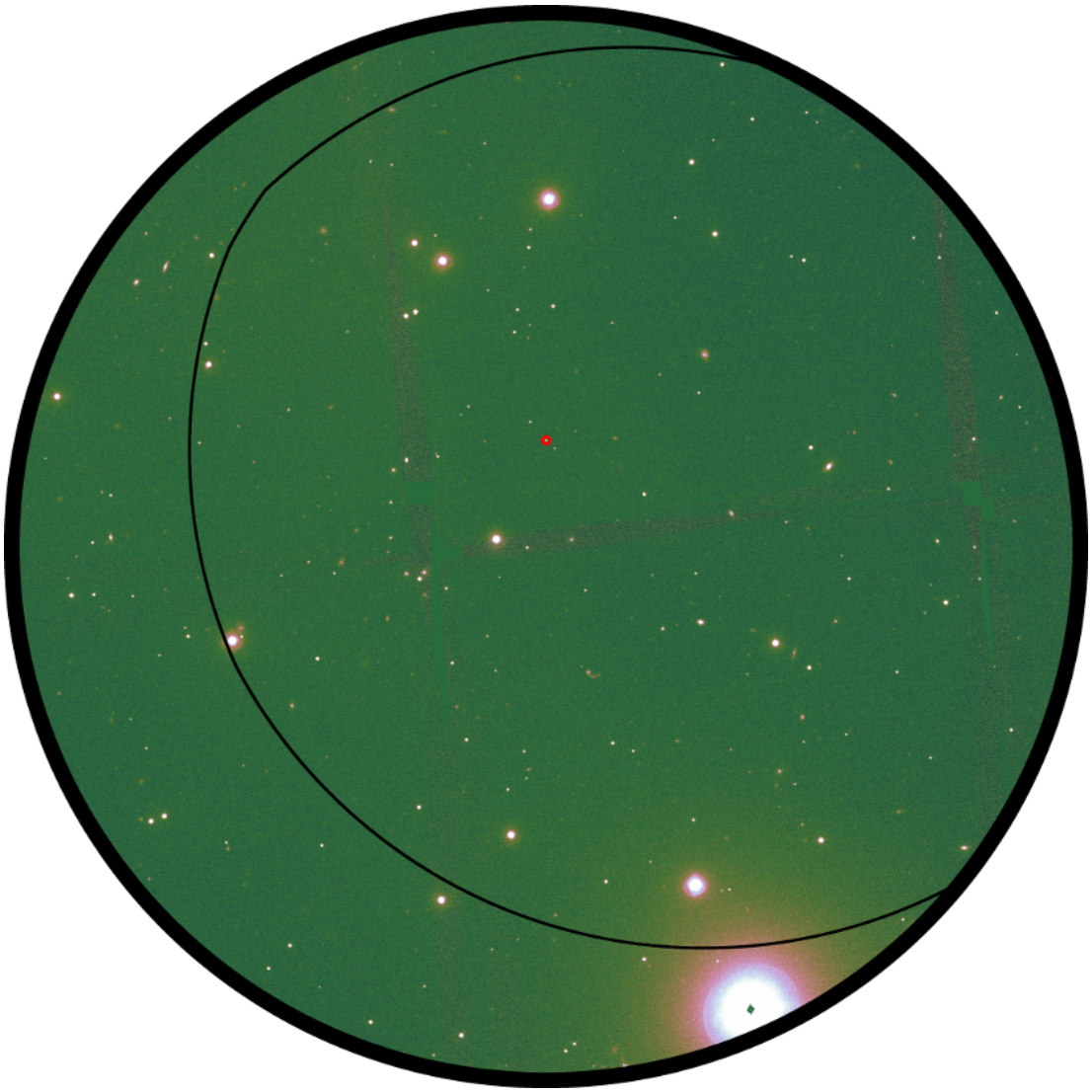

Figure 5.2: Field within the monochromatic spot of the 5260 Å science image. The field within the monochromatic spot is 13.8′ (4140 pixels) in diameter. The thin black outline is the stacked monochromatic spot, marking the region included in the candidate selection. The red circle above the centre point is the EF02 quasar, located at (10°6′43.8″, 0°13′48.4″).

spot. These masks are simple image files with the same number of pixels as our science images. They contain a value of 1 in all pixels to be analysed and a value of 0 in all pixels to be ignored.

We use SExtractor to identify all stellar objects within each of the image frames, using the field of view mask to remove spurious artefacts from the generated catalogue. Using these catalogues, along with the coordinates of three tie points (chosen by eye) corresponding to the largest saturated stars, we use IRAF to calculate a set of transformation solutions to map each of the other four frames to the pixel grid on the 5260 Å reference frame.

These same transformations are performed for the monochromatic spot mask for each frame as well to keep it aligned relative to the optical axis in each frame. We stack the resulting spot masks into a single composite, as described in section 4.3.1 (page 79), that masks out all pixels that are not within the monochromatic spot of all the frames. The outline of this composite mask can be seen in figure 5.2 as an irregular black line.

To aid in the detection of objects that straddle two frames, we co-add adjacent frames to form wider narrowband images with a combined bandpass of 24 Å. These pair images are included throughout the candidate detection and catalogue creation process, and are presented in the final visual inspection of candidates.

Catalogue creation

We run SExtractor on the now registered images to build a set of frame-specific catalogues of all objects with a SNR of 3 or above (the lower SNR of 3 to detect objects straddling adjacent frames). This is run with the composite monochromatic spot mask to ensure all detected objects fall within the modelled survey volume. We also exclude all objects within 25 pixels of the edge of the mask as the abrupt change

in pixel values near the mask causes spurious object detections. These catalogues are then cross-referenced with the catalogues from all other frames, matching objects by their pixel location. When performing this match we allow a tolerance in pixels equal to the largest PSF recorded among the science images. These stacked objects make up the final candidate list to be confirmed visually.

To help further inform our visual inspection, we run SExtractor once more on all frames, this time using the 'Dual Image Mode'[8] feature. This allows for the flux in one image to be calculated using a detection in another, giving each of our objects a magnitude in all frames regardless of whether they were detected or not. This was extended to include magnitudes calculated for the broadband CTIO I $f/2$ image as well to help determine if an object was a continuum source during visual inspection. These magnitudes are stored in the metadata for the object in the final object catalogue.

For the EF02 observations, a total of 220 objects were detected within the survey volume.

Visual inspection of candidates

For each object in the stacked catalogue, we generate a series of thumbnail images, each 51×51 pixels ($10.2'' \times 10.2''$) in area, centred on the averaged pixel location of the object across all frames. The thumbnails from each frame, pair of frames, and broadband CTIO I $f/2$ image are composited into a final inspection image. These are placed horizontally, with the broadband image on the far left, and the frames, and pairs of frames, in order of ascending wavelength from left to right. A reticle is superimposed onto each thumbnail, as well as a black box in the lower left corner for the frames in which the object was detected. Figure 5.3 shows an example of

[8]This feature of SExtractor was implemented specifically to help analyse data collected by the Taurus Tunable Filter, and is invaluable in general for tunable filter work.

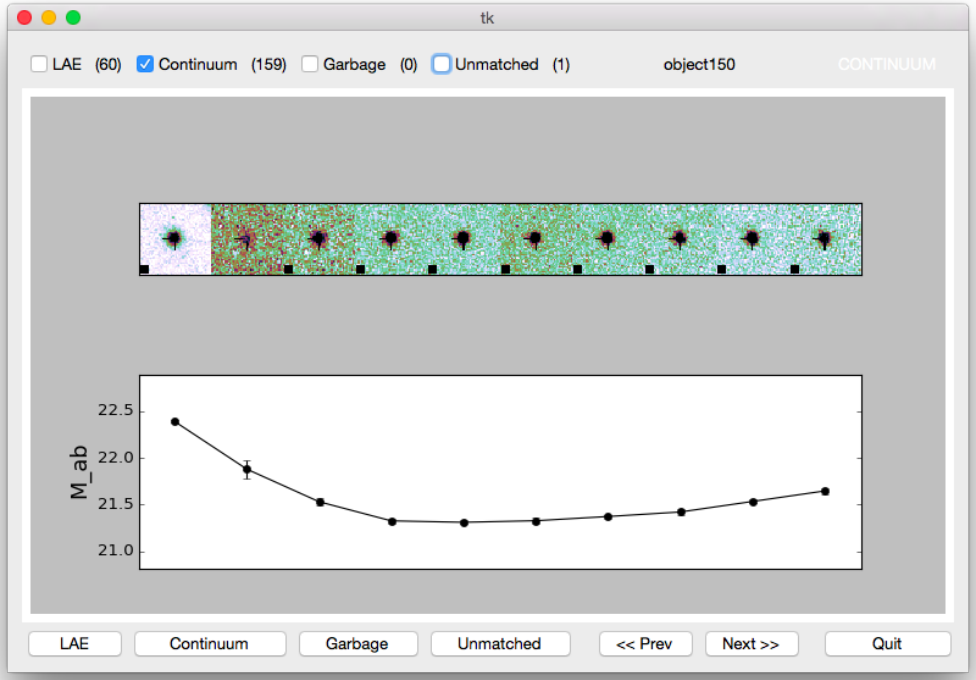

Figure 5.3: Screenshot of the candidate inspection tool displaying EF02. The different category filters are in the top left, the object number and assigned classification are in the top right, and the buttons for classifying and navigating through inspection images run along the bottom. The inspection image in the centre shows thumbnails for each frame. The black squares in the lower left of the thumbnail indicate that the object was detected in that frame, and a reticle is overlain indicating the centre of the thumbnail. Below the image is a graph showing the AB magnitude recorded for each frame.

the inspection image corresponding to quasar EF02 being displayed in our candidate viewer software.

Before inspecting them visually, each object is first given an initial categorisation based on a set of simple rules. An object is classified as a candidate Lyα galaxy if it is detected in:

- only one frame,
- exactly two adjacent frames,

- only one frame and in a corresponding co-added pair image,
- exactly two adjacent frames and in the corresponding co-added pair image, or
- only one co-added pair image.

If an object was not classified as a candidate Lyα galaxy using the above criteria, it must therefore have been detected in more than two frames, or in non-adjacent frames. If this is the case and it has a detectable flux in the CTIO I $f/2$ image, it is classified as a continuum object. Any object not matched by these criteria are left unclassified.

We perform the final visual inspection using the custom built tool seen in figure 5.3. This tool is designed to allow us to present and categorise each object, as well as letting us revisit previously categorised objects and filter objects based on their currently assigned classification. It presents the thumbnails for each object, along with a graph of the detected magnitude in each frame, and allows us to quickly navigate through and categorise each object using only the keyboard.

When we applied this initial classification algorithm to the stacked object catalogue we had the following breakdown of classifications: 60 candidate Lyα galaxies, 159 continuum sources, and 1 unmatched object. All objects that were initially classified as a continuum source were verified upon inspection. The unmatched object was classified as a continuum object after inspection as well, having failed the initial continuum classifier because it was not detected in the CTIO I $f/2$ image. The candidate Lyα detection had multiple false positives, all but one of which were found to be artefacts from improperly masked cosmic rays. These triggered the Lyα candidate classifier because they only appeared in one frame without there being any flux in the other four frames. The final misidentified Lyα candidate was a continuum object that was not detected at the SNR level in the CTIO I $f/2$ but contained flux

upon inspection. Our final visual inspection classified 11 objects as potential Lyα candidate galaxies, 161 objects as continuum sources, and 48 objects as non-source artefacts.

Once visually identified as candidate Lyα galaxies, we inspected the 11 potential detections in further detail. All of these objects were determined to be ghost stellar reflections, as we will discuss in section 5.4.3. We therefore concluded that there are no detectable Lyα galaxies in the observations of the EF02 field.

With all five of the narrowband frames of the EF02 field we are able to say that no Lyα emitting galaxies were detected at a SNR of 5 in a volume of 246.7 pMpc^3, at $z = 3.3$, down to a flux limit of 4.6×10^{-16} erg cm^{-2} s^{-1}. If we exclude the 5236 Å frame, we are able to say that no Lyα emitting galaxies were detected at a SNR of 5 in a volume of 198.0 pMpc^3, at $z = 3.3$, down to a flux limit of 1.9×10^{-16} erg cm^{-2} s^{-1}.

5.4.3 Ghost reflections

A faint reflection exists between the MMTF and the camera, which can lead to spurious objects being classified as potential detections using our selection method. Saturated stars in the field of view cause significant reflective ghosts in the image, enough so that these artefacts can easily be detected at a SNR of 3. These reflections are easy to find when looking at a single exposure, as they are directly across the optical axis from their progenitor star. However, when exposures are dithered and stacked, the optical axis moves relative to the saturated stars leading to a family of ghosts in the resultant image and no single optical axis through which to easily identify their associated stars. Figure 5.4 shows an individual exposure of the 5260 Å frame, with markings associating the saturated stellar sources with their ghost.

Each of these ghosts will only be visible in the one MMTF frame, meaning our candidate selection technique that looks for objects appearing in single or adjacent

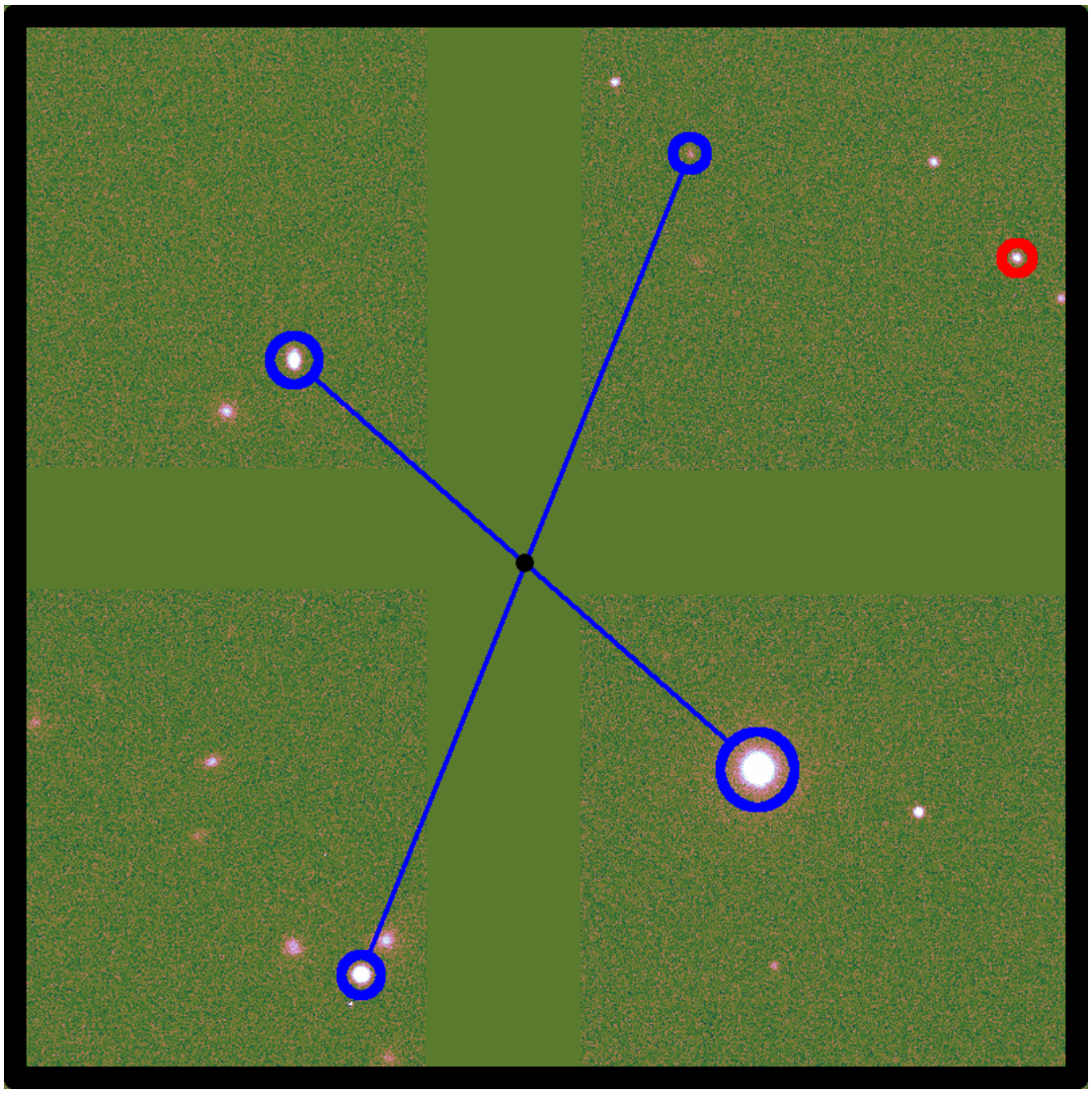

Figure 5.4: Ghost stellar images in a 5260 Å exposure of the EF02 field. The black dot in the centre is the optical axis, and the blue circles and lines link the saturated stellar objects (in the lower half of the image) with their ghosts. The horizontal and vertical stripes are the chip gaps on the Mosaic2 camera. The red circle in the top right is the EF02 quasar, located at (10°6′43.8″, 0°13′48.4″).

frames is particularly susceptible to detecting these artefacts. Currently there is not an automated script for generating a list of potential ghost locations in the MMTF reduction pipeline, though it would not be difficult to create. For our candidate selection we added a final step to the manual inspection to account for this once it was identified to be a problem. We went back to the unstacked images for each object in the frame they were detected and visually inspected the region directly across the optical axis for saturated stars. All 11 of the candidates that passed our first round of visual inspections were found to be ghosts.

A quick way to check for these ghosts is to see if there is any noticeable flux above background levels in the adjacent frames. The nature of the way the ghosts are formed implies that there should be no flux in either of the adjacent frames. For our particular experimental set-up, the FWHM of each frame was roughly that of the expected Lyα line. Thus, for a galaxy to appear in only one frame would require it to be at exactly the redshift corresponding to $\lambda_{\mathrm{Ly}\alpha}$ in our frame, which is unlikely. Also, because these ghosts are based on stellar objects with large SNR on a pixel by pixel basis, the error in their magnitudes are insignificant giving another clue as to their nature. This can be seen in figure 5.5 which shows a ghost object in our inspection tool.

5.5 Summary

In this chapter we have discussed the calibration, observational procedures, and analysis of the MMTF narrowband observations conducted in April, 2012. We discussed the unique data reduction required to produce science images using the MMTF pipeline and presented an analysis of these calibrated images. This analysis included the creation of a candidate catalogue, the visual inspection and classification of each detected object in the catalogue, and the determination of the Lyα luminosity of a

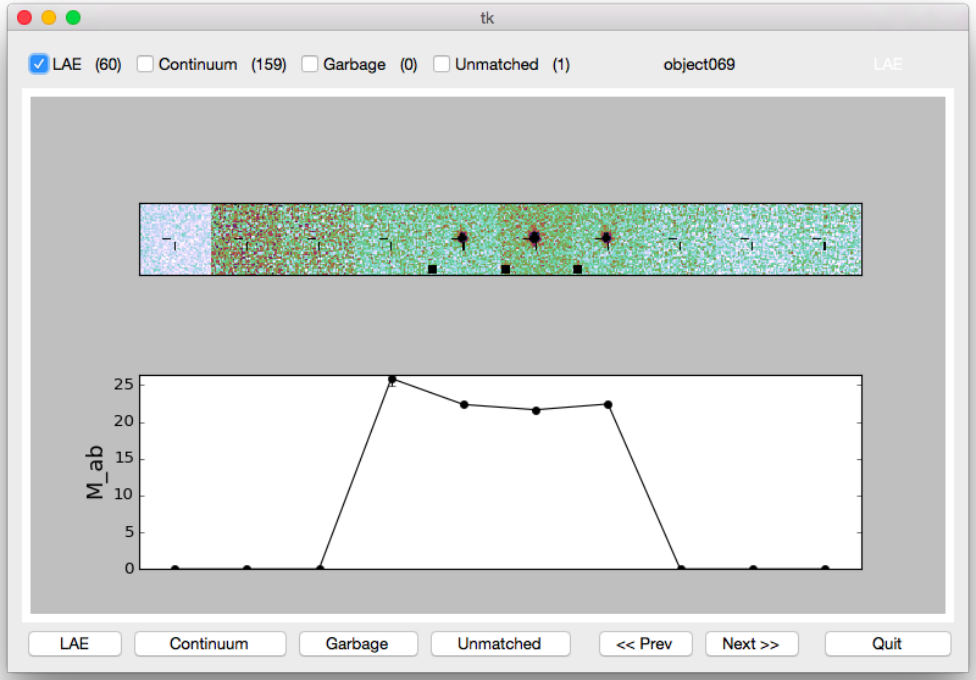

Figure 5.5: Screenshot of the candidate inspection tool displaying a stellar ghost image.

successfully identified object from its measured magnitude. The main result from this chapter is that no candidate Lyα galaxies were detected in the EF02 quasar field, which was in good agreement with the modelling presented in chapter 4.

Chapter 6

Conclusion

In this thesis a new probe of galaxy formation is presented, focusing on the modelling and observation of surrogate environments around quasars to parametrise the impact of intense ionising radiation on galaxy evolution. The semi-analytic modelling of the intergalactic medium in the vicinity of a quasar and its impact on the detectability of star forming galaxies by their Lyα emission forms the basis for this technique. The tunable filter observations presented, with their unique data collection, calibration, and reduction processes, complement this modelling by providing a laboratory to observe galactic Lyα emission around quasars. Taken together, the modelling and observational techniques create a framework for constraining the critical ionising flux required to suppress or delay galaxy formation during the epoch of reionisation.

It is shown that the increased density of the intergalactic medium around a quasar and the increased ionisation background produced by said quasar, severely impact the transmission of Lyα photons from neighbouring galaxies. The model presented combines the structure formation history and statistical clustering of dark matter haloes to build up a prediction for the average number of galaxies that should be detectable by their Lyα emission around a given quasar and reproduces the results of previous Lyα galaxy surveys. The major result of this modelling is that in the vicinity of a quasar, even in the absence of any enhanced ionising radiation from the quasar, there should be a detectable overdensity of Lyα emitting galaxies.

This modelling is specifically applied to observations that detected no Lyα emission in the immediate vicinity of the quasar PKS 0424-131. These calculations suggest that this null detection is only consistent with the model at the 68% (90%) level if all galaxies below a mass of $1.2 \times 10^{12}\,M_{\odot}$ ($2.5 \times 10^{12}\,M_{\odot}$) are removed, corresponding to a virial temperature greater than 3.4×10^{6} K. These results suggest that considerable radiative suppression of galaxy formation by PKS 0424-131 is taking place.

The unique suitability for observing Lyα emission with a Fabry-Pérot tunable filter motivated an experiment using the Maryland-Magellan Tunable Filter to detect Lyα emission around $z \sim 3.3$ quasars. The quality of the data is not sufficient to expect the detection of any galaxies by their Lyα emission, a prediction borne out in the detailed analysis of the science images that failed to detect Lyα emission. This analysis includes a discussion on ways to detect and remove ghost reflections from stellar sources during candidate selection, an imaging artefact unique to tunable filters.

The modelling presented suggests that tunable filter searches for Lyα emission are a promising new way to probe the history of galaxy formation. Future tunable filter observations will provide the statistics required for the spatial mapping of Lyα emitters around luminous quasars. In the coming decade, there are multiple facilities that are ideally suited to searches for Lyα emission at high-redshift, including the Osiris Tunable Filter on the Grantecan 10.2 m telescope (Cepa et al., 2003), the Maryland-Magellan Tunable Filter on the Magellan Baade telescope discussed in this thesis, and tunable filter instruments under development for the NTT 3.5 m and the SOAR 4 m telescopes (Marcelin et al., 2008; Taylor et al., 2010). All of these instruments are well adapted to study the impact of quasars on their environs, and will help to put meaningful constraints on the critical ionising flux required to disrupt galaxy formation.

References

Adelberger, K. L., Steidel, C. C., Kollmeier, J. A. & Reddy, N. A. (2006). Possible Detection of Lyα Fluorescence from a Damped Lyα System at Redshift $z \sim 2.8$. *ApJ*, *637*(1), 74.

Alvarez, M. A., Bromm, V. & Shapiro, P. R. (2006, mar). The H II Region of the First Star. *ApJ*, *639*(2), 621.

Babul, A. & Rees, M. J. (1992, mar). On dwarf elliptical galaxies and the faint blue counts. *MNRAS*, *255*, 346.

Barkana, R. (2004). A model for infall around virialized haloes. *MNRAS*, *347*, 59.

Barkana, R. & Loeb, A. (1999, sep). The Photoevaporation of Dwarf Galaxies during Reionization. *ApJ*, *523*, 54.

Barkana, R. & Loeb, A. (2001, jul). In the beginning: the first sources of light and the reionization of the universe. *Phys. Rep.*, *349*, 125.

Bertin, E. & Arnouts, S. (1996, jun). SExtractor: Software for source extraction. *A&AS*, *117*, 393.

Blanc, G. A., Adams, J. J., Gebhardt, K., Hill, G. J., Drory, N., Hao, L., ... Tufts, J. (2011, jul). The HETDEX Pilot Survey. II. The Evolution of the Lyα Escape

Fraction from the Ultraviolet Slope and Luminosity Function of $1.9 < z < 3.8$ LAEs. *ApJ*, *736*, 31.

Bland-Hawthorn, J. & Jones, D. H. (1998, apr). Taurus Tunable Filter: A flexible approach to narrowband imaging. *Publ. Astron. Soc. Australia*, *15*, 44.

Bland-Hawthorn, J., Sokolowski, J. & Cecil, G. (1991, jul). Imaging spectrophotometry of ionized gas in NGC 1068. II - Global ionization of the inner disk. *ApJ*, *375*, 78.

Bolton, J. S. & Haehnelt, M. (2007, nov). The observed ionization rate of the intergalactic medium and the ionizing emissivity at $z \geq 5$: evidence for a photon-starved and extended epoch of reionization. *MNRAS*, *382*, 325.

Bouwens, R. J., Illingworth, G. D., Franx, M., Chary, R.-R., Meurer, G. R., Conselice, C. J., ... van Dokkum, P. (2009, nov). UV Continuum Slope and Dust Obscuration from $z \sim 6$ to $z \sim 2$: The Star Formation Rate Density at High Redshift. *ApJ*, *705*, 936.

Bromm, V. & Yoshida, N. (2011, sep). The First Galaxies. *ARA&A*, *49*, 373.

Bromm, V., Yoshida, N., Hernquist, L. & McKee, C. F. (2009, may). The formation of the first stars and galaxies. *Nature*, *459*(7), 49.

Bruns, L. R., Wyithe, J. S. B., Bland-Hawthorn, J. & Dijkstra, M. (2012, apr). Clustering of Lyα emitters around luminous quasars at $z = 2$–3: an alternative probe of reionization on galaxy formation. *MNRAS*, *421*(3), 2543.

Cantalupo, S., Lilly, S. J. & Porciani, C. (2007, mar). Plausible Fluorescent Lyα Emitters around the $z = 3.1$ QSO 0420-388. *ApJ*, *657*, 135.

Cantalupo, S., Porciani, C., Lilly, S. J. & Miniati, F. (2005, jul). Fluorescent Lyα Emission from the High-Redshift Intergalactic Medium. *ApJ*, *628*(1), 61.

Cepa, J., Aguiar-Gonzalez, M., Bland-Hawthorn, J., Castaneda, H., Cobos, F. J., Correa, S., ... Tejada, C. (2003, mar). OSIRIS tunable imager and spectrograph for the GTC. Instrument status. In M. Iye & A. F. M. Moorwood (Eds.), *Instrument design and performance for optical/infrared ground-based telescopes* (Vol. 4841, p. 1739). Bellingham.

Dayal, P. & Ferrara, A. (2011). The visibility of Lyman α emitters during reionization. *MNRAS*, *410*, 830.

Dijkstra, M., Haiman, Z., Mesinger, A. & Wyithe, J. S. B. (2008, dec). Fluctuations in the high-redshift Lyman-Werner background: close halo pairs as the origin of supermassive black holes. *MNRAS*, *391*, 1961.

Dijkstra, M., Haiman, Z., Rees, M. J. & Weinberg, D. H. (2004, feb). Photoionization Feedback in Low-Mass Galaxies at High Redshift. *ApJ*, *601*, 666.

Dijkstra, M., Lidz, A. & Wyithe, J. S. B. (2007, may). The impact of The IGM on high-redshift Lyα emission lines. *MNRAS*, *377*, 1175.

Dijkstra, M. & Wyithe, J. S. B. (2010, oct). Seeing through the trough: outflows and the detectability of Lyα emission from the first galaxies. *MNRAS*, *408*, 352.

Dressler, A., Hare, T., Bigelow, B. C. & Osip, D. J. (2006, jun). IMACS: the wide-field imaging spectrograph on Magellan-Baade. *Proc. SPIE*, *6269*, 62690F.

Efstathiou, G. (1992, may). Suppressing the formation of dwarf galaxies via photoionization. *MNRAS*, *256*, 43.

Fan, X., Strauss, M. A., Becker, R. H., White, R. L., Gunn, J. E., Knapp, G. R., ... Fukugita, M. (2006, jul). Constraining the Evolution of the Ionizing Background and the Epoch of Reionization with $z \sim 6$ Quasars. II. A Sample of 19 Quasars. *AJ*, *132*, 117.

Faucher-Giguère, C.-A., Lidz, A., Hernquist, L. & Zaldarriaga, M. (2008, nov). Evolution of the Intergalactic Opacity: Implications for the Ionizing Background, Cosmic Star Formation, and Quasar Activity. *ApJ*, *688*, 85.

Francis, P. J. & Bland-Hawthorn, J. (2004, sep). The mysterious absence of neutral hydrogen within 1 Mpc of a luminous quasar at redshift 2.168. *MNRAS*, *353*, 301.

Gawiser, E., van Dokkum, P. G., Gronwall, C., Ciardullo, R., Blanc, G. A., Castander, F. J., ... Virani, S. N. (2006, may). The Physical Nature of Lyα-emitting Galaxies at $z = 3.1$. *ApJ*, *642*, 13.

Gebhardt, K., Pryor, C., Williams, T. B. & Hesser, J. E. (1994, jun). Fabry-Perot measurements of the dynamics of globular cluster cores: M15 (NGC 7078). *ApJ*, *107*, 2067.

Gnedin, N. Y. (2000, oct). Effect of Reionization on Structure Formation in the Universe. *ApJ*, *542*, 535.

Gonçalves, T. S., Steidel, C. C. & Pettini, M. (2008). Detection of the Transverse Proximity Effect: Radiative Feedback from Bright QSOs. *ApJ*, *676*(2), 816.

Greenstein, J. L. & Schmidt, M. (1964, oct). The Quasi-Stellar Radio Sources 3c 48 and 3c 273. *ApJ*, *140*, 1.

Gronwall, C., Ciardullo, R., Hickey, T., Gawiser, E., Feldmeier, J. J., van Dokkum, P. G., ... Treister, E. (2007, sep). Lyα Emission-Line Galaxies at $z = 3.1$ in the Extended Chandra Deep Field-South. *ApJ*, *667*, 79.

Groom, D. (2002). Cosmic rays and other nonsense in astronomical CCD imagers. *Exp. Astron.*, *14*(1), 45.

Gunn, J. E. & Peterson, B. A. (1965, nov). On the Density of Neutral Hydrogen in Intergalactic Space. *ApJ*, *142*, 1633.

Hamuy, M., Suntzeff, N. B., Heathcote, S. R., Walker, A. R., Gigoux, P. & Phillips, M. M. (1994, jun). Southern spectrophotometric standards, 2. *PASP*, *106*, 566.

Hogg, D. W. (1999, may). Distance measures in cosmology. *ArXiv e-prints*.

Iliev, I. T., Scannapieco, E., Martel, H. & Shapiro, P. R. (2003, may). Non-linear clustering during the cosmic Dark Ages and its effect on the 21-cm background from minihaloes. *MNRAS*, *341*, 81.

Iliev, I. T., Shapiro, P. R. & Raga, A. C. (2005, aug). Minihalo photoevaporation during cosmic reionization: evaporation times and photon consumption rates. *MNRAS*, *361*, 405.

Jacquinot, P. (1960, jan). New developments in interference spectroscopy. *Reports on Progress in Physics*, *23*(1), 267.

Jones, D. H. (1999). *Tunable filter surveys of star-forming galaxies* (Unpublished doctoral dissertation). The Australian National University.

Jones, D. H. & Bland-Hawthorn, J. (2001, apr). The Taurus Tunable Filter Field Galaxy Survey: Sample Selection and Narrowband Number Counts. *ApJ*, *550*(2), 593.

Kaiser, N. (1987, jul). Clustering in real space and in redshift space. *MNRAS*, *227*, 1.

Kashikawa, N., Kitayama, T., Doi, M., Misawa, T., Komiyama, Y. & Ota, K. (2007, jul). The Habitat Segregation between Lyman Break Galaxies and Lyα Emitters around a QSO at $z \sim 5$. *ApJ*, *663*, 765.

Kennicutt, R. C. (1998). Star Formation in Galaxies Along the Hubble Sequence. *ARA&A*, *36*, 189.

Kepner, J. V., Babul, A. & Spergel, D. N. (1997, sep). The Delayed Formation of Dwarf Galaxies. *ApJ*, *487*, 61.

Kitayama, T., Susa, H., Umemura, M. & Ikeuchi, S. (2001, oct). Criteria for the formation of Population III objects in the ultraviolet background radiation. *MNRAS*, *326*, 1353.

Kitayama, T., Tajiri, Y., Umemura, M., Susa, H. & Ikeuchi, S. (2000, jun). Radiation-hydrodynamical collapse of pre-galactic clouds in the ultraviolet background. *MNRAS*, *315*, 1.

Kitayama, T., Yoshida, N., Susa, H. & Umemura, M. (2004, oct). The Structure and Evolution of Early Cosmological H II Regions. *ApJ*, *613*(2), 631.

Komatsu, E., Smith, K. M., Dunkley, J., Bennett, C. L., Gold, B., Hinshaw, G., ... Wright, E. L. (2011, feb). Seven-year Wilkinson Microwave Anisotropy Probe (WMAP) Observations: Cosmological Interpretation. *ApJS*, *192*(2), 18.

Kron, R. G. (1980, aug). Photometry of a complete sample of faint galaxies. *ApJS*, *43*, 305.

Lahav, O., Lilje, P. B., Primack, J. R. & Rees, M. J. (1991). Dynamical effects of the cosmological constant. *MNRAS*.

Laursen, P., Sommer-Larsen, J. & Razoumov, A. (2011, feb). Intergalactic Transmission and Its Impact on the Lyα Line. *ApJ*, *728*, 52.

Lowenthal, J. D., Hogan, C. J., Green, R. F., Caulet, A., Woodgate, B. E., Brown, L. & Foltz, C. B. (1991, aug). Discovery of a Ly-alpha galaxy near a damped Ly-alpha absorber at $Z = 2.3$. *ApJ*, *377*, 73.

Macchetto, F., Lipari, S., Giavalisco, M., Turnshek, D. A. & Sparks, W. B. (1993, February). Identification of a Lyman-alpha radio-quiet galaxy at redshift $Z = 3.428$ - A primeval galaxy? *ApJ*, *404*, 511.

Marcelin, M., Amram, P., Balard, P., Balkowski, C., Boissin, O., Boulesteix, J., ... Vallée, P. (2008, aug). 3D-NTT: a versatile integral field spectro-imager for the NTT. In I. S. McLean & M. M. Casali (Eds.), *Ground-based and airborne instrumentation for astronomy ii* (Vol. 7014, p. 170). Marseille.

Menzel, D. H. (1926, aug). The Planetary Nebulae. *PASP*, *38*, 295.

Miralda-Escudé, J., Haehnelt, M. & Rees, M. J. (2000, feb). Reionization of the Inhomogeneous Universe. *ApJ*, *530*, 1.

Mo, H. J. & White, S. D. M. (1996, sep). An analytic model for the spatial clustering of dark matter haloes. *MNRAS*, *282*, 347.

Møller, P. & Warren, S. J. (1993, mar). Emission from a damped Ly-alpha absorber at $Z = 2.81$. *A&A*, *270*, 43.

Mortlock, D. J., Warren, S. J., Venemans, B. P., Patel, M., Hewett, P. C., McMahon, R. G., ... Röttgering, H. J. A. (2011, jun). A luminous quasar at a redshift of $z = 7.085$. *Nature*, *474*(7353), 616.

Nilsson, K. K. (2007). *The Lyman-alpha Emission Line as a Cosmological Tool* (Unpublished doctoral dissertation). Københavns Universitet.

Nilsson, K. K., Tapken, C., Møller, P., Freudling, W., Fynbo, J. P. U., Meisenheimer, K., ... Östlin, G. (2009, apr). Evolution in the properties of Lyman-α emitters from redshifts $z \sim 3$ to $z \sim 2$. *A&A*, *498*, 13.

Oke, J. B. (1974, feb). Absolute Spectral Energy Distributions for White Dwarfs. *ApJS*, *27*, 21.

Oke, J. B. & Gunn, J. E. (1983, mar). Secondary standard stars for absolute spectrophotometry. *ApJ*, *266*, 713.

Osterbrock, D. E. (1989). *Astrophysics of gaseous nebulae and active galactic nuclei*. Mill Valley, CA: University Science Books.

Ouchi, M., Shimasaku, K., Akiyama, M., Simpson, C., Saito, T., Ueda, Y., ... Yoshida, M. (2008, jun). The Subaru/XMM-Newton Deep Survey (SXDS). IV. Evolution of Lyα Emitters from $z = 3.1$ to 5.7 in the 1 deg^2 Field: Luminosity Functions and AGN. *ApJS*, *176*, 301.

Overzier, R. A., Bouwens, R. J., Cross, N. J. G., Venemans, B. P., Miley, G. K., Zirm, A. W., ... Zheng, W. (2008, jan). Lyman Break Galaxies, Lyα Emitters, and a Radio Galaxy in a Protocluster at $z = 4.1$. *ApJ*, *673*, 143.

Partridge, R. B. & Peebles, P. (1967). Are young galaxies visible? *ApJ*.

Peebles, P. (1980). *The large-scale structure of the universe*. Princeton University Press.

Persson, S. E., Carr, D. M. & Jacobs, J. H. (1990). Las campanas observatory seeing measurements. *Experimental Astronomy*.

Pirzkal, N., Malhotra, S., Rhoads, J. E. & Xu, C. (2007, sep). Optical-to-Mid-Infrared Observations of Lyα Galaxies at $z \sim 5$ in the Hubble Ultra Deep Field: A Young and Low-Mass Population. *ApJ*, *667*, 49.

Planck Collaboration, Ade, P. A. R., Aghanim, N., Arnaud, M., Ashdown, M., Aumont, J., ... et al. (2015, feb). Planck 2015 results. XIII. Cosmological parameters. *ArXiv e-prints*.

Press, W. H. & Schechter, P. (1974, feb). Formation of Galaxies and Clusters of Galaxies by Self-Similar Gravitational Condensation. *ApJ*, *187*, 425.

Reed, D. S., Bower, R., Frenk, C. S., Jenkins, A. & Theuns, T. (2007). The halo mass function from the dark ages through the present day. *MNRAS*, *374*, 2.

Salpeter, E. E. (1955, mar). The Luminosity Function and Stellar Evolution. *ApJ*, *121*, 161.

Scannapieco, E. & Barkana, R. (2002, jun). An Analytical Approach to Inhomogeneous Structure Formation. *ApJ*, *571*, 585.

Schaerer, D. (2003). The transition from Population III to normal galaxies: Lyα and He II emission and the ionising properties of high redshift starburst galaxies. *A&A*, *397*, 527.

Schirber, M. & Bullock, J. S. (2003, feb). Faint Active Galactic Nuclei and the Ionizing Background. *ApJ*, *584*, 110.

Shapley, A. E., Steidel, C. C., Adelberger, K. L., Dickinson, M., Giavalisco, M. & Pettini, M. (2001, nov). The Rest-Frame Optical Properties of $z \approx 3$ Galaxies. *ApJ*, *562*, 95.

Sharp, R. G. & Bland-Hawthorn, J. (2010, mar). Three-Dimensional Integral Field Observations of 10 Galactic Winds. I. Extended Phase (> 10 Myr) of Mass/Energy Injection Before the Wind Blows. *ApJ*, *711*, 818.

Shen, Y., Strauss, M. A., Oguri, M., Hennawi, J. F., Fan, X., Richards, G. T., ... Knapp, G. R. (2007, may). Clustering of High-Redshift ($z \geq 2.9$) Quasars from the Sloan Digital Sky Survey. *ApJ*, *133*, 2222.

Sheth, R. K., Mo, H. J. & Tormen, G. (2001, may). Ellipsoidal collapse and an improved model for the number and spatial distribution of dark matter haloes. *MNRAS*, *323*, 1.

Sokolowski, J., Bland-Hawthorn, J. & Cecil, G. (1991, jul). Imaging spectrophotometry of ionized gas in NGC 1068. III - Anisotropic excitation of the large-scale disk by scattering of nuclear continuum. *ApJ*, *375*, 583.

Swinbank, J., Baker, J., Barr, J., Hook, I. & Bland-Hawthorn, J. (2012, jun). Tunable filter imaging of high-redshift quasar fields. *MNRAS*, *422*(4), 2980.

Taylor, K., Mendes de Oliveira, C., Laporte, R., Guzman, C. D., Ramirez Fernandez, J., Scarano, S. J., ... Andrade, D. (2010, jul). The Brazilian tunable filter imager for SOAR. In E. Atad-Ettedgui & D. Lemke (Eds.), *Modern technologies in space- and ground-based telescopes and instrumentation* (Vol. 7739, p. 155). San Diego.

Thoul, A. A. & Weinberg, D. H. (1996, jul). Hydrodynamic Simulations of Galaxy Formation. II. Photoionization and the Formation of Low-Mass Galaxies. *ApJ*, *465*, 608.

van Dokkum, P. G. (2001, nov). Cosmic-Ray Rejection by Laplacian Edge Detection. *PASP*, *113*(789), 1420.

Veilleux, S., Weiner, B. J., Rupke, D. S. N., McDonald, M., Birk, C., Bland-Hawthorn, J., ... Vogel, S. N. (2010, jan). MMTF: The Maryland-Magellan Tunable Filter. *AJ*, *139*(1), 145.

Venemans, B. P., Röttgering, H. J. A., Miley, G. K., van Breugel, W. J. M., De Breuck, C., Kurk, J. D., ... Ford, H. (2007, jan). Protoclusters associated with $z > 2$ radio galaxies . I. Characteristics of high redshift protoclusters. *A&A*, *461*, 823.

Véron-Cetty, M. P. & Véron, P. (2010, jul). A catalogue of quasars and active nuclei: 13^{th} edition. *A&A*, *518*, A10.

White, M. (2001, feb). The mass of a halo. *A&A*, *367*(1), 27.

Wolfe, A. M., Lanzetta, K. M., Turnshek, D. A. & Oke, J. B. (1992, jan). Lyman-alpha emission from the damped Lyman-alpha system toward H0836 + 113. *ApJ*, *385*, 151.

Wyithe, J. S. B. & Loeb, A. (2005, mar). Calibrating the Galaxy Halo-Black Hole Relation Based on the Clustering of Quasars. *ApJ*, *621*, 95.

Zanstra, H. (1927, jan). An Application of the Quantum Theory to the Luminosity of Diffuse Nebulae. *ApJ*, *65*, 50.

Zitrin, A., Labbe, I., Belli, S., Bouwens, R., Ellis, R. S., Roberts-Borsani, G., … Smit, R. (2015, sep). Lyα emission from a luminous $z = 8.68$ galaxy: implications for galaxies as tracers of cosmic reionization. *ApJ*, *810*(1), 12.